DE-SC04-01AL67526

Solicitation Number: DE-SC04-01AL67526, Research and Development to Increase Engine Efficiency, Reduce Emissions, and Improvements in System Efficiency for Off-Highway Vehicles, Including Construction, Agriculture, and Mining Equipment.

EXHAUST AFTERTREATMENT AND LOW PRESSURE LOOP EGR APPLIED TO AN OFF-HIGHWAY ENGINE

Final Report
March 30th, 2007

Prepared by:
Dr. Kirby J. Baumgard and Dr. Antonio P. Triana
John Deere Power Systems

Dr. John H. Johnson, Dr. Song. L. Yang, and Kiran C. Premchand
Michigan Technological University

John Deere Product Engineering Center
PO BOX 8000
Mail Code 81K
Waterloo, IA 50704

Subcontractors: Michigan Technological University, Houghton, MI

DISCLAIMER

EXECUTIVE SUMMARY

The goal of the project was to demonstrate that low pressure loop EGR incorporating a diesel oxidation catalyst (DOC) and a diesel particulate filter (DPF) can be applied to an off-highway engine to meet Tier 3 (Task I) and Interim Tier 4 (Task II) off-road emissions standards. Task I was completed in 2004 and Task II data collection was completed in 2005 and the final filtration model was completed in 2006.

Task I data was collected using a John Deere 8.1 liter engine modified with a low pressure loop EGR system. The engine and EGR system was optimized and final data over the ISO 8178 eight mode test indicated the NOx emissions were less than 4 g/kWh and the PM was less than 0.02 g/kWh which means the engine met the Tier 3 off-road standard. Considerable experimental data was collected and used by Michigan Tech University to develop and calibrate the MTU-Filter 1D DPF model. The MTU-Filter 1D DPF code predicts the particulate mass evolution (deposition and oxidation) in the diesel particulate filter (DPF) during simultaneous loading and during thermal and NO_2-assisted regeneration conditions. It also predicts the pressure drop across the DPF, the flow and temperature fields, the solid filtration efficiency and the particle number distribution downstream of the DPF. A DOC model was also used to predict the NO_2 upstream of the DPF.

The DPF model was calibrated to the experimental data at temperatures from 230^{o}C to 550^{o}C, and volumetric flow rates from 9 to 39 actual m^3/min. Model predictions of the solid particulate mass deposited in the DPF after each loading and regeneration case were in agreement within +/-10g (or+/-10%) of experimental measurements at the majority of the engine operating conditions. The activation temperatures (Ea/R = 18000 K for thermal, and 14650 K for NO_2-assisted) obtained from the model calibration are in good agreement with values reported in the literature and gave good results in the model calibration by using constant pre-exponential factors throughout the entire range of conditions evaluated. The average clean filter permeability was 2.372×10^{-13} m^2, which is in the range of permeability values reported in the literature. Estimates of the solid particulate mass packing density inside the porous wall were 1 to 5 kg/m^3; and percolation factors were 0.81 to 0.97. Average particulate layer permeability was 1.95×10^{-14} m^2. Solid particulate layer packing density values were between 11 and 128 kg/m^3. These values were in good agreement with the Peclet number correlation theory reported in the literature. NO_2-assisted oxidation of PM in the DPF showed experimentally that a significant reduction of the pressure drop can be achieved (<8 kPa) when sufficient NO_2 (>120 ppm) is available and high exhaust gas temperatures (~360-460^{o}C) can be maintained, even at high PM loadings (low NO_2/solid PM ratios).

The CRT^{TM} (DOC-DPF system) showed limited advantages when used with high PM rates (low NOx/PM ratios) in combination with a low pressure loop EGR strategy for a continuous operation of an engine-exhaust aftertreatment system.

The 8.1-liter engine was not designed for low-pressure loop EGR and when the EGR was added the NOx emissions were reduced but the PM emissions increased. This corresponds to the well known NOx to PM relationship in which if the NOx is reduced the PM emissions increase. In order for this technology to be successful on this engine family, the engine out PM emissions must be reduced. These results led to Task II.

Task II objective was to meet the interim Tier 4 standards using the CCRT™ technology applied to an advanced 6.8 liter John Deere engine. The advanced engine incorporated a 4 valve head, required additional EGR, an advanced high pressure common rail fuel system and a better matched turbocharger. The EGR system was optimized and the goal of less than 2 g/kWh NOx and less than 0.02 g/kWh PM were achieved over the 8 mode test. Again, experimental data was provided to Michigan Tech to study the passive regeneration of the CCRT™ technology.

Two computer models, i.e., the MTU 1-D DOC model and the MTU 1-D 2-layer CPF model were developed as part of this research and calibrated using the data obtained from experiments. The 1-D DOC model employs a three-way catalytic reaction scheme for *CO*, *HC* and *NO* oxidation, and is used to predict *CO*, *HC*, *NO* and NO_2 concentrations downstream of the DOC. The 1-D 2-layer CPF model used "2-filters in series" approach for filtration, *PM* deposition and oxidation in the *PM* cake and substrate wall via thermal (O_2) and NO_2/temperature-assisted mechanisms, and production of NO_2 as the exhaust gas mixture passes through the CPF catalyst washcoat. Results obtained from the 1-D 2-layer CPF model agreed well to experimental data.

PM oxidation efficiency of the DOC-CPF device increased with increasing CPF inlet temperatures due to temperature dependency of NO_2/temperature-assisted and thermal PM oxidation reactions in the CPF, and was higher in the DOC+CPF configuration compared to the CPF configuration due to higher CPF inlet NO_2 concentrations. Overall CPF filtration efficiencies greater than 90% were observed within 90-100 minutes of loading time (starting with a clean filter) at all engine load cases, due to the fact that the *PM* cake layer on the substrate wall forms a very efficient filter.

The bottom line is the MTU models were improved and the models better predict the pressure drop across the DOC and CPF and the models do a good job estimating the amount of PM entering the CPF and the amount oxidized in the CPF and the amount exiting. The idea is to use this information to predict how much soot is in the DPF and predict when active regeneration is needed.

ACKNOWLEDGEMENTS

"*This Report was prepared with the support of the U.S. Department of Energy under Award Numbers DE-FC26-02AL67526. However, any opinions, findings, conclusions, or recommendations expressed herein are those of the authors and do not necessarily reflect the views of the DOE*".

Recognition goes to the entire John Deere Advanced Engine Technology Team for helping in collecting experimental data, specially, Cuong Huynh for his support during the experimental work.

Table of Contents

1. List of Figures, Tables and Definitions

1.1 List of Figures

1.2 List of Tables

Table 20: CPF model input parameters obtained from calibrated CPF model in previous research for 2100 rpm data

Table 21: A comparison of experimentally measured variables and CPF oxidation characteristics between current study and previous research

1.3 TASK I DEFINITIONS, ACRONYMS, ABBREVIATIONS

a : filter cell size (hydraulic diameter of a square channel)
A_{NO2} : pre-exponential factor for the NO_2-assisted oxidation
A_{th} : pre-exponential factor for the thermal oxidation
$c_{p,g}$: exhaust gas specific heat
$c_{p,p}$: solid particulate matter specific heat
$c_{p,s}$ or $c_{p,w}$: cordierite substrate wall specific heat
d_{c0} : clean unit collector diameter
d_c : loaded unit collector diameter
d_{pore}: filter wall pore diameter
D_B : Brownian diffusion coefficient
D_p : diesel exhaust particle diameter
Δx: control volume discretized axial length
E : filter wall collection efficiency
E_{th} : activation energy for thermal oxidation
E_{NO2} : activation energy for NO_2-assisted oxidation
ε_0 : clean filter wall porosity
ε : loaded filter wall porosity
η_D : unit collector diffusion efficiency
η_{DR} : unit collector total filtration efficiency
η_R : unit collector direct interception efficiency
φ : partition coefficient
F : correction factor of the momentum transfer coefficient
f_{CO} : CO selectivity for thermal oxidation
g_{CO} : CO selectivity for NO2-assisted oxidation
h_1 : inlet channel convective heat transfer coefficient
h_2 : outlet channel convective heat transfer coefficient
k : loaded filter wall permeability
k_0 : clean filter wall permeability
k_p : particulate layer permeability
k_{NO2} : reaction rate constant of the NO_2-assisted oxidation
k_s : filter wall permeability
k_{th} : reaction rate constant of the thermal oxidation
K_u : Kuwabara's hydrodynamic factor
L : filter channel length
λ_p : particulate layer thermal conductivity
λ_s : substrate wall thermal conductivity
m_c : solid particulate mass deposited per unit collector
MW_c : Molecular Weight of Carbon
MW_{O2} : Molecular Weight of Oxygen
MW_{mix} : Molecular Weight of the exhaust gas mixture
MW_{NO2} : Molecular Weight of Nitrogen dioxide
NR : dimensionless interception parameter

p_1 : inlet channel gas pressure
p_2 : outlet channel gas pressure
Pe : Peclet Number
ψ : percolation factor
R_{NO2} : Nitrogen dioxide depletion rate
R_{O2} : Thermal oxygen depletion rate
ρ_1 : inlet channel exhaust gas density
ρ_2 : outlet channel exhaust gas density
ρ_w : wall channel exhaust gas density
ρ_p : particulate layer packing density
ρ_{pw} : particulate packing density inside the filter wall
ρ_s : substrate wall bulk density
ρ_w : wall channel exhaust gas density
S_p : Solid particulate specific deposit area
t : time
T_1 : inlet channel exhaust gas temperature
T_2 : outlet channel exhaust gas temperature
T_w : wall channel exhaust gas temperature
U_i : Interstitial velocity
u_1 : inlet channel exhaust gas velocity
u_2 : outlet channel exhaust gas velocity
u_w : wall exhaust gas velocity
w : thickness of the particulate layer
Y_{NO2} : nitrogen dioxide mass fraction
Y_{O2} : oxygen mass fraction

1.4 TASK II DEFINITIONS, ACRONYMS, ABBREVIATIONS

$1-D$: One dimensional
$(.)$: Dimensionless quantity
API : American Petroleum Institute
$BSFC$: Brake-specific fuel consumption
C : (Elemental) Carbon
$C_{16}H_{34}$: n-Hexadecane
C_3H_6 : Propylene
$CCRT^{®}$: Catalyzed Continuously Regenerating Trap (same as $DOC+CPF$)
CH_4 : Methane
CO : Carbon monoxide
CO_2 : Carbon dioxide
CPF : Catalyzed Particulate Filter
$cpsi$: Cells per square inch
$DN-CPF$: Downstream of CPF
$DN-DOC$: Downstream of DOC
DOC : Diesel Oxidation Catalyst
EGR : Exhaust gas recirculation
H_2O : Water
HC : Hydrocarbons
NO : Nitric oxide
NO_2 : Nitrogen dioxide

O_2 : Oxygen
PM : Particulate matter (carbon)
PSD : Particulate size distribution
$SMPS$: Scanning Mode Particulate Sensor
$UP-CPF$: Upstream of CPF
$UP-DOC$: Upstream of DOC

DOC SYMBOLS

$A_{a0,j}$: *'jth'* adsorption factor *(.)*
$A_{a,j}$: *'j^{th}'* adsorption equilibrium factor *(.)*
a: Width of the DOC channel *(m)*
D : Diameter of the substrate *(m)*
$f_{CO}^{catalytic}$: Catalytic *CO* selectivity *(.)*
$f_{CO}^{thermal}$: Thermal *CO* selectivity *(.)*
G_{ca} : Catalytic surface area per unit volume *(m^2/m^3)*
Ga : Geometric surface area of the substrate *(m^2/m^3)*
g_{CO}: *NO_2*-assisted *CO* selectivity *(.)*
L : Channel length *(m)*
$\dot{m}$: Mass flow rate of exhaust gas *(kg/s)*
n : Number of reactions considered in the DOC kinetics model *(.)*
R_{cat} : Reaction rate of catalytic *PM* oxidation *(gmol/m^2-s)*
R_j: Reaction rate of species *'j' (gmol/m^2-s)*
R_{NO_2} : Reaction rate of *NO_2*-assisted *PM* oxidation *(gmol/m^2-s)*
R_{th} : Reaction rate of thermal *PM* oxidation *(gmol/m^2-s)*
Sp : Specific area of particulate *(m^2/m^3)*
T_g : Absolute temperature of the exhaust gas *(K)*
T_w : Absolute temperature of the substrate wall *(K)*
T_∞ : Absolute ambient temperature *(K)*
u : Velocity of exhaust gas *(m/s)*
$\dot{V}$: Volumetric flow rate of exhaust gas *(m^3/s)*
$Y_{g,i}$: Gas-phase mole fraction of species *'j' (.)*
$Y_{s,j}$: Solid-phase mole fraction of species *'j' (.)*
μ_g : Dynamic viscosity of exhaust gas *(Ns/m^2)*
ρ_g : Density of exhaust gas *(kg/m^3)*

CPF SYMBOLS

A_η : Maximum *PM* cake efficiency parameter *(.)*
A_{cat} : Frequency factor for catalytic *PM* oxidation *(m/s-K)*
A_{NO} : Frequency factor for *NO_2* production in the substrate wall *(m/s-K^3)*

A_{NO_2} : Frequency factor for NO_2/temperature-assisted *PM* oxidation in the *PM* cake layer *(m/s-$K^{0.5}$)*

$A_{NO_2,wall}$: Frequency factor for NO_2/temperature-assisted *PM* oxidation in the substrate wall *(m/s-$K^{0.5}$)*

A_{th} : Frequency factor for thermal *PM* oxidation *(m/s-K)*

a : Width of the CPF channel *(m)*

$C_{in,std}$: Standard inlet *PM* concentration *(mg/std.m^3)*

$d_{c,cake}$: Diameter of *PM* cake layer collector *(m)*

Ea_{cat} : Activation energy for catalytic *PM* oxidation *(J/kmol)*

Ea_{NO} : Activation energy for NO_2 production in the substrate wall *(J/kmol)*

Ea_{NO_2} : Activation energy for NO_2/temperature-assisted *PM* oxidation (in *PM* cake layer and substrate wall) *(J/kmol)*

Ea_{th} : Activation energy for thermal *PM* oxidation *(J/kmol)*

k_p : *PM* cake layer permeability *(m^2)*

$k_{t,0}$: Clean trap (substrate wall) permeability *(m^2)*

$\dot{V}_{std}$: Standard exhaust volumetric flow-rate *(std.m^3/s)*

ΔP_i : Initial pressure drop *(kPa)*

ε_0 : Clean porosity of the (CPF) substrate *(.)*

η_c : *PM* cake layer collector efficiency *(.)*

$\frac{\eta_c}{d_{c,cake}}$: *PM* cake collector efficiency ratio parameter *(m^{-1})*

$\rho_{p,w}$: *PM* packing density in the wall *(kg/m^3)*

ρ_p : *PM* cake layer packing density *(kg/m^3)*

ψ : Percolation factor *(.)*

2. INTRODUCTION

The goal of this project was to demonstrate that low-pressure loop EGR incorporating an oxidation catalyst and a particulate filter could be applied to an off-highway engine to meet the Tier 3 and Interim Tier 4 standards.

The project objectives for Task I were to:

1) Demonstrate that 4 g/kWh NOx +HC and 0.020 g/kWh PM emission levels can be achieved over the ISO 8178-test cycle using cooled low pressure loop EGR and a diesel particle filter (DPF). This required optimizing the EGR strategy for NOx reduction and also optimizing the engine for best BSFC.
2) Measure the exhaust particle size distributions for both baseline and with the EGR/DPF emission control system over the ISO 8178-test cycle.
3) Determine the steady-state loading curves and the balance point regeneration temperatures for various operating conditions. Incorporate this data into the MTU aftertreatment model.
4) Identify optimum regeneration control strategies. Determine how the engine and aftertreatment system can be operated to achieve the required temperatures for regeneration.

The project objectives for Task II were:

1) Use an advanced 6.8 liter 4 valve engine with an advanced high pressure common rail fuel system using low pressure loop EGR and an advanced combustion system to minimize BSFC and still meet the emission standards of 2.0 g/kWh NOx and 0.02 g/kWh PM.
2) Measure the exhaust particle size distributions for both baseline with EGR and with the EGR/DPF emission control system over the ISO 8178-test cycle.
3) Update the MTU models developed for task I and determine if they still applied with the high rates of EGR in task II.
4) Identify regeneration control strategies.

Task I of the current contract evaluated the feasibility of using a low-pressure loop exhaust gas recirculation (EGR) system in combination with a high efficiency diesel particulate filter (DPF) to reduce the oxides of nitrogen (NOx) to the Tier 3 off-highway standards. By removing the EGR gas downstream of the DPF the clean gas can be routed to the upstream side of the turbocharger and because the exhaust is free of particles there is no abrasive wear on the turbo compressor wheel or fouling of the engine's intercooler.

The major driving force for continuing task II of the project was to meet the interim Tier 4 off-road diesel emission standards while maintaining or improving Tier 3 fuel economy. The interim Tier 4 standard requires an additional 50% NOx reduction and a 90% particulate reduction from Tier 3. Figure 1 shows the various tiers of emission regulations and the target for this research is the interim Tier 4 standard which is 2 g/kWh NOx and 0.02 g/kWh particulate starting in 2011. The Non-Road standards were finalized May 10, 2004.

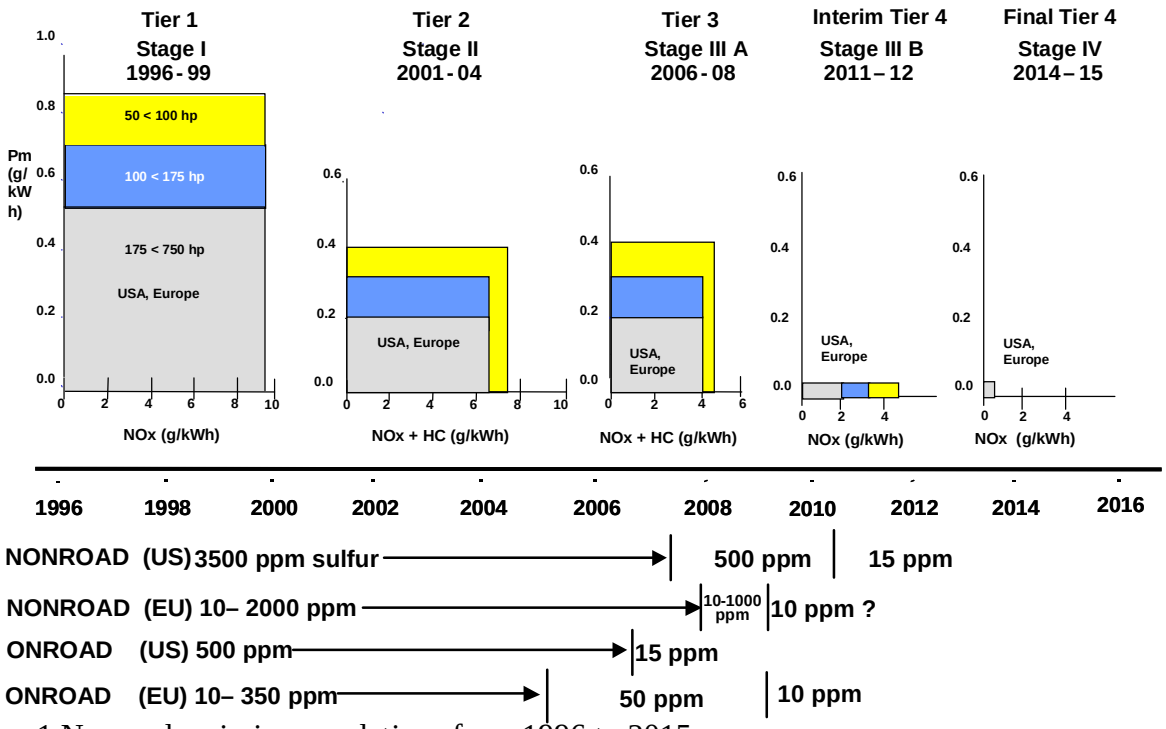

Figure 1 Nonroad emission regulations from 1996 to 2015.

Task II consisted of laboratory testing and computer modeling since the technology was already identified during task I. The testing was performed in John Deere's state-of-the-art test cells. The cells have the latest General Electric AC dynamometers that are computer controlled with automatic data collection. The cells have full emission benches along with partial flow dilution tunnels. Because the size of diesel particles may be a potential health concern and because EPA is considering regulating particle number concentrations, the particle size distributions from 0.005 to 1.0 microns in diameter were measured using an SMPS system. To determine the percent EGR, the test cell was equipped with two CO_2 analyzers. One was used to measure the raw exhaust concentration and the other the intake manifold concentration. By correcting for background levels and taking the CO_2 ratio, the fraction of EGR was determined.

The DOC and DPF models for predicting pressure drop and regeneration characteristics were developed during task I, and were used in conjunction with the data collected for task II. During task II the amount of NO_2 available for regeneration was considerably less and the DOC model had to be verified at these NO_2 levels.

A John Deere 6068H 187kW engine was used for task II, a more advanced engine than was used for task I (6081H 175 kW). The engine's displacement is 6.8 liters and is turbocharged and intercooled. It incorporates the latest high-pressure common rail fuel injection system, 4 valves per cylinder and is fully electronic. A Johnson Matthey catalyzed continuously regenerating diesel particle filter (DOC-CDPF) was placed downstream of the turbocharger. A portion of the exhaust gas downstream of the DPF was recirculated to the intake system and the amount controlled using a special EGR valve. An EGR cooler was incorporated to cool the EGR exhaust gas.

The major challenge for this part of the project was lowering the NOx emissions to 2 g/kWh over the 8178 eight-mode test. This required EGR rates between 18-22%, approximately 50% greater than those used for task I. In order to keep the PM emissions under control the A/F ratio had to be maintained greater than 20 with the addition of EGR. This was maintained by using a fixed turbocharger with a large compressor and small turbine housing (0.64 A/R) that provided sufficient boost at those EGR rates.

Adding EGR lowers the NOx emissions and increases the particulate emissions. In order for the DOC-CDPF to be self-regenerating the NOx:PM ratio needs to be about 20:1. During task I it was determined that the NOx:PM ratio was much less than 20:1, therefore, passive regeneration did not occur under all conditions. For task II, modifications to the air system and the combustion system were made to obtain the proper NOx : PM ratio. This was accomplished by performing turbocharger matching, increasing the fuel rail pressure and changing the fuel injectors. By optimizing both the air and combustion system the NOx : PM ratio was sufficient. More importantly, the BSFC vs. NOx tradeoff was optimized leading to lower BSFC.

This report presents the experimental and modeling results from two types of exhaust aftertreament systems (CRT and CCRT) and two different engines. Task I incorporated the CRT technology using a Tier 1 8.1 liter engine with an experimental low pressure loop EGR system. DPF loading tests, with and without an upstream DOC, conducted as part of a Department of Energy Contract with John Deere Power Systems in which Michigan Technological University was subcontracted to perform the modeling research.

3. TASK 1

3.1 MODEL DEVELOPMENT

The DPF model describes the solid particulate matter deposition and oxidation mechanisms occurring in a DPF using kinetic and filtration models together with equations derived from applicable conservation laws (mass, momentum, and energy). The model describes the filtration, flow field, temperature field, pressure drop, and regeneration characteristics (thermal and NO_2-assisted) occurring in a DPF under simultaneous solid particulate matter accumulation and depletion conditions. This model was developed from the CPF two-layer modeling effort by Huynh et al. [2,3] in which a NO_2-assisted regeneration model inside the inlet channels and the porous walls has been incorporated to account for the high solid PM oxidation rates in the DPF. The MTU Filter 1D 2-layer model recently developed and used in this paper is described in detail in reference [23], and therefore only limited equations have been included in the present paper.

3.1.1 Pressure Drop across the Filter Wall

The pressure drop across a porous wall for the flow through clean and loaded diesel particulate filters is represented using Darcy's Law from [2-4]:

$$p_1 - p_2 = \frac{\mu(T_w)}{k_p} u_w w + \frac{\mu(T_w)}{k_s} u_w w_s \tag{1}$$

where p_1 and p_2 are the inlet and outlet channel gas pressures at the x (axial) location respectively, k_p is the permeability of the particulate deposit layer, k_s is the permeability of the porous wall, w is the thickness of the particulate deposit layer, w_s is the thickness of the porous wall, and μ is the dynamic viscosity of the exhaust gas mixture.

With the mass, momentum and energy conservation equations in the inlet and outlet channels, together with the pressure drop across the filter walls, the flow field can be solved numerically to obtain the velocity profiles in the inlet and outlet channels, and the pressure drop across the entire DPF. The filtration process will significantly affect the properties controlling the pressure drop characteristics across the DPF and the solid particulate matter depletion (layer shrinkage) will also have a controlling effect on it.

3.1.2 Solid Particulate Mass Conservation

The conservation of species can be expressed in molar concentration terms as:

$$\frac{\partial([X_n])}{\partial t} + \frac{\partial([X_n]u_w)}{\partial y} = \dot{\omega}_n \tag{2}$$

The convective effects dominate the species transport in the porous wall [5]. It is assumed that the concentration of any species in the inlet channel is unaffected by the depletion of species in the reactive deposit layer [5]. Due to the gases short residence time and high velocity in the inlet and outlet channels, chemical reactions in the inlet

channel are assumed to be negligible. The mole fraction of each species in the inlet is assumed to be constant and equal to the inlet concentration.

It can be observed from equation (2) that the time rate of change of the species molar concentration is governed by the balance between convective transport in the y-(radial) direction and the chemical kinetics in the particulate layer. It is assumed that the reactions are kinetically controlled due to the extremely small passages in the particulate layer and porous wall, which according to experimental results from Bisset [2-7], gave estimates of mass transfer rates two orders of magnitude higher than the chemical reaction rates at the highest temperatures.

Assuming 1st order reaction with thermal oxidation only, setting the mixture density $\rho=\rho_w$, the O_2 conservation equation in mass fraction terms is [5]:

$$\frac{\partial(\rho_w Y_{O_2})}{\partial t} = -\frac{\partial(\rho_w Y_{O_2} u_w)}{\partial y} - k_{th}\rho_w Y_{O_2} \tag{3}$$

where Y_{O2} is the oxygen mass fraction of the inlet gas, u_w is the wall flow velocity, $k_{th}(T_w) = A_{th}T_w \exp\left(-\frac{E_{th}}{\overline{R}T_w}\right)$ is the reaction rate constant of the modified Arrhenius form, in which A_{th} is the pre-exponential factor, and E_{th} the activation energy.

If quasi-steady state is assumed, then the O_2 species conservation equation is:

$$\frac{\partial(\rho_w Y_{O_2} u_w)}{\partial y} = -k_{th}\rho_w Y_{O_2} \tag{4}$$

The rate of oxygen depletion per unit wall surface area (m^2) can be obtained by integrating the O_2 species conservation equation above.

$$R_{O_2} = \int_0^w S_p \rho_w Y_{w_{O_2}} k_{th}(T_w) dy \tag{5}$$

where *Sp* is the specific deposit area [5,8], Y_{wO2} is the oxygen mass fraction at the wall, and y is the normal direction of the filter wall.

Solving the integration we have [5]:

$$R_{O_2} = \rho_w u_w Y_{O_2}(0,t) * \left[1 - \exp\left(\frac{-S_p k_{th} w}{u_w}\right)\right] \tag{6}$$

In a similar form, the nitric dioxide species conservation equation species can be derived:

$$\frac{\partial(\rho_w Y_{NO_2} u_w)}{\partial y} = -k_{NO_2} \rho_w Y_{NO_2} \tag{7}$$

where now, the Y_{NO2} represents the NO_2 mass fraction, k_{NO2} the reaction rate constant of the NO_2-assisted oxidation with its corresponding modified Arrhenius form where A_{NO2} is the pre-exponential factor and E_{NO2} the activation energy as shown in the following equation.

$$k_{NO_2}(T_w) = A_{NO_2} T_w \exp\left(-\frac{E_{NO_2}}{\overline{R} T_w}\right) \tag{8}$$

As with the O_2, the NO_2 depletion rate can be expressed as:

$$R_{NO_2} = \int_0^w S_p \rho_w Y_{w_{NO_2}} k_{NO_2}(T_w) dy \tag{9}$$

where Y_{wNO2} is the nitric dioxide mass fraction at the wall, and y is the normal direction through the filter wall. Integrating the equation above we have the NO_2 depletion rate in terms of the gas density in the wall ρ_w, wall flow velocity u_w, inlet NO_2 mass fraction and the reactive term in exponential form:

$$R_{NO_2} = \rho_w u_w Y_{NO_2}(0,t) * \left[1 - \exp\left(\frac{-S_p k_{NO_2} w}{u_w}\right)\right] \tag{10}$$

Both the O_2 and NO_2 depletion rates have units of mass fraction of O_2 or NO_2 per unit time per unit wall surface area.

With the chemical reactions involved in the particulate matter oxidation process shown above, the particle depletion rate (with units of: mass of PM per unit time per unit particulate layer area) can be expressed as follows:

$$\frac{\partial(\rho_p w)}{\partial t} = -\left(\frac{MW_c}{MW_{O_2}} \cdot R_{O_2} + \frac{MW_c}{MW_{NO_2}} \cdot R_{NO_2}\right) \tag{11}$$

where MW_c, MW_{O2}, and MW_{NO2} are the molecular weights of the solid particulate matter, oxygen and nitric dioxide respectively. R_{O2} and R_{NO2} are the oxygen and nitric dioxide depletion rates respectively. ρ_p is the particulate layer packing density and w the particulate layer thickness.

The particulate mass balance above can be solved numerically to estimate the regeneration characteristics of the filter with the thermal oxidation mechanism, and with and without the NO_2-assisted oxidation mechanism. In the two-layer model developed by Konstandopoulos et al. [7] and coded by Hasan et al. [2,3], the particulate layer thickness is divided into a catalytic layer w_1 and a thermal layer w_2 on top of the catalytic layer [2,3,7]. Using this same approach, an approximation can be performed to estimate the oxidation inside the porous wall, by accounting for the mass accumulated inside the wall, and determining an equivalent thickness that represents a particulate layer in the wall

[9,23]. The “in the wall” particulate layer mass balance can be solved similarly as the particulate layer on the wall. Simulation results of this sub-model are presented in the Results & Discussion section. To determine the thickness of the particulate layer *w*, it is necessary to understand the deposition and filtration mechanisms in the filter, which have been extensively explained in the literature in references [2,3,4,6,7,9,10,11,12,13,14], and for such reason the mathematical equations describing such mechanisms have not been included in this paper.

3.2 EXPERIMENTAL PROCEDURES

To collect the necessary data and to calibrate the DOC and DPF models, a series of experiments were designed and conducted on two different research projects. The first project determined the emissions characteristics of the DOC over a wide range of engine operating conditions [15], and the second project, involved a series of DPF loading experiments at several engine operating conditions, with and without the DOC upstream of the DPF.

3.2.1 Engine, Fuel, and Test Cell Instrumentation

The engine used for this project was a John Deere 8.1 liter 175 kW @ 2200 rpm, 1060 N-m @ 1400 rpm, 4 stroke, 6-cylinder in-line, turbocharged and after-cooled with a high-pressure common rail fuel injection system and an electronic control unit with variable injection timing. For the DOC experiments no EGR was used, but for the DPF and CR-DPF testing, a cooled low-pressure loop EGR strategy was used.

A state-of-the-art test cell at the John Deere Product Engineering Center was used for all experiments. This test cell has a full emissions bench with Horiba 200 series analyzers. The CO and CO_2 instruments use the non-dispersive infrared detectors, the NOx analyzer uses the chemiluminescence principle, the HC analyzer uses the heated flame ionization detection (FID) method, and the O_2 instrument is a paramagnetic detector. The particulate sampling system uses the Sierra BG-2 partial flow dilution system. The exhaust gases are diluted between 8 to 10 to 1 depending on the engine operating conditions and then the particulate matter is deposited on a 70 mm Pallflex TA60 filter by drawing a diluted sample with a flow rate of 110 std L/min. The 70 mm filters are pre-baked, weighed in a humidity and temperature controlled room, taken to the test cell for sample collection, returned to the conditioned room and then re-weighed. The particulate samples are then baked in a vacuum oven at 200°C for 2 hours, re-conditioned and re-weighed for determining the volatile particulate portion by the difference from the first weighing.

The 6081H engine was connected to a 750 hp General Electric AC dynamometer controlled with a Digalog Testmate controller. The test cell computer controls the engine’s speed and load, records all the test cell data and controls the emissions bench. The test cell supplies conditioned air to the engine, which is at 10.71 g H_2O/kg air and 25°C. Diesel fuel was supplied in 350 gallon totes and was pumped into a day tank. The mass flow rate of fuel to the engine was measured with an AVL 721 fuel weigher. All temperatures were measured using k-type thermocouples and pressures were measured with Sensotec transducers. Engine intake air humidity was measured using General Eastern dew point meters. An ultra low sulfur diesel fuel with less than 15 ppm was selected for all experiments in order to avoid excessive sulfate particulate formation in the DOC due to the catalytic reaction and also to reduce the inhibition effect of SO_2 on the NO conversion to NO_2.

Particle size distribution data were collected using a TSI Model 3936 Scanning Mobility Particle Sizer (SMPS) system, which is capable of measuring particle sizes in the range of 5 nm to 1000 nm. The SMPS system uses an electrical mobility detection technique. An Electrostatic Classifier (EC) charges particles to a known charge distribution and then classifies them according to their ability to pass through an electrical field, and a Condensation Particle Counter (CPC) measures their concentration. Size distribution plots can be obtained by using a PC with custom software from TSI to perform the data reduction (TSI Manual). Particle size distributions were collected upstream and downstream of both the DPF and of the complete DOC-DPF unit during every filter loading experiment. No particle size distribution data were collected for the DOC testing as the instrumentation was not yet available for those experiments. Two secondary dilution systems, consisting of four air ejectors (two series of two), two for the upstream sampling and two for the downstream sampling were used to dilute the sample. The inlet orifice diameters in the ejectors were designed to approximate isokinetic sampling conditions from the exhaust pipe and to obtain dilution ratios in the range of 10-500 to 1 depending on the sampling port. A thermodenuder was installed between the dilution system and the SMPS to remove the HC and sulfates to minimize the homogeneous nucleation of nano-particles [3]. Figure 2 shows a schematic representation of the dilution system setup.

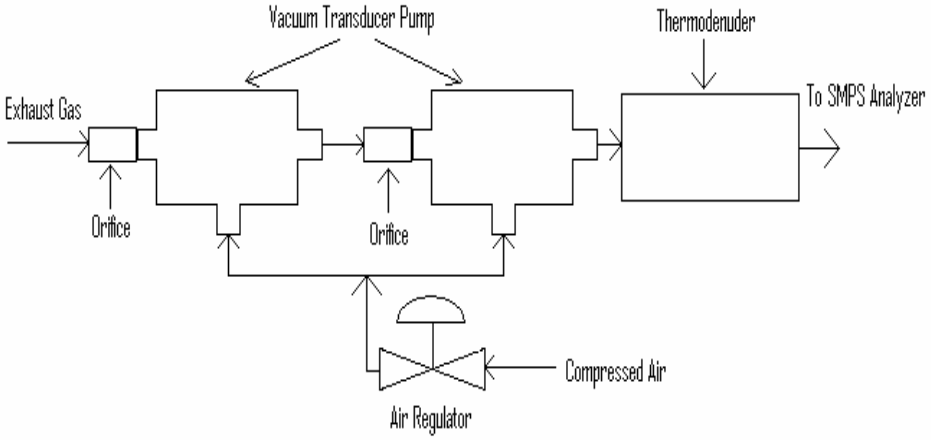

Figure 2 Schematic of the Dilution Sampling System. Adapted from Huynh [3]

For the DOC experiments, the DOC was mounted in the exhaust stream approximately 2 meters from the engine. The exhaust pipe from the engine to the inlet of the DOC was insulated.

3.2.2 DOC and DPF Specifications

The diesel oxidation catalyst and diesel particulate filter used in the experiments were from a Johnson Matthey CR-DPF. All substrates were made of cordierite material with square channels. The DOC was a 10.5 in D x 6 in L with cell density of 300cpsi and 0.19 wall thickness. Two DPF's of 10.5 D x 12 in L with cell densities of 100cpsi and 200cpsi, and wall thicknesses of 0.43 and 0.31 mm respectively.

3.2.3 DPF Testing and Sampling Procedures

DOC testing and sampling procedures were described in SAE 2003-01-3176 [15] which reported the DOC experiments and modeling work performed prior to the DPF testing.

To calibrate the DPF model controlling parameters, the work of Huynh [2,3] was followed and adapted to the present experimental research work. The objective of the DPF loading experiments is to generate the input variables required for the filtration/oxidation model, as well as, to measure key output variables of the DPF. The input variables are: exhaust temperature, exhaust volumetric flow rate, gaseous and particulate emissions, and particle size distributions. The output variables are: pressure drop across the DPF, gas and solid temperatures, gaseous and particulate emissions, and the particulate mass retained in the filter. These data are used to calibrate the filtration/oxidation model in order to determine the DPF filtration parameters, the reaction kinetics constants, and the particulate deposition characteristics.

A total of 20 steady state DPF loading experiments were performed and used to calibrate the DPF model developed in this research. Four experiments with the 100cpsi DPF were performed at 2200 rpm and 25,50,75, and 100% loads. When this filter failed during the baking process after the fourth experiment, a new 200cpsi was selected and these experiments were repeated, and then the remaining 12 experiments were performed. 12 experiments were performed without the DOC installed upstream of the DPF, and 8 with the DOC installed to test the complete DOC-DPF unit.

Each experimental loading test was performed as follows: Starting with a "clean" filter, the DPF was loaded by passing exhaust flow through the DPF for a period of time. For the majority of the loading experiments, the engine was started and operated at the desired speed at 100 N-m load for 60 seconds. Then the engine was ramped to the desired condition. The time to reach the initial condition varied between experiments.

The mass deposited in the filter was measured by weighing the filter before and after each loading experiment. Before each new experiment the filter was baked by placing the filter in a high temperature oven, ramping the temperature up to 650^{o}C over 2 hours, baking at 650 for 4 hours and then cooling for 4 hours. The filter was weighed using a scale with the capability of measuring down to 1 gram. Before each weighing a 10 kg and a 5 kg calibration weight was used to check the accuracy of the scale. The scale always measured the calibration weights to within 1 gram. The filters were typically weighed at temperatures greater than 150^{o}C to minimize humidity effects.

During the loading phase a minimum of three downstream particulate matter concentrations samples were taken, the number of samples varied as the sampling technique was changed from the 100cpsi filter testing to the 200cpsi filter testing.

The particulate number distribution samples were taken at the same time of the particulate matter concentrations samples. In the case of the particle size distribution, a minimum of three upstream and downstream samples were taken during each experiment. The upstream particulate matter concentrations had to be taken in a separate run without the DPF installed, this was achieved by simulating the pressure drop across the DPF with the aid of a restriction valve instead of the actual DPF. The pressure drop was varied by closing the valve and restricting the flow until pressure drop readings were similar to those of the DPF during loading experiments and a minimum of three samples were taken and averaged.

Solid particulate matter concentration measurements were made with both sampling techniques (raw and diluted), the data were compared and agreement within 10% was obtained with both techniques. For this, it was decided to use the diluted technique to allow faster, earlier, and more samples during the loading experiments. This approach

allowed a downstream particulate concentration sample in the early stage of the loading experiment to determine the filtration efficiency during the deep bed filtration stage. During the testing of the 100cpsi filter, a raw sampling technique was used, but during the testing of the 200cpsi filter, the diluted technique employed by John Deere was preferred for the reasons explained above.

3.3 Results and Discussion

3.3.1 DPF Model Calibration

Figure 3 shows the correlation between the predicted and experimental clean pressure drop across the DPF for each of the 20 test conditions tested. The reason why only 15 experimental points, instead of 20 can be observed in the graph in Figure 3 is due to the fact that clean pressure drop values at 0.6, 1.1, 1.5, 1.8, and 2.6 kPa were overlapped from different experiments. The controlling parameter that determines the "clean" pressure drop across the DPF are the wall permeability, exhaust gas temperature, and actual volumetric flow rate.

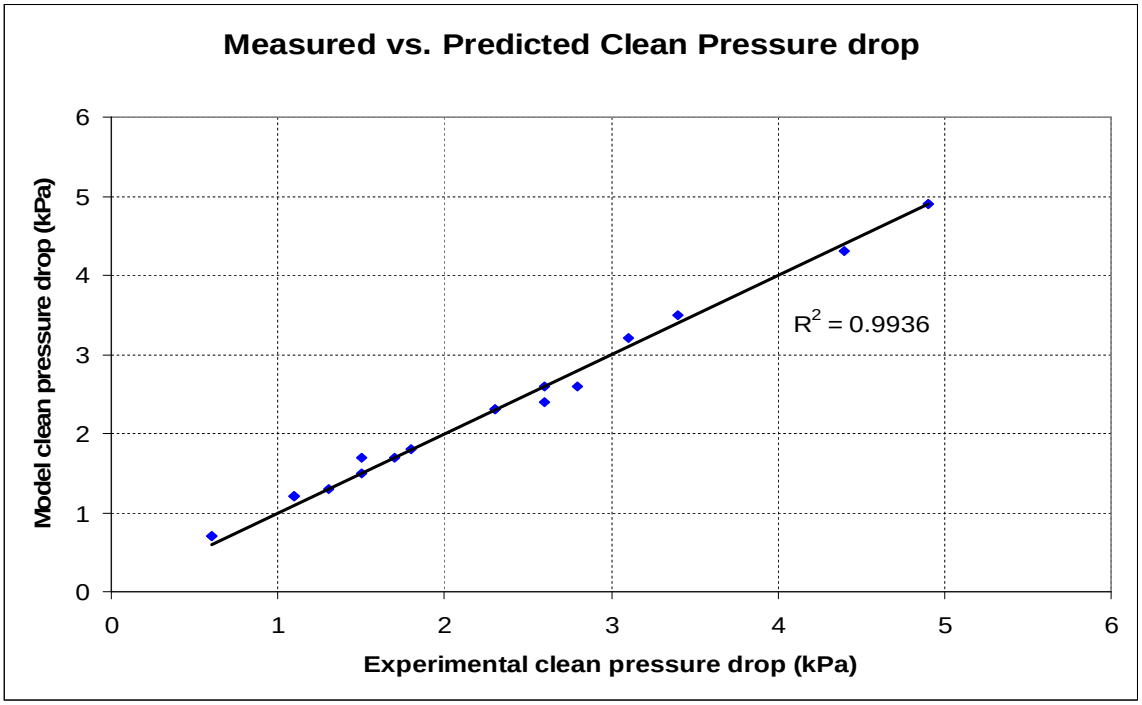

Figure 3 Correlation of Measured vs. Predicted clean pressure drop across the DPF.

Figure 4 illustrates the clean wall permeability values determined in the model calibration for each experiment, and its deviation from the mean. In theory, the clean wall permeability of a DPF should be constant, however, in our case, the determination of such parameter varied due to the inadequate selection of the initial condition point from each experiment. Also, due to the different stabilization times of each loading condition, and of the baking process of the filter, the pre-test filter weight was in most cases within +/- 2 grams of the average filter weight. But in a few conditions, the pre-test weight varied more than 3 grams from the average value, indicating that the filter may have not been completely clean prior to that particular experiment, therefore the initial wall permeability slightly varied from experiment to experiment. The average "clean" filter permeability was 2.169E-13 m^2, with a 2 standard deviation of 1.007E-13 m^2. These

values agree well with those reported in references [2,3,7], although the larger variation reported in this work is due to the procedures explained above.

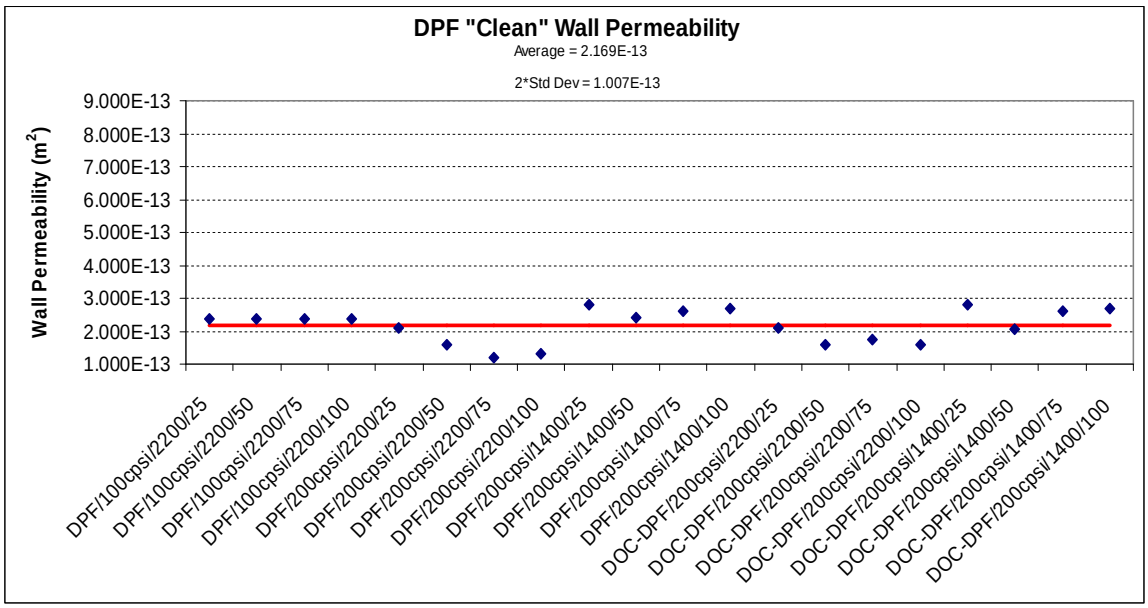

Figure 4 Filter "Clean" Wall Permeability for each of the 20 DPF experiments.

Figure 5 shows the correlation between the predicted mass retained in the filter and the measured. Most measured values agree well with the estimated solid PM mass from the PM samples, except for some cases in which the DPF weights, after their respective experiments, were performed once the DPF had cooled down, and the excess weight most likely was caused by water condensation in the ambient resulting in higher error in the measurements. This error was not significant as it did not affect the determination of the model calibration parameters.

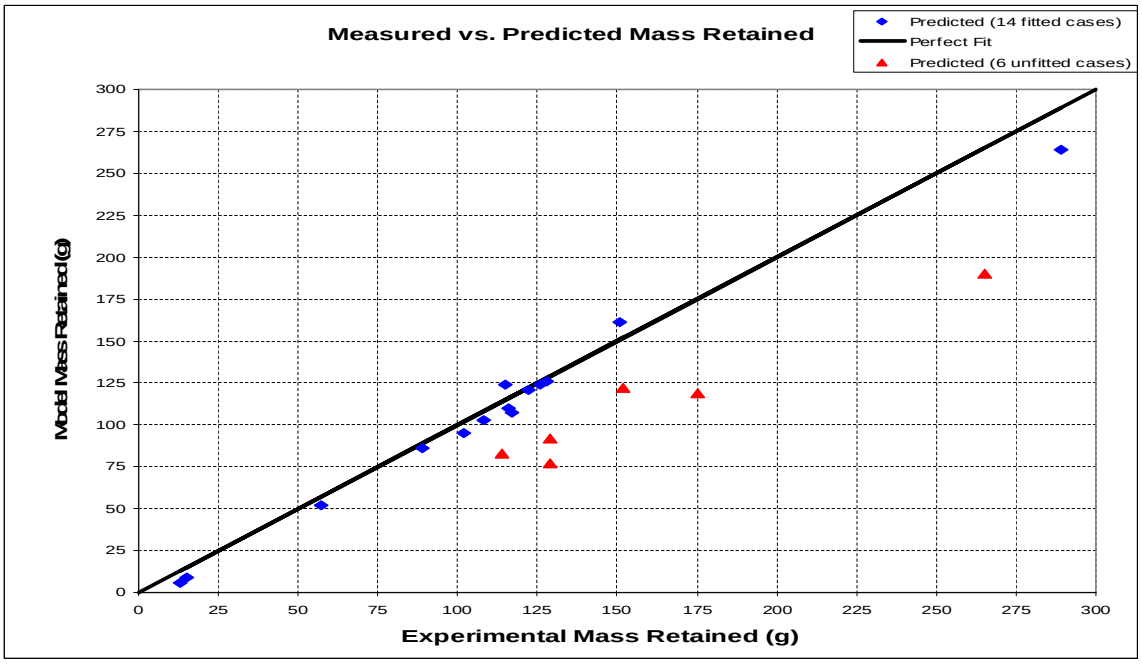

Figure 5 Correlation between Measured vs. Predicted soot mass retained in the DPF.

Two parameters that control the pressure drop characteristics in the deep-bed filtration stage are the percolation factor and the wall solid particulate matter packing density. Figure 6 shows the percolation factor for each of the 20 experiments performed. The average percolation factor identified for all experiments was 0.887, with a 2 standard deviation of 0.108. These results are in agreement with values reported in references [2,3,7].

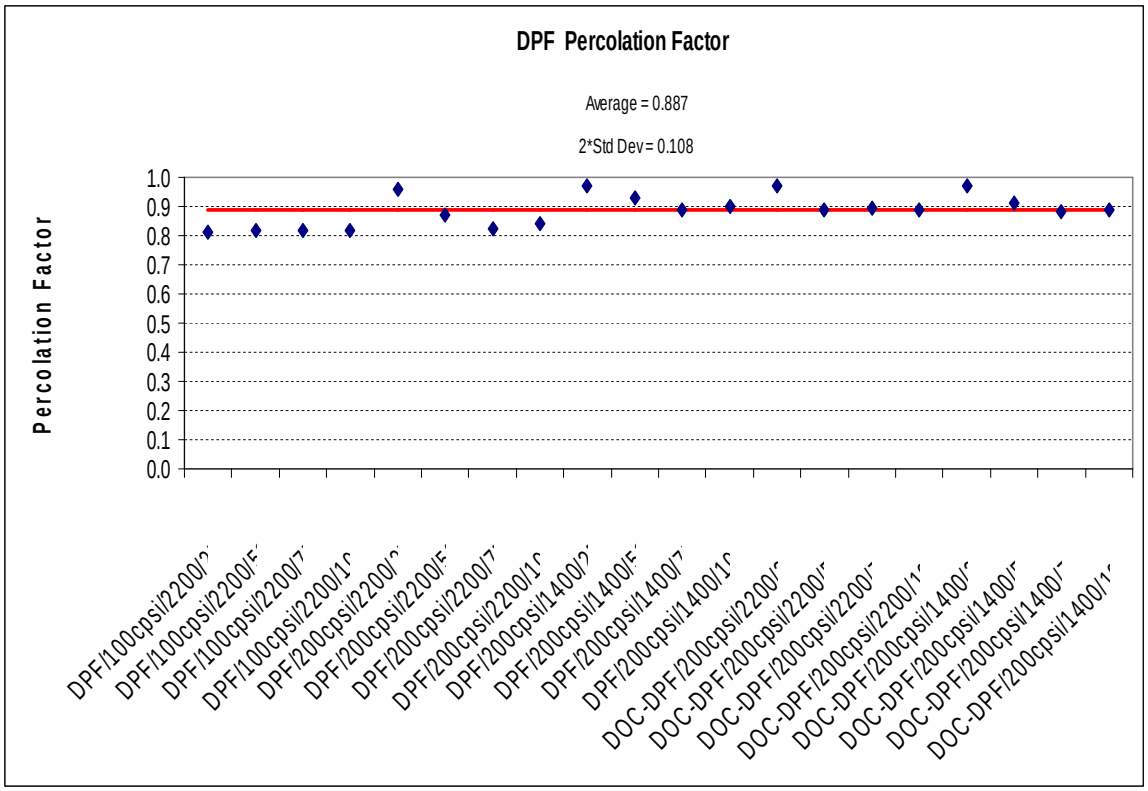

Figure 6 Percolation Factor for each of the 20 DPF experiments.

The results of the solid particulate packing density in the wall are also in agreement with those reported in references [2,3,7] as it can be observed in Figure 7. An average solid particulate packing density of 3.0 kg/m^3 was determined. The difference in values of packing densities between the 4 100cpsi and 16 200cpsi filter experiments was due to the geometry and properties of each filter type, which affect the deposition mechanism, channel and wall flow velocities. Wall soot packing densities between 1 and 4 kg/m^3 were found for the 200cpsi experiments, and a constant value of 5 fitted well to the 100cpsi cases.

The parameters that affect the layer cake filtration stage in the filter loading process, and have a direct impact in the linear pressure drop increase are: the packing density, and permeability of the solid particulate matter in the form of layers deposited on the walls inside the inlet channels of the DPF.

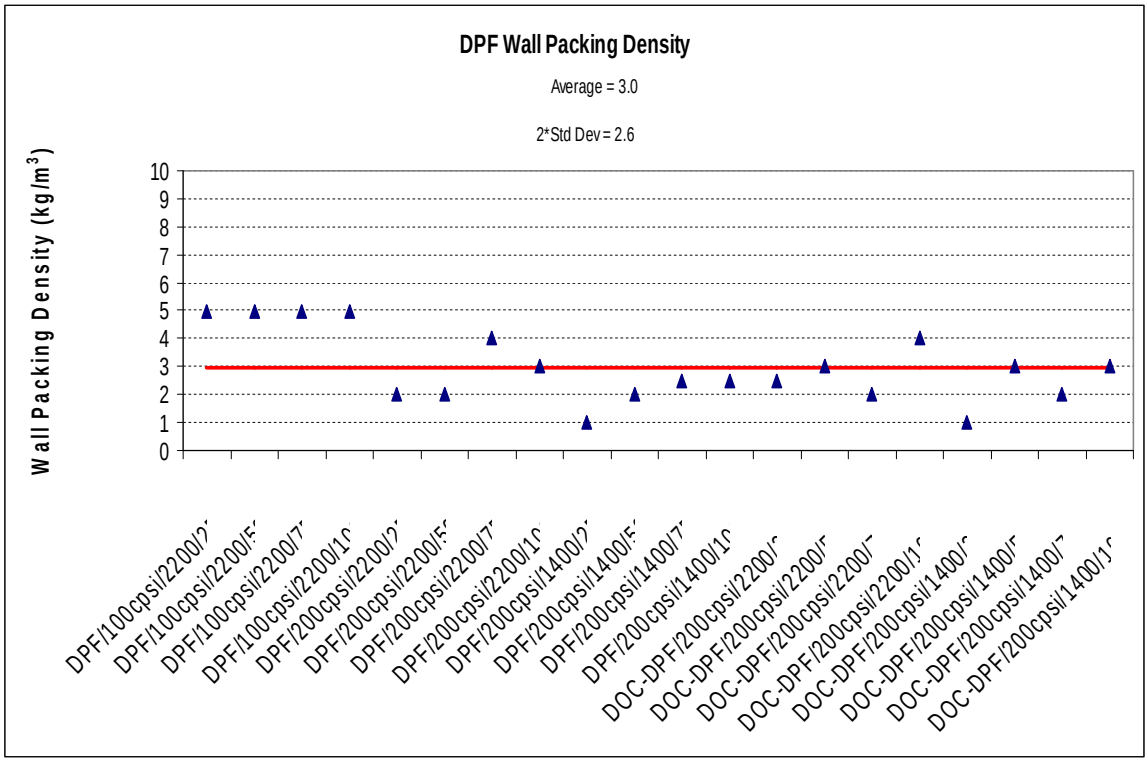

Figure 7 Filter Wall Packing Density for each of the 20 DPF experiments.

Konstandopoulos et al. [16] presented a study of the growth process in solid particulate layers in diesel particulate filters, which describes the relation between the solid particulate matter properties (packing density, porosity, permeability) and a dimensionless parameter (Peclet number) that measures the relation between convective and diffusive transport in particulate flows.

Peclet number (Pe) is a dimensionless parameter that correlates the microstructure of the solid particulate deposits and the process in which such particulates were deposited inside a filter. High Pe numbers are representative of compacted microstructures (higher packing densities), similarly, low Pe numbers are of more porous structures (lower packing densities) [16]. Peclet number is defined as:

$$Pe = \frac{v_w \cdot d_{primary}}{D_p}$$

where v_w is the wall flow velocity, $d_{primary}$ is the primary solid particulate matter diameter, and D_p is the Diffusion coefficient [16].

Huynh et al. [2,3] found good agreement with their model calibration data and the Konstandopoulos's correlations [16]. In the present research work, such correlations have been employed to compare against the model calibration parameters found in our modeling effort.

In the present work, Peclet number varied from 0.25 to 0.83 for all 20 experiments performed with the 100cpsi and 200cpsi DPF. The 200cpsi filter, having more and smaller channels than the 100cpsi filter, presented lower Pe numbers than the 100cpsi, under similar engine operating conditions. Figure 8 shows the packing density vs. Peclet Number used for model calibration of each of the 20 conditions studied.

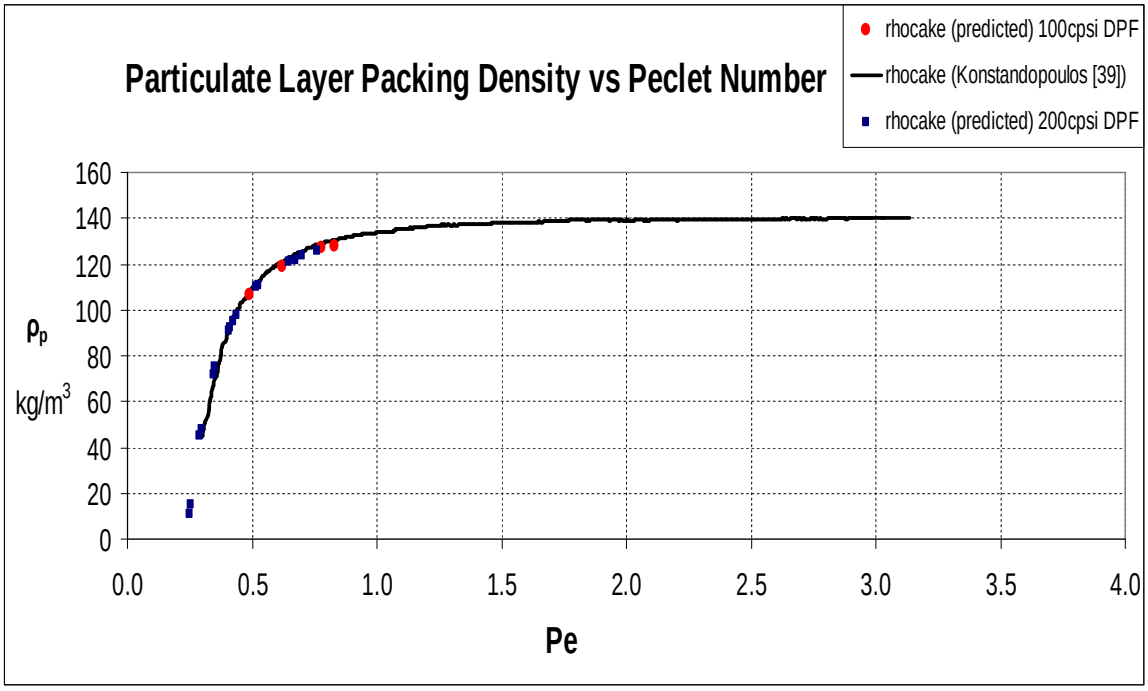

Figure 8 Particulate layer packing density vs. Pe Number

Similarly, the particulate layer porosity and permeability as a function of the Peclet number are shown in Figures 9 and 10 respectively. Good agreement with the theory of Konstandopoulos et al. [16] was found from the model calibration for the packing density and porosity of the solid particulate mass in the filter at all operating conditions. Particulate layer permeability values were on average 1.95×10^{-14} m^2, which agree well with values reported by Huynh et al. [2,3], and Konstandopoulos et al.[7,16]. For the cases where NO_2-assisted oxidation was significant, the particulate layer permeability was much larger as can be observed in Figure 10.

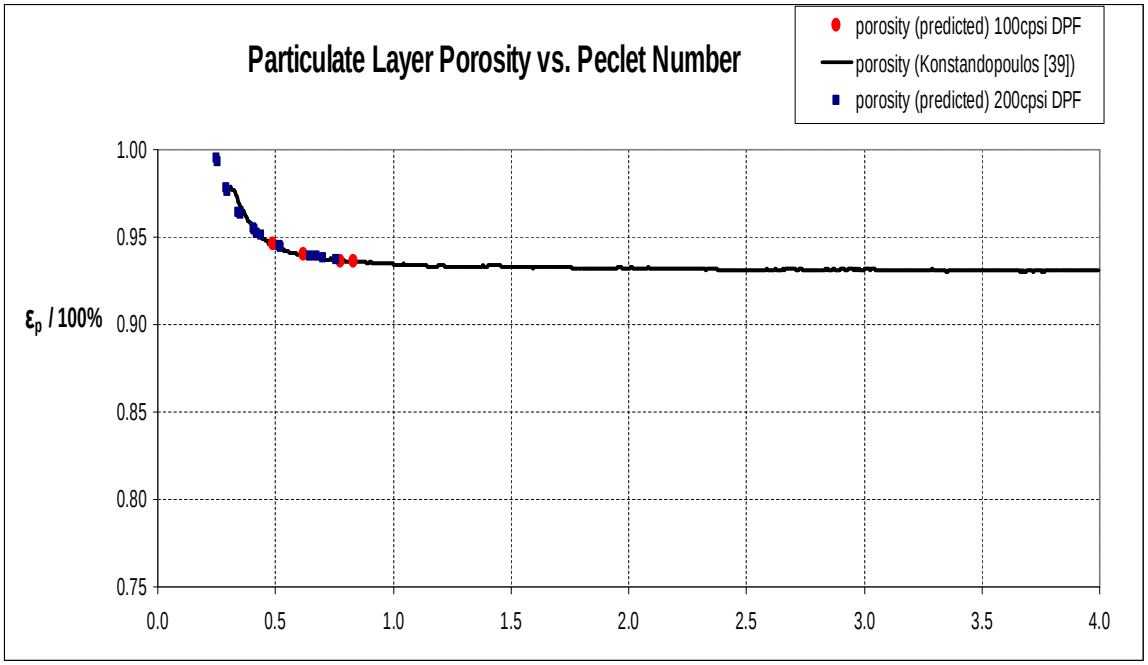

Figure 9 Particulate layer porosity vs. Pe Number.

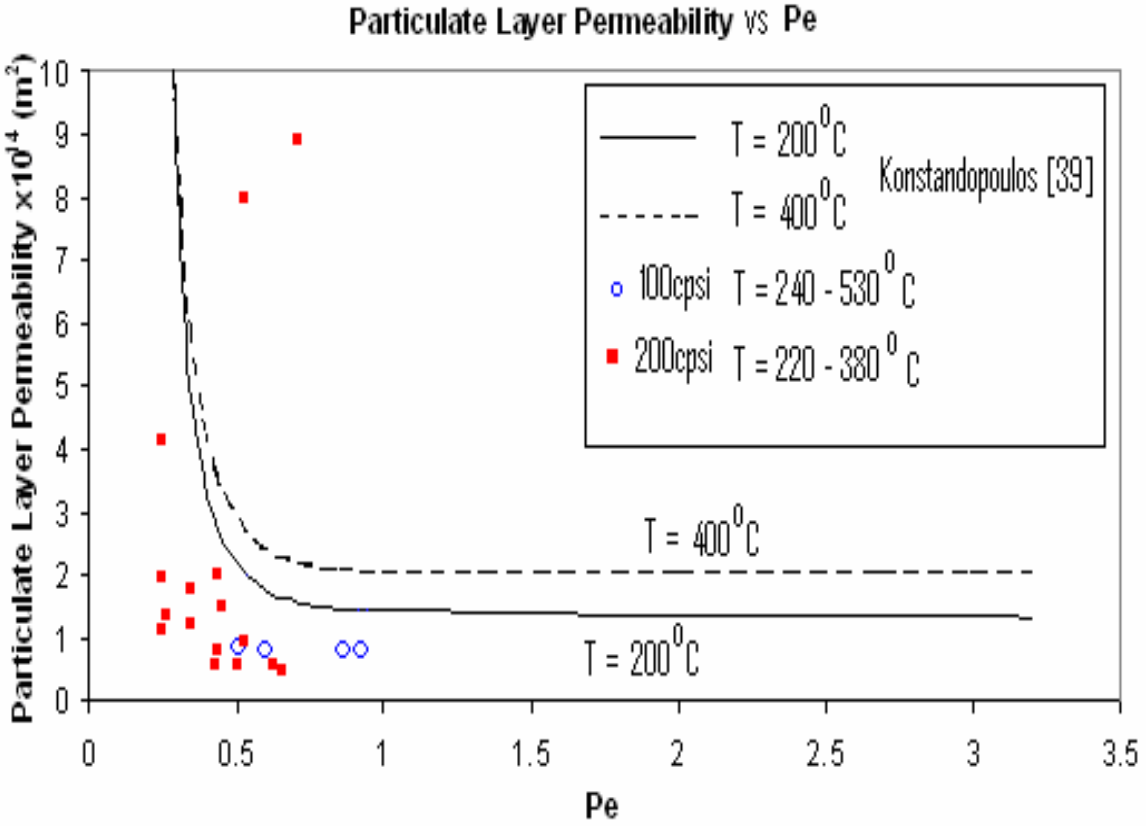

Figure 10 Particulate layer Permeability vs. Peclet Number

3.3.2 DOC-DPF System Modeling

Simulation results of the model calibration which was fitted to data from the DOC-DPF experimental work is presented in this section. The objective of this part of the experimental and numerical work was to determine the effect of the NO_2-assisted oxidation mechanism in the DPF.

Figure 11 shows the pressure drop profile across the 200cpsi DPF for the 2200 rpm 100% load condition with the DOC installed upstream of the DPF. As it can be observed in Figure 11 the pressure drop does not increase after the deep-bed filtration stage due to the effect of the NO_2-assisted oxidation of solid particulate mass becoming very significant in the cake layer and in the wall. The NO_2, generated from the conversion of NO inside the DOC, oxidizes the particulates deposited in and on the walls of the inlet channels. The pressure drop characteristics appear to have reached a constant value in which the pressure drop decreased due to both the particulate layer depletion and also due to the increase in filter wall permeability caused by the depletion of the solid particulate matter inside the porous wall. This later effect, appears to be more significant than the first one because considerable particulate mass (57g) was still measured at the end of this experiment, indicating the possibility that the particulate mass continues to accumulate as particulate layer on the filter walls, but at the same time the particulate oxidized inside the porous walls cause a significant increase in the wall permeability. Equation (1) shows the pressure drop across the porous walls. Particulate mass oxidized in the porous walls contribute to an increase in wall permeability and with this a decrease in pressure drop.

$$P_1 - P_2 = \frac{\mu(T_w)}{k_p} u_w w + \frac{\mu(T_w)}{k_s} u_w w_s \qquad (1)$$

To calibrate the model based on the experimental results observed in some of the operating conditions in which the pressure drop characteristics decrease at or below the point where the filter walls are completely filled, it was necessary to simulate this pressure drop decrease in the cake filtration region, with a sub-model representing the oxidation inside the porous wall as described in Hasan et al. [9,23]. By adding such sub-model, solid particulate mass oxidation in the wall affect the filtration model parameters, such as the filter wall permeability.

Figure 12 shows the prediction of the solid particulate mass being deposited, compared against the experimental results measured. Agreement within 7 grams of particulate was found in this particular case.

Even when the pressure drop across the DPF significantly decreases under constant regeneration due to NO_2, for the 2200 rpm 100% case, there is still significant solid particulate mass deposited inside the filter. Simulation results of the particulate layer evolution along the channel length show that due to some wall oxidation, the wall flow velocities at the front and end of the channel are larger than at the center of the filter, as usually observed during loading under low particulate oxidation conditions, therefore causing a larger deposition of solid particulate matter in the mid section of the inlet channels as it can be observed from Figures 13 and 14. Since the flow will find the path of less resistance, the wall flow velocities are higher at the front and end of the filter wall as can be observed in the velocity profiles in Figure 13. Wall flow velocities at the front and end of the inlet channels actually increase with time, as more particulate matter continues to be deposited in the center of the channels where the wall flow velocities are lower, and less mass is deposited on the sides as shown in Figure 14.

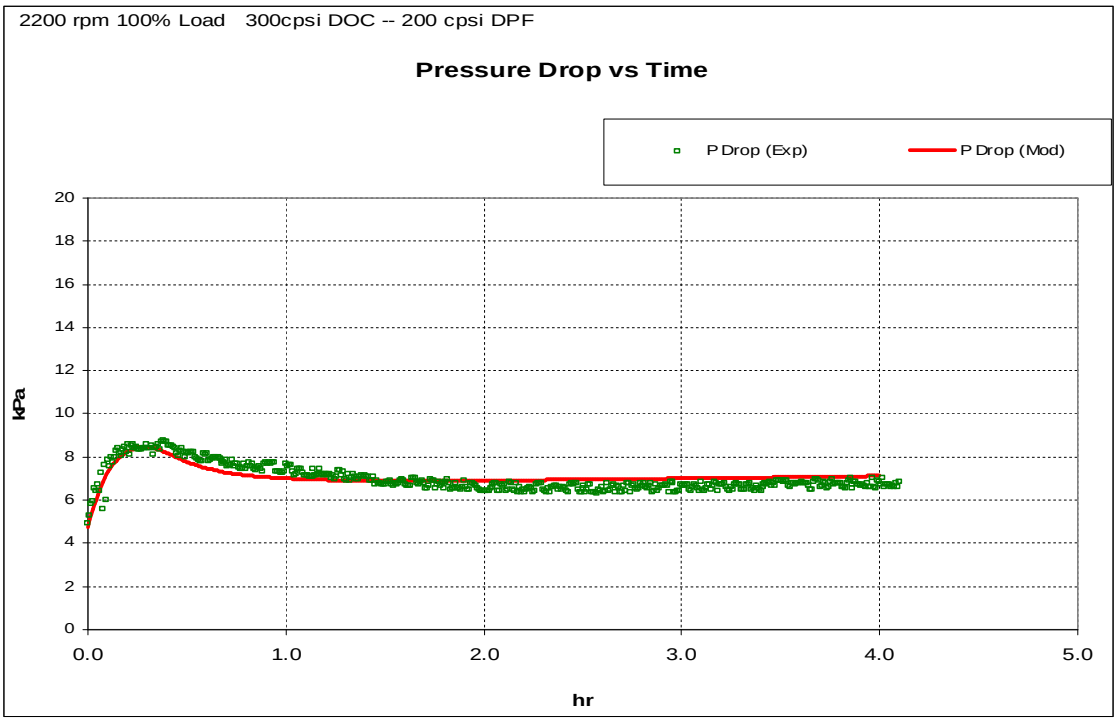

Figure 11 DOC-DPF Pressure drop across DPF at 2200 rpm 100% load for the 200cpsi filter. Model vs. Experimental.

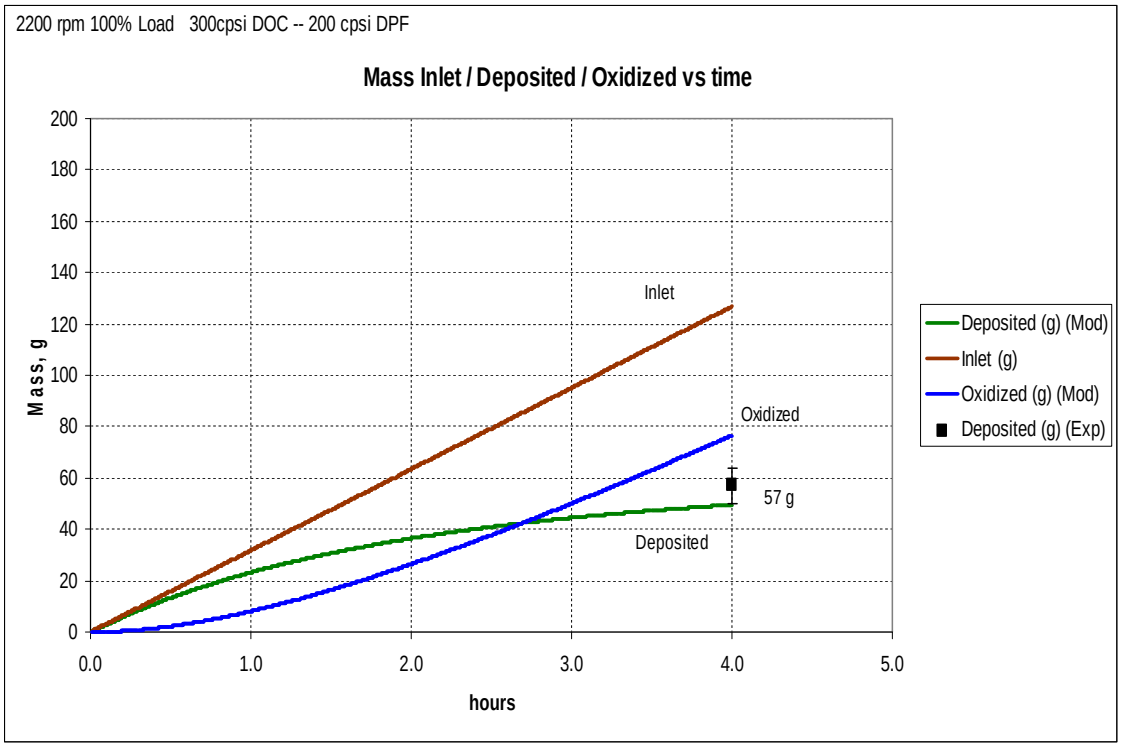

Figure 12 Mass deposited/oxidized in the DOC-DPF. 2200 rpm 100% load. 200cpsi filter. Model vs. Experimental

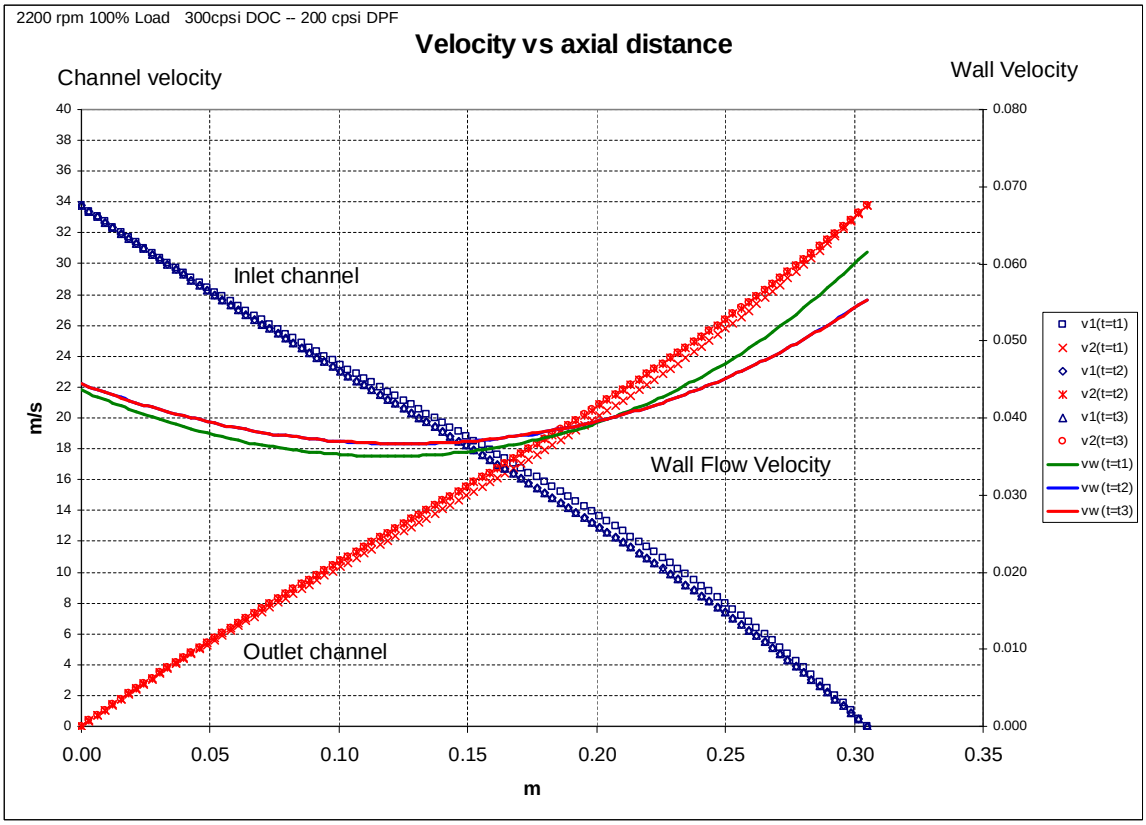

Figure 13 DOC-DPF Channel and wall flow gas velocities vs. axial length at 2200 rpm 100% load. 200cpsi filter. Model

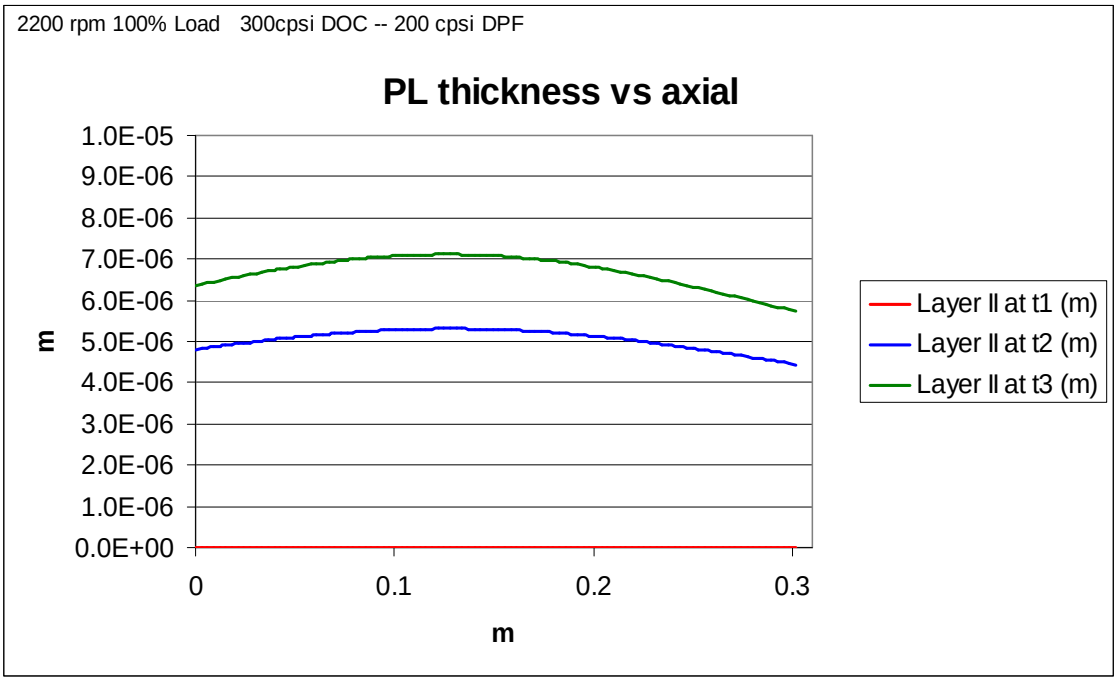

Figure 14 DOC-DPF Particulate layer thickness vs. channel axial length at 2200 rpm 100% load. 200cpsi filter. Model

The results of the remaining 7 conditions tested did not show similar trends as for the 2200 rpm 100% load condition. The reason for these results, was due to the lower NO_2 levels measured upstream of the DPF. Actually, only 4 of the 8 conditions of the DOC-DPF system show an apparent particulate oxidation by NO_2. The remaining 4, either the NO_2 was too low at high temperatures in which the NO and NO_2 reach equilibrium in the DOC, or the temperatures were too low to promote continuous regeneration.

Comparing the performance of the DPF with and without the effect of solid particulate mass oxidation by NO_2, resulted in significant pressure drop difference across the DPF during the loading experiment, as shown in Figure 15. Figure 15 shows the pressure drop vs. time characteristics of both the DPF and the DOC-DPF systems at the 2200 rpm 100% load condition, in which model and experimental results are compared. The effect of a higher NO_2/PM ratio (8.6) when using a DOC-DPF system instead a DPF alone (0.3) can be observed in Figure 15. In this case the DOC supplied 155 ppm of NO_2 to the DPF, compared against 10 ppm for the case without the aid of a DOC. Even when the NOx to PM ratios are similar, the NO_2/PM ratios clearly make the difference in the pressure drop characteristics of both systems under similar conditions.

Figure 16 shows similar results as in Figure 15, but for the 1400 rpm 100% load condition for both DPF and DOC-DPF systems. In this case, the amount of NO_2 in either condition is not significant (<10ppm), therefore the difference in pressure drop observed between the two loading experiments was mainly due to the difference in temperature (543^oC vs. 522^oC).

The cases discussed above were used to perform a parametric study to determine the effect of solid particulate matter concentrations, exhaust volumetric flow rates, gas temperatures, oxygen and NO_2 mole fractions on the regeneration behavior and the pressure drop characteristics across the DOC-DPF system. For this parametric study the

controlling parameters identified in the model calibration at 2200 rpm and 25,50,75 and 100% load cases were used, and only the PM and NO_2 concentrations were varied.

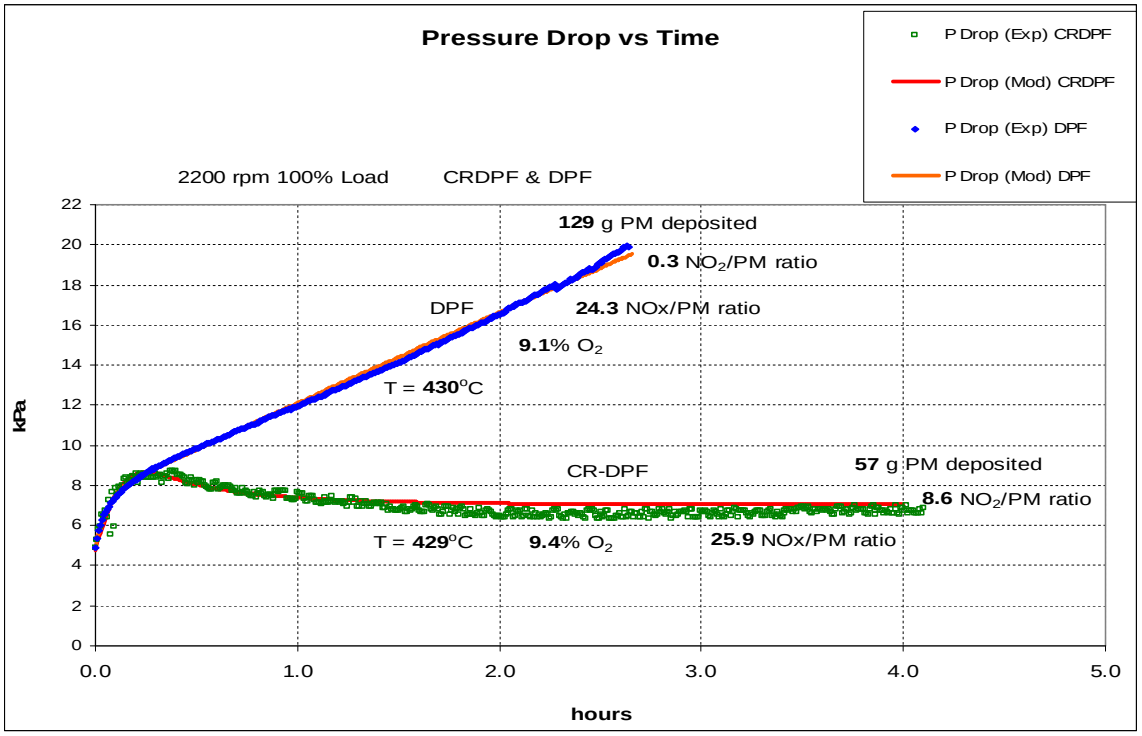

Figure 15 DPF pressure drop comparison between DPF and DOC-DPF operation at 2200 rpm 100% load. 300cpsi DOC and 200cpsi DPF.

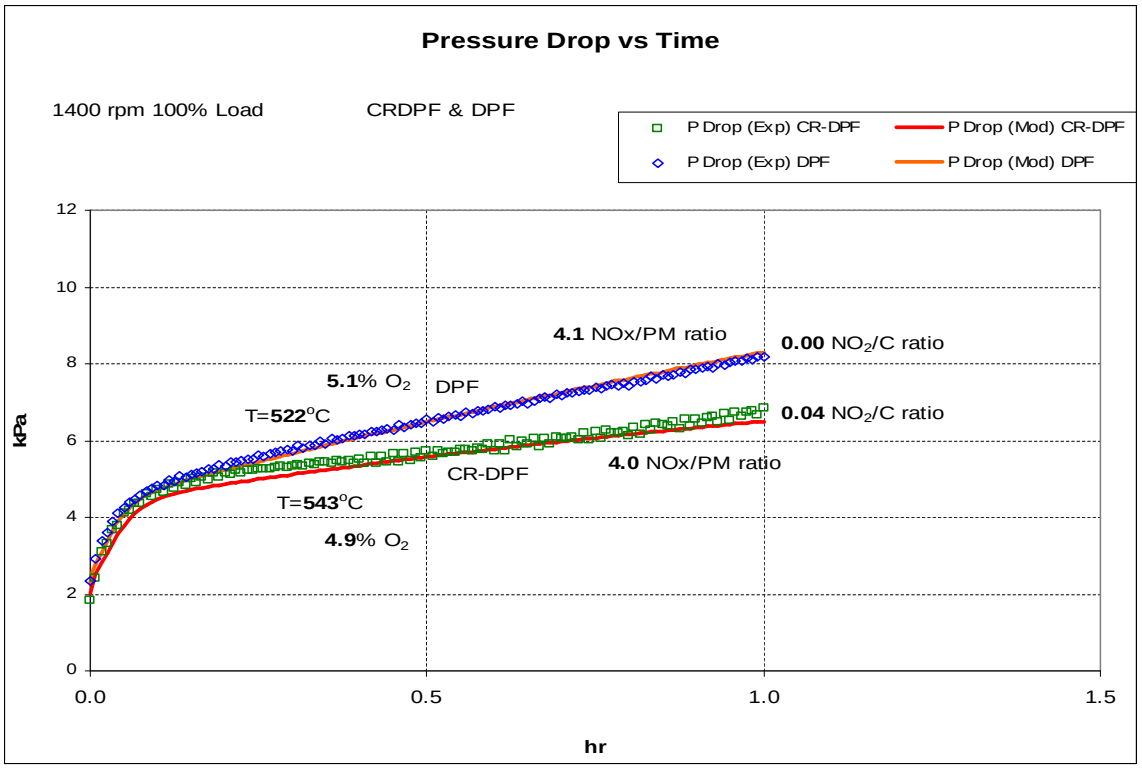

Figure 16 DPF pressure drop comparison between DPF and DOC-DPF operation at 2200 rpm 100% load. 300cpsi DOC and 200cpsi DPF.

3.3.3 DOC-DPF system Thermal and NO_2-assisted Regeneration Parametric Study

To study the effect on solid particulate matter and NO_2 mass flow rates, and NO_2/PM ratios in the regeneration performance of a DOC-DPF system, a parametric study was performed by using Design of Experiments tools. A 16-simulation-run test matrix was designed to evaluate the effect of engine exhaust solid PM emissions and NOx gaseous emissions at several loads and 2200 rpm. For this parametric study, four levels of each of the three factors (PM, NOx, and engine % load at 2200 rpm) were considered as shown in Table 1.

In each engine % load level, the actual DPF inlet exhaust gas conditions engine out measured during each loading experiment with 25,50,75 and 100% load at 2200 rpm 300cpsi DOC-200cpsi DPF case were used, except for the solid particulate matter concentrations, and NO_2 mole fractions as shown in Table 2. The NO_2 concentrations were obtained from the DOC model, and used as input for the DPF model. Each simulation run was for 4 hours.

This set of simulation runs provided a wide range of NO_2/PM ratio which is reported to be one of the most important parameters in a DOC-DPF system. Table 3 shows the Analysis of Variance (ANOVA) for a linear model analysis of the means vs. factors A, B, C.

Table 1 Input parameters and Simulation Design for Parametric Study

INPUT PARAMETERS

	NOx	**Solid PM**	**% Load**
Level	ppmv	mg/std m^3	2200 rpm
1	**100**	**10**	**25**
2	**200**	**20**	**50**
3	**300**	**30**	**75**
4	**400**	**40**	**100**

from Engine Exhaust		from DOC Model	
Engine Out / DOC in		DOC out / DPF in	
NO	NO2	NO	NO2
ppmv	ppmv	ppmv	ppmv
81	19	40	60
189	11	92	108
294	6	179	121
391	9	272	128

Simulation Design			
	Cin	% Load	yNO_2
Run No.	A	B	C
1	1	1	1
2	1	2	2
3	1	3	3
4	1	4	4
5	2	1	2
6	2	2	1
7	2	3	4
8	2	4	3
9	3	1	3
10	3	2	4
11	3	3	1
12	3	4	2
13	4	1	4
14	4	2	3
15	4	3	2
16	4	4	1

Table 2. Inlet conditions for each simulation run in parametric study

Factor	B			A			C					
Run No.	Load	Tin	Vdot	Cin	DPo	To	yNO2	yO2	yCO2	yH2O	Conc NO_2	NO_2/C
	%	^oC	act m^3/s	mg/act m^3	kPa	^oC	ppmv	% vol	% vol	% vol	mg/act m^3	by weight
1	25	286	0.275	5.3	1.3	114	60	13.57	4.4	5.8	37.86	7.1
2	50	362	0.399	4.7	2.6	175	108	11.37	5.8	7.1	60.00	12.8
3	75	403	0.55	4.4	3.4	248	121	10.47	6.3	7.7	62.80	14.2
4	100	429	0.649	4.2	4.9	326	128	9.42	7	8.4	64.20	15.1
5	25	286	0.275	10.7	1.3	114	108	13.57	4.4	5.8	67.98	6.4
6	50	362	0.399	9.4	2.6	175	60	11.37	5.8	7.1	33.25	3.5
7	75	403	0.55	8.8	3.4	248	128	10.47	6.3	7.7	66.63	7.6
8	100	429	0.649	8.5	4.9	326	121	9.42	7	8.4	60.65	7.1
9	25	286	0.275	16.0	1.3	114	121	13.57	4.4	5.8	76.16	4.8
10	50	362	0.399	14.1	2.6	175	128	11.37	5.8	7.1	70.93	5.0
11	75	403	0.55	13.2	3.4	248	60	10.47	6.3	7.7	31.23	2.4
12	100	429	0.649	12.7	4.9	326	108	9.42	7	8.4	54.13	4.3
13	25	286	0.275	21.3	1.3	114	128	13.57	4.4	5.8	80.57	3.8
14	50	362	0.399	18.8	2.6	175	121	11.37	5.8	7.1	67.05	3.6
15	75	403	0.55	17.6	3.4	248	108	10.47	6.3	7.7	56.22	3.2
16	100	429	0.649	17.0	4.9	326	60	9.42	7	8.4	30.07	1.8

Table 3. Analysis of Variance of the Means

ANOVA						
Source	DF	Seq SS	Adj SS	Adj MS	F	P-value
A = Cin	3	0.0118	0.0118	0.0039	2.59	0.15
B = % Load (Temperature, Vol. Flow Rate)	3	0.4577	0.4577	0.1526	100.85	0.00
C = NO2	3	0.0341	0.0341	0.0114	7.51	0.02
Residual Error	6	0.0091	0.0091	0.0015		alfa = 0.05
Total	15	0.5126				

The effect of engine load at 2200 rpm (i.e. exhaust gas temperature, actual volumetric flow rate, etc) has a very statistically significant effect on the ratio of solid PM mass oxidized by NO_2 to the solid PM mass entering the DPF. NO_2 concentrations had the second largest statistical significance, and solid particulate matter concentrations had no statistically significant effect. Even though the effect on the solid particulate matter concentration is not statistically significant for amount of solid particulate mass oxidized, it does have a very significant effect on the amount of mass deposited in the filter, and also in the pressure drop across the DPF, particularly at temperatures 362^{o}C and below. Figure 17 shows the effect of solid particulate matter concentration on the pressure drop across the DPF. It can be observed that as temperature increases from 286^{o}C to 403^{o}C the effect of the solid particulate concentration becomes less and less significant, as oxidation by NO_2 becomes more significant. The reason why the pressure drop at 403^{o}C (75% load) with 40 mg/std m^3 of solid PM was slightly lower than the 30 mg /std m^3 is due to the fact that the NO_2/PM ratio was higher (3.2) for the 40mg/std m^3 case than for the 30mg/ std m^3 (2.4). This result is evidence that the NO_2/PM ratio becomes very important as exhaust gas temperature increase from 362 to 403^{o}C.

Figure 18 shows the effect of NO_2 concentrations on DPF pressure drop. It can be observed from Figure 17 and 21 at 286°C that the effect of NO_2/ PM ratio increasing from 3.8 to 7.1 is inversely proportional to the pressure drop across the DPF. The higher the NO_2/PM ratio, the lower the DPF pressure drop. This effect is overlapped with the fact that the lightest loading (10 mg/std m^3) had also the lowest NO_2 concentration (60ppm). At 362°C, the combined effect of temperature and NO_2/PM ratio becomes more evident. The crossing of the 128ppm under the 121ppm line and the 108ppm under the 60ppm is due to higher NO_2/PM ratios at those conditions as can be observed from Table 2. At 403°C the exhaust gas temperature is the dominant factor in the NO_2-assisted oxidation process, as a change in the NO_2/PM ratio from 2.4 to 14.2 is practically undetectable in the pressured drop characteristics across the DPF.

Figure 19 illustrates the effect of solid PM concentration on NO_2-assisted and thermal oxidation of PM vs. exhaust gas temperature. For these simulation results, a constant NO_2 concentration of 120ppm was selected for all 16 runs at each of the 4 temperatures studied (286,362,403, and 429°C).

To determine the amount of solid PM mass oxidized thermally and that by NO_2, the O_2 and NO_2 depletion rates from equations 6 and 10 were used to quantify the respective concentrations that have been consumed due to oxidation of solid PM. Figure 20 shows a comparison between the solid PM mass thermally oxidized and that oxidized by NO_2. As the NO_2 increases from 60 to 128ppm, so does the mass oxidized increase from zero to approximately more than 50% of the solid PM mass entering the DPF. The effect of temperature can also be observed, as the amount of mass oxidized increases at higher temperatures (from 286 to 429°C).

Figure 21 shows the effect of NO_2/PM ratio on the ratio of mass oxidized to mass entering the DPF at the different temperatures studied (286, 362, 403, and 429°C). At 286°C, very low solid PM oxidation due to NO_2 was detected. It can be observed that as temperature increases from 362 to 429°C, the solid PM oxidation increases with an NO_2/PM ratio increase, but is limited and not much is gained by increasing the ratio after a value of 8.0. The reason for this is probably due to the effect of the NO_2 concentration being more important to the solid PM oxidation than the NO_2/PM ratio.

Figure 22, shows the effect of exhaust gas temperature, the effect of NO_2 concentration and PM solid concentrations in the amount of solid PM mass oxidized. As it can be observed from the four curves in the plot, two curves represent the constant PM concentration and variable NO_2, and two curves the constant NO_2 and variable PM concentration at two temperatures 382 and 416°C. The effect of higher NO_2 is much more significant to the solid PM oxidation than the actual NO_2/PM ratio.

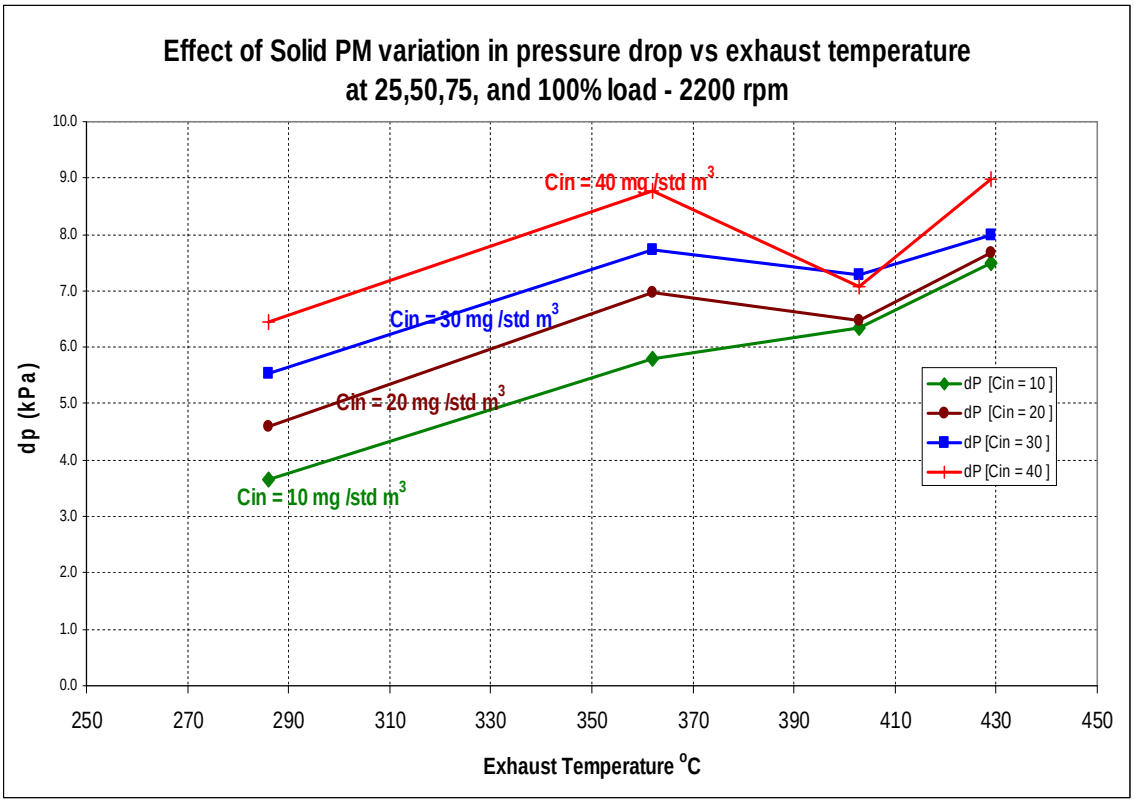

Figure 17. Effect of PM variation in pressure drop after 4 hours

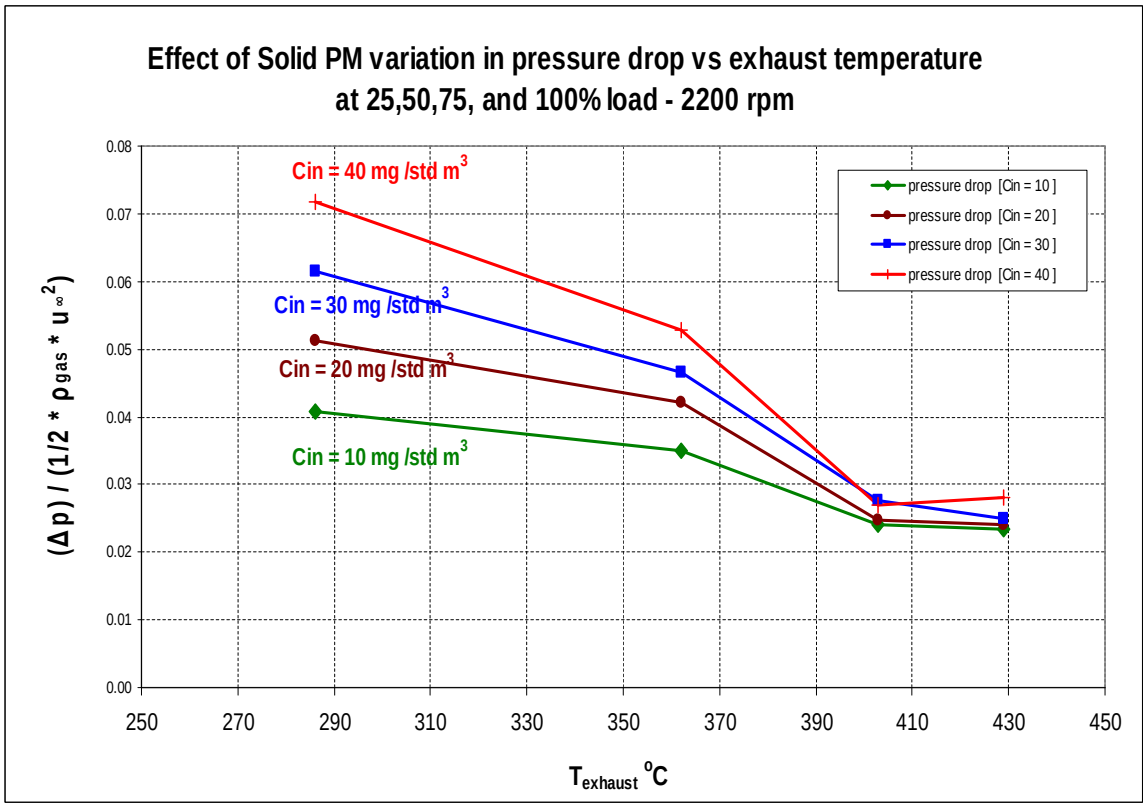

Figure 18. Effect of NO_2 concentration in pressure drop after 4 hours

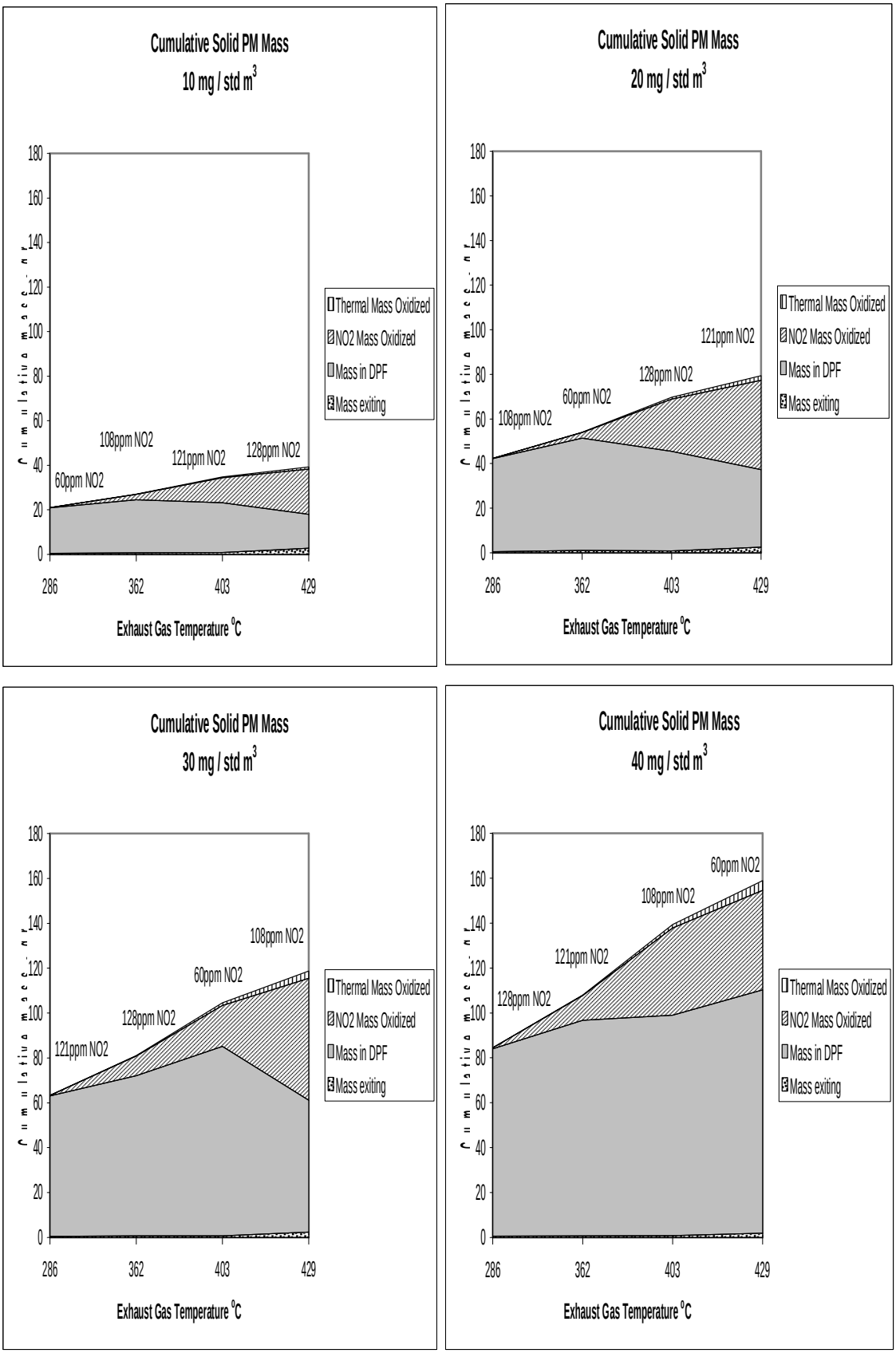

Figure 19. Cumulative solid PM mass after 4 hours at four different inlet solid PM concentrations.

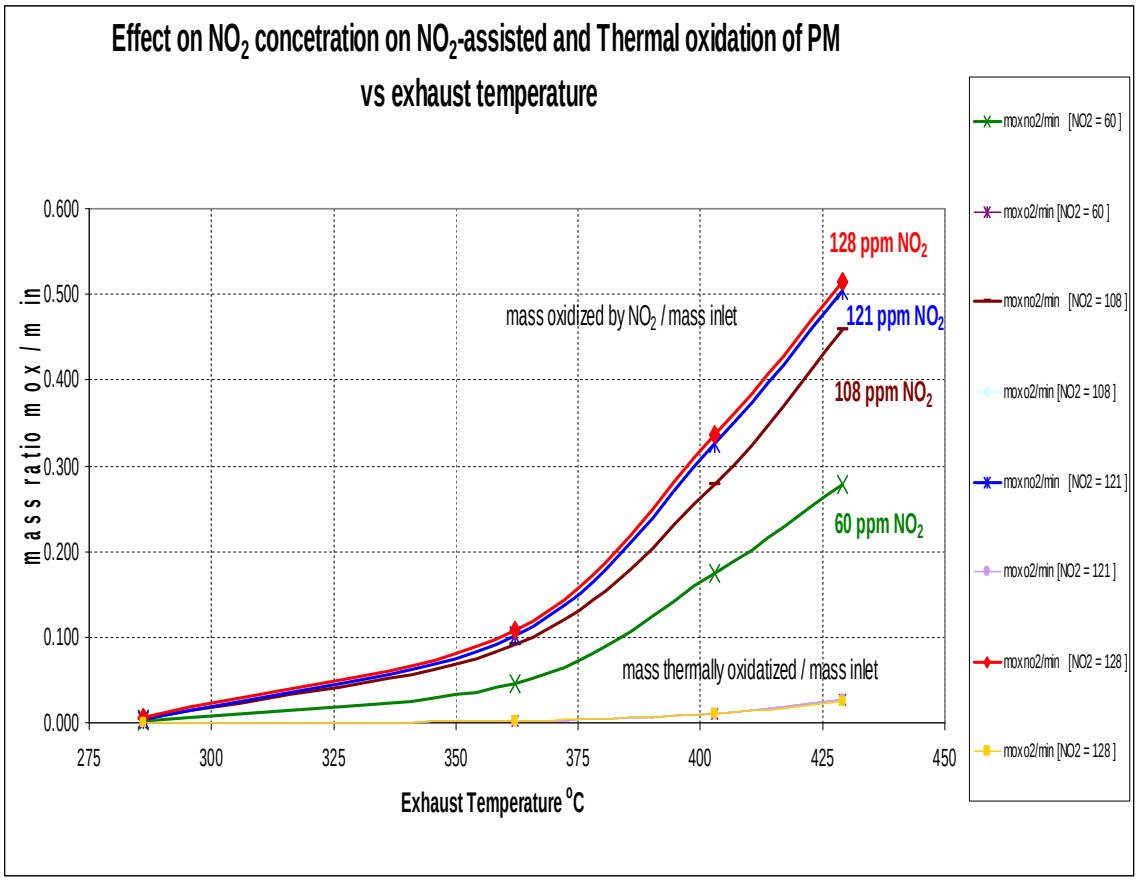

Figure 20. Solid PM Mass oxidized by NO_2 and by O_2 after 4 hours.

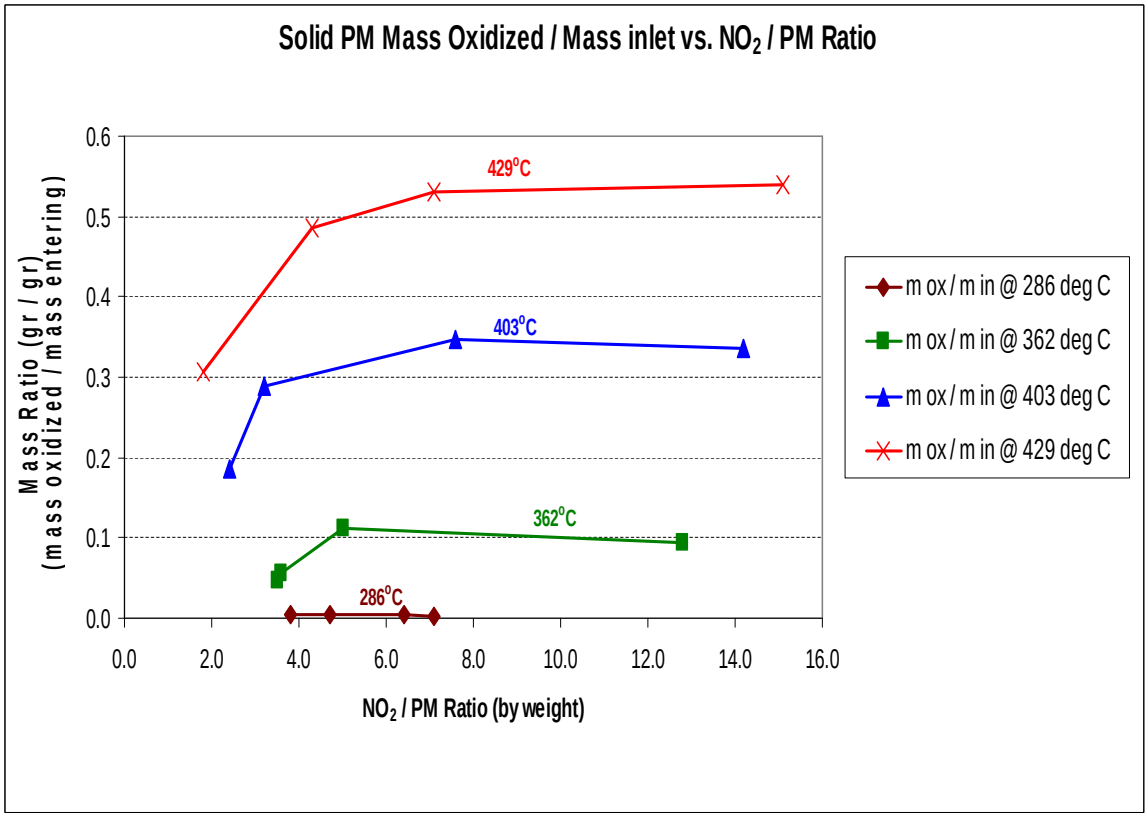

Figure 21 Ratio of mass of PM oxidized by mass of PM entering vs. NO_2 / PM ratio after 4 hours.

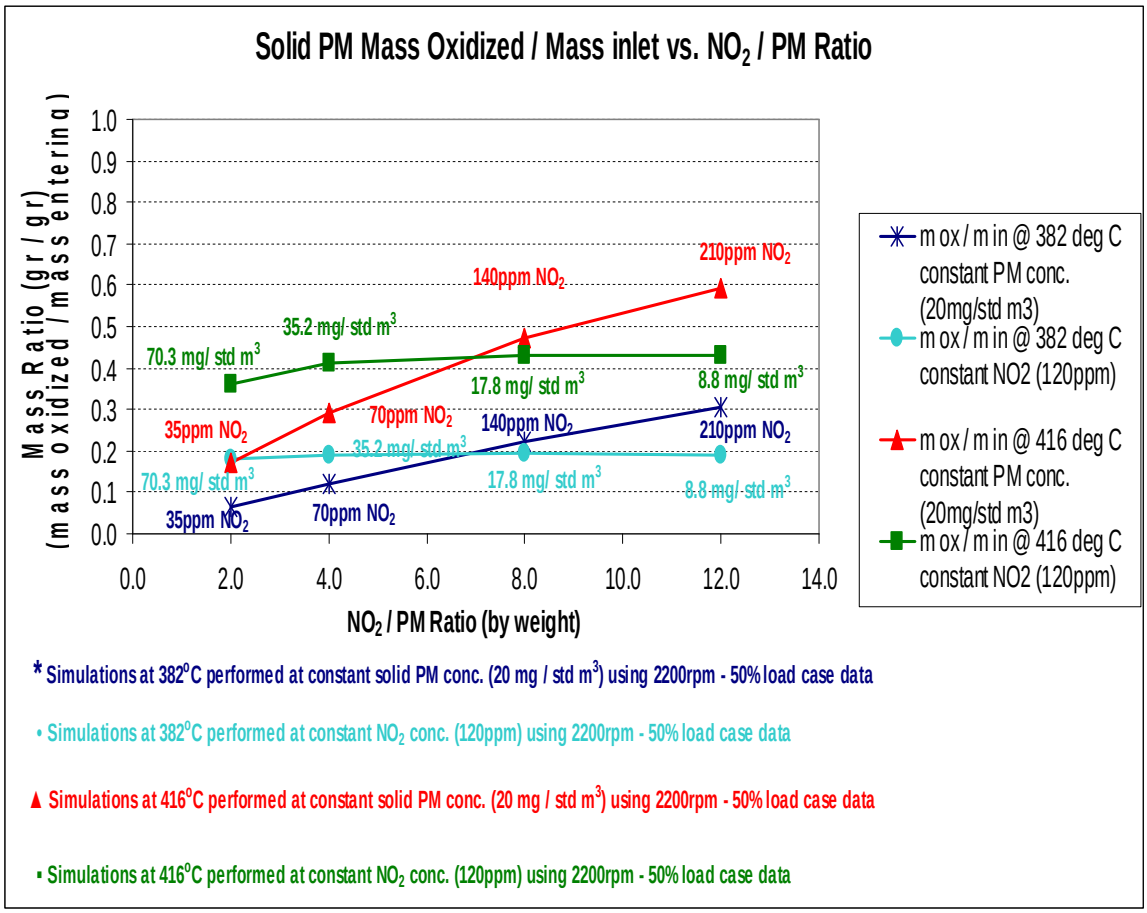

Figure 22 Ratio of mass of PM oxidized by mass of PM entering vs. NO_2 / PM ratio.

In addition to the parametric study presented, some extra simulation cases were run to quantify the amount of PM mass oxidized for both the NO_2-assisted and the thermal oxidation mechanisms using the same measured engine conditions in the experimental work but with lower or higher exhaust gas temperatures, and lower or higher NO_2 concentrations. Using the 1400 rpm 100% load case baseline conditions, the inlet gas temperature was varied from 200 to 700°C. The amount of PM mass oxidized varied from 0.0% at the low temperatures (<400°C) to 95.0% at 700°C as it can be observed on Figure 23. For the 2200 rpm 100% load case the NO_2 concentration was varied from 0ppm to 300ppm. As can be observed in Figure 24, the amount of PM mass oxidized increased from 2.7% with 0ppm NO_2 to 76.1% with 300ppm. The 2.7% of PM mass oxidized was due to thermal oxidation, as expected from the results shown in Figure 23.

Since NO_2 as high as 300ppm at 430°C oxidize up to 76% of the solid PM entering (125g /4 hours), and considering the significant pressure drop decrease in the filter (<8kPa), it is suggested that the NO_2-assisted oxidation may have local regeneration effects possibly leading to an heterogeneous solid PM distribution in the DPF. This affirmation cannot be demonstrated in this research work, but Ranalli et al. [17] show how to measure and simulate the solid PM distribution inside the DPF. Maly et al. [18] show the effect of NO_2-assisted oxidation on the solid PM distribution, in which they concluded that the DOC-CPF had better NO_2-assisted oxidation performance than the CPF and the DOC-DPF, which was the poorest in performance.

Allanson et al. [19] compared the performance of a DOC-DPF system against a CPF and a DOC-CPF. In their experimental work, balance point temperature of around 265°C was determined for the DOC-DPF system, 280°C for the CPF only, and 250°C for the DOC-CPF system. In the present research, only two test conditions (2200 rpm 100% load, and 1400 rpm 25% load) had NOx/PM ratios higher than 25. The 1400 rpm 25% load had exhaust gas temperatures (249°C), below the balance point temperature of 265°C given by Allanson et al. [19] so only one case (2200 rpm 100% load) successfully demonstrated the efficient DPF regeneration performance of the DOC-DPF system. During the present experimental work, at temperatures close to the balance point temperature (286°C at 2200 rpm 25% load) the NOx/PM ratio was low (<6) limiting the operation of the DOC-DPF system under this particular engine speed and load condition. The DECSE 2000a [20,21] reported CRT™ Balance Point Temperature (BPT) data as a function of fuel sulfur level, and at less than 15ppm S, the BPT varied from approximately 275 to 310°C depending on the engine speed studied, where higher engine speeds had the higher balance temperatures. The parametric study discussed in this paper showed practically no activity of the NO_2 reacting with the solid PM at 286°C as was shown in Figure 23. From the present research work, it cannot be concluded how the performance of the DOC-DPF system may had been at temperatures around 286°C, since not enough data were obtained from the experimental effort. This may have affected the accurate determination of the kinetic parameters in the DPF model at those low temperatures.

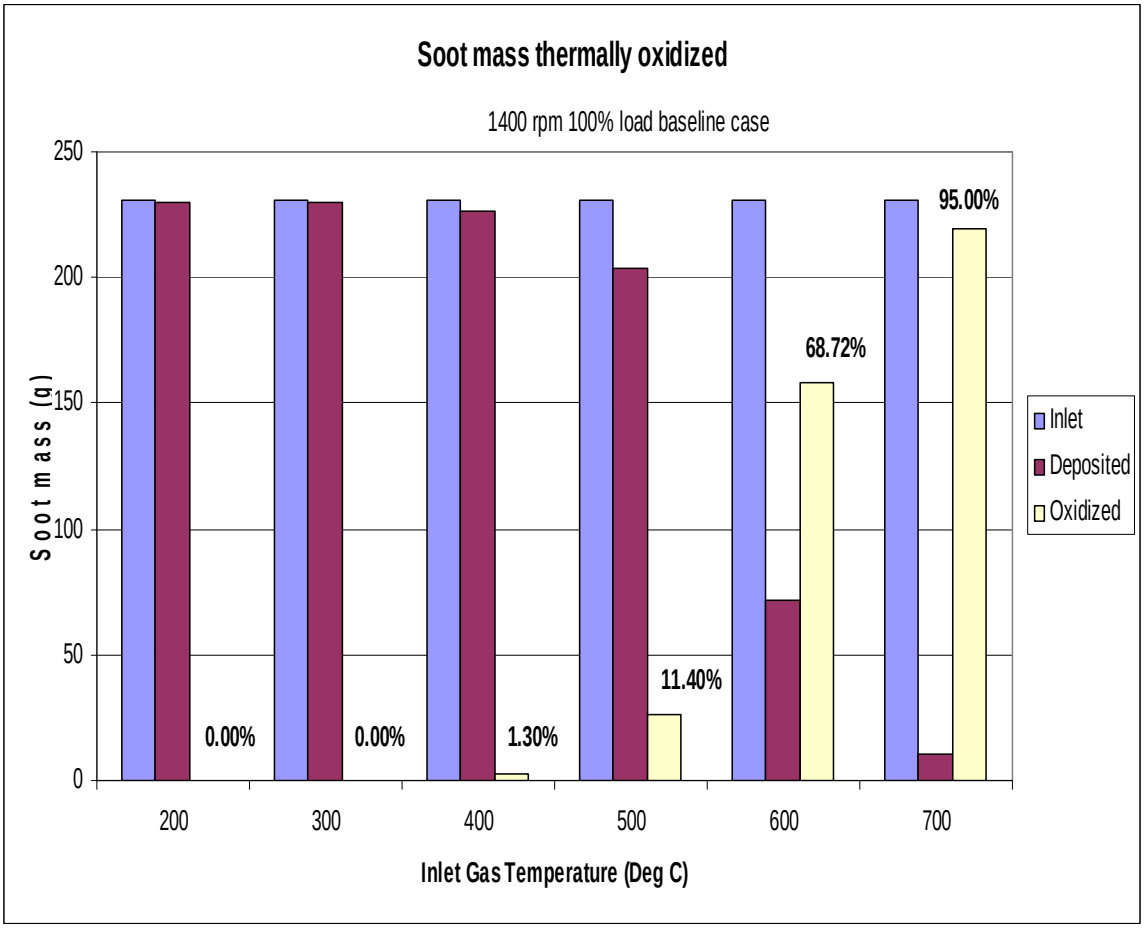

Figure 23. Effect Thermal Regeneration comparison from 200 to 700 deg C at 4 hours

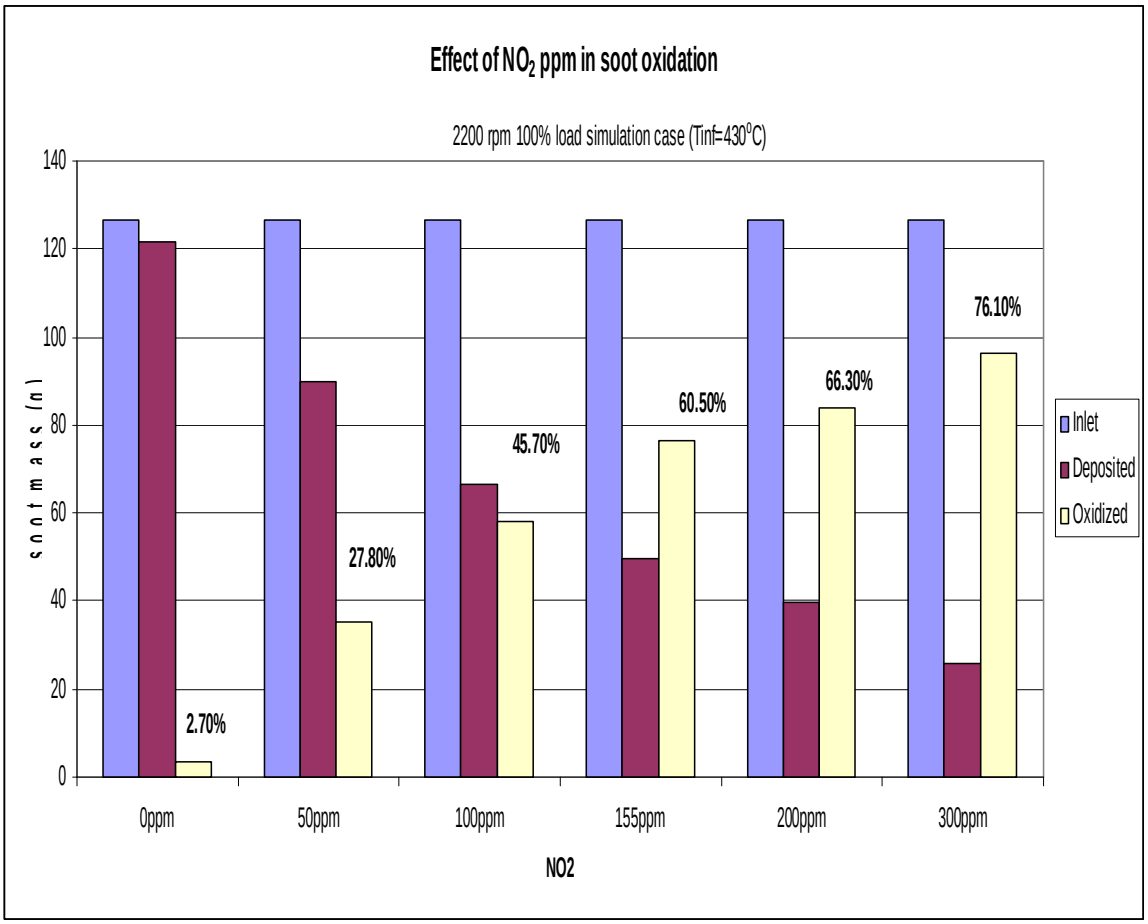

Figure 24. Effect of NO_2-assisted Regeneration comparison at 0, 50, 100, 155, 200, and 300ppm at 4 hours.

3.4 SUMMARY & CONCLUSIONS IN TASK I

Model predictions of the solid particulate mass deposited in the DPF after each loading and regeneration experiment were in agreement within +/- 10g (or +/-10%) of experimental measurements at most of the engine operating conditions (14 out of 20 experiments). Discrepancies (20-40%) found in 6 experiments were attributed to measurements in solid particulate matter concentrations in those particular cases. The effect of these measurement errors on the estimated DPF model controlling parameters was on the particulate layer permeability which apparently was being underestimated. The corrected particulate layer permeability showed better agreement with values reported in the literature [2,3,5,7,12,13,14] and with the remaining 14 cases studied in this research work. The estimated thermal and NO_2-assisted activation energies obtained from the model calibration were: 150 and 122 kJ/mol respectively. These values are in agreement with values reported in the literature [2,3,5,7,12,13,14]. The values of the pre-exponential factors were 0.4 for the thermal oxidation and 100 for the NO_2 assisted oxidation. These values gave pressure drop and solid particulate mass predictions within 10% of experimental results throughout the entire range of conditions evaluated. DPF clean pressure drop was calibrated within +/- 0.1 kPa of the experimental values measured. The average clean filter permeability was 2.372×10^{-13} m^2 with a 2 standard deviation of 1.007×10^{-13} m^2. These values are in the range of permeability values reported in references [2,7] for the same type of filters. The variation in the permeability values

was attributed to the procedures employed in the determination of the initial or "clean" condition during the filter loading experiments.

Model predictions of the pressure drop across the DPF for all loading conditions were in good agreement (correlation coefficient $R^2 > 0.99$) with the experimental data during the loading phase where the recommended filter loading was not exceeded. Estimates of the solid particulate mass packing density inside the porous wall were between 1-5 kg/m^3; and percolation factors were between 0.81 and 0.97. Solid particulate layer packing density values were between 11 and 128 kg/m^3. The large range of packing density values was due to the range of Peclet Numbers encountered (0.25 to 0.85), particularly at low Peclet numbers, diffusive transport of particles becomes more dominant and with this the structure of the particles accumulation on the layer is more porous. These values were in agreement with the Peclet number correlation theory from Konstandopoulos et al. [22]. Average particulate layer permeability was 1.95x10-14 m^2 and all estimated values varied within the same order of magnitude of those reported in the literature [2,3,7].

NO_2-assisted oxidation of PM in the DPF showed experimentally that a significant reduction of the pressure drop (<8kPa) can be achieved when sufficient NO_2 (>120ppm) is available and high exhaust gas temperatures (~400^{o}C) can be maintained. The benefit of solid PM oxidation by NO_2 was limited to certain engine operating conditions (363^{o}C to 500^{o}C). At high temperatures (>500^{o}C) the DOC-DPF system was not efficient to reduce pressure drop across the DPF, due to very low NO_2 concentrations from the DOC (<10ppm). At low temperatures (<363^{o}C), NO_2/PM ratio by weight were lower than 2.0, and even when considerable NO_2 was present (>86ppm), the system still had a poor regeneration behavior. Only at one condition (2200rpm 100% load) was NO_2/PM greater than 8.0, providing high regeneration rates. The CRT^{TM} (DOC-DPF system) showed limited advantages when used in combination with an EGR strategy for a continuous operation of an engine-exhaust aftertreatment system. As EGR increases, NOx decreases, and PM increases, limiting the amount of NO_2 produced in the DOC, and reducing the NO_2/C ratio that can be used in the DPF to oxidize the PM.

The DOC model [15] predicted the conversion of NO to NO_2 within +/-5% of the experimentally measured conversion efficiencies in a parametric study. The predicted NO_2 were used as input in the DPF model to estimate the oxidation of solid particulate mass in the filter. Temperature is the most important factor in both, thermal and NO_2-assisted oxidation processes. Higher temperatures require less NO_2 to be used and lower NO_2/PM ratios. NO_2 is much more effective than O_2 in PM oxidation in a DPF, but possibly leads to a less uniform distribution of the solid PM in the filter than the thermal oxidation. NO_2 flow rates are more important than NO_2/PM ratios. Larger ratios of solid PM mass oxidized per solid PM mass entering the DPF for the same NO_2/PM ratio were obtained when higher NO_2 flow rates were used. The amount of solid PM thermally oxidized decreased as the NO_2 increased at the same temperature condition.

4. TASK II

4.1 Model Development

This section gives an overview of the computer models developed and used as part of this study, as well as relevant governing equations for both models. A comprehensive description of the two models is given in reference [25]. Reference [23] describes in detail the CPF model.

4.1.1 DOC 1-D MODEL

The MTU 1-D DOC model was developed as part of this research [25] and is based on similar models available in references [15, 26, 27, and 28]. This model uses a one-dimensional single channel representation of the DOC, as shown in Figure 25. The exhaust gas mixture flows through the DOC in a 2-phase flow (gas-phase and solid-phase), and all gaseous species reactions are considered to be occurring in the solid-phase, and at the local substrate wall temperature. Details about the governing conservation equations used in the DOC model are given in reference [25]. Heat transfer between the gas in the channel and the substrate wall takes place through convection, and heat loss from the substrate wall to the ambient is also considered in the model via a convection mechanism. Physical properties of the exhaust gas mixture calculated in this model are based on simplified equations as given in reference [29].

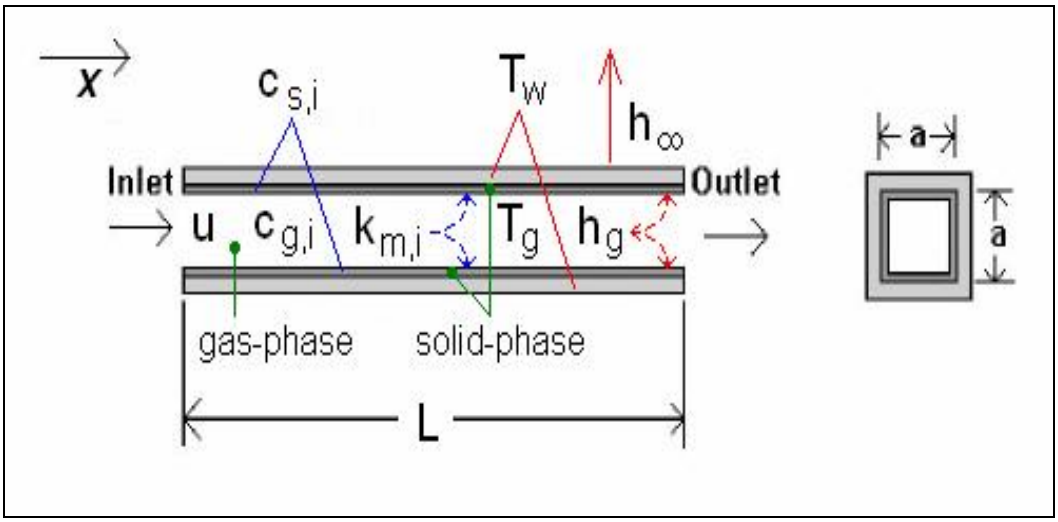

Figure 25: Schematic representation of the single channel DOC (adapted from [15])

CHEMICAL REACTIONS AND KINETICS

The kinetics scheme considered in the model uses equations of the Langmuir-Hinshelwood form (Reference [27]) for expressing the rates of chemical reactions. There are 8 global one-step reactions available in the DOC model. They are:

1. Oxidation of *CO* (solid-phase)

$$CO + \frac{1}{2} O_2 \rightarrow CO_2 \qquad (12)$$

2. Oxidation of *NO* (solid-phase)

$$NO + \frac{1}{2}O_2 \rightarrow NO_2 \tag{13}$$

3. Oxidation of C_3H_6 (solid-phase)

$$C_3H_6 + \frac{9}{2}O_2 \rightarrow 3CO_2 + 3H_2O \tag{14}$$

4. Oxidation of CH_4 (solid-phase)

$$CH_4 + 2O_2 \rightarrow CO_2 + 2H_2O \tag{15}$$

5. Oxidation of $C_{16}H_{34}$ (solid-phase)

$$C_{16}H_{34} + \frac{49}{2}O_2 \rightarrow 16CO_2 + 17H_2O \tag{16}$$

6. NO_2-assisted *PM* oxidation (gas-phase)

$$\begin{aligned} &C + (2 - g_{CO})NO_2 \rightarrow \\ &g_{CO}CO + (1 - g_{CO})CO_2 + (2 - g_{CO})NO \end{aligned} \tag{17}$$

7. Thermal *PM* oxidation (gas-phase)

$$\begin{aligned} &C + \left(1 - \frac{f_{CO}^{thermal}}{2}\right)O_2 \rightarrow \\ &f_{CO}^{thermal}CO + \left(1 - f_{CO}^{thermal}\right)CO_2 \end{aligned} \tag{18}$$

8. Catalytic *PM* oxidation (gas-phase)

$$\begin{aligned} &C + \left(1 - \frac{f_{co}^{catalytic}}{2}\right)O_2 \rightarrow \\ &f_{CO}^{catalytic}CO + \left(1 - f_{CO}^{catalytic}\right)CO_2 \end{aligned} \tag{19}$$

In this study, however, all hydrocarbons were considered to be represented by equimolar concentrations of propylene (C_3H_6) and hence, Reactions (15) and (16) were not considered, and Reactions (17) thru (19) were also assumed not to be taking place since *PM* oxidation in flow-through situations at exhaust temperatures less than 500°C can be considered negligible compared to that in wall-flow situations such as in the CPF.

Rate expressions for the reactions (12) thru (14) were described using Langmuir-Hinshelwood expressions as follows:

$$R_{CO} = \frac{A_1 e^{\frac{-Ea_1}{RT}} Y_{s,CO} Y_{s,O_2}}{G_1} \tag{20}$$

$$R_{NO} = \frac{A_2 e^{\frac{-Ea_2}{RT}} Y_{s,NO} Y_{s,O_2}}{G_2} \tag{21}$$

$$R_{C_3H_6} = \frac{A_3 e^{\frac{-Ea_3}{RT}} Y_{s,C_3H_6} Y_{s,O_2}}{G_3 G_4} \tag{22}$$

where G_1 thru G_4 are the inhibition terms [27] accounting for the reduction in reaction rates of each species due to solid-phase concentrations of other species and are given by:

$$\begin{aligned} &G_1 = T_w\left(1 + A_{a,1}Y_{s,CO} + A_{a,2}Y_{s,C_3H_6}\right)^2 \times \\ &\left(1 + A_{a,3}Y_{s,CO}^2 Y_{s,C_3H_6}^2\right)\left(1 + A_{a,4}Y_{s,NO}^{0.7}\right) \end{aligned} \tag{23}$$

$$G_2 = T_w \left(1 + A_{a,5} Y_{s,CO} + A_{a,6} Y_{s,C_3H_6}\right)^2 \times \left(1 + A_{a,7} Y_{s,CO}^2 Y_{s,C_3H_6}^2\right)\left(1 + A_{a,8} Y_{s,NO}^{0.7}\right) \quad (24)$$

$$G_3 = T_w \left(1 + A_{a,9} Y_{s,CO} + A_{a,10} Y_{s,C_3H_6}\right)^2 \times \left(1 + A_{a,11} Y_{s,CO}^2 Y_{s,C_3H_6}^2\right)\left(1 + A_{a,12} Y_{s,NO}^{0.7}\right) \quad (25)$$

$$G_4 = \left(1 + A_{a,13} Y_{s,O_2}\right)^{1.5} \quad (26)$$

The values of adsorption equilibrium constants ($A_{a,1}$ thru $A_{a,13}$) used in Equations (23) thru (26) are calculated from Arrhenius-type relations as follows:

$$A_{a,j} = A_{a0,j} e^{\frac{-\Delta H_j}{RT_w}} \quad (27)$$

where the values of adsorption factors ($A_{a0,j}$) and adsorption heats $\left(\Delta H_j\right)$ used in the DOC model are shown in Table 4, as obtained from reference [27][1].

Table 4: Values of adsorption parameters [27]

Constant	**Adsorption Factor ($A_{a0,j}$)**	**Adsorption Heat (ΔH_j)**
	(.)	***(J/mol)***
$A_{a,1}$	65.5*	-7990
$A_{a,2}$	2080	-3000
$A_{a,3}$	3.98	-96534
$A_{a,4}$	479000	31036
$A_{a,5}$	0*	0*
$A_{a,6}$	0*	0*
$A_{a,7}$	3.98*	-96534*
$A_{a,8}$	700000*	31036*
$A_{a,9}$	65.5*	-7990
$A_{a,10}$	2080	-3000
$A_{a,11}$	3.98	-96534
$A_{a,12}$	400000*	31036
$A_{a,13}$	90000*	0

[1] Values marked by asterisks in Table as reported in reference [9] were changed to current values according to private communication with the author.

4.1.2 DPF 1-D MODEL

The detailed description of the MTU 1-D 2-layer CPF model developed as part of previous research at MTU is given in references [9] and [23], and is based on the regeneration framework presented in reference [5], and the filtration process is based on the model presented in references [6] and [7]. Figure 26 shows the representation of the CPF, which uses a single inlet channel, a substrate wall and a single outlet channel, with cross-sectional average values of velocity and exhaust temperature as input to represent all the CPF channels.

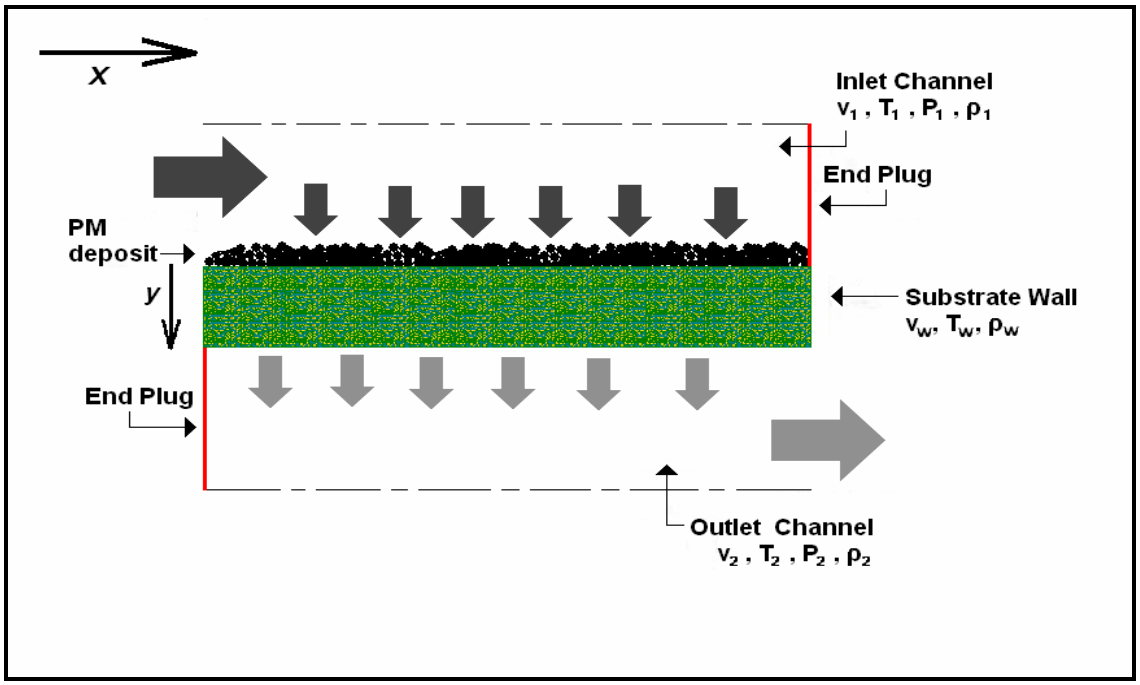

Figure 26: Schematic of single channel representation used in CPF model

FILTRATION

The filtration process in the CPF is represented by filtration by two porous filters in series, the *PM* cake layer and the substrate wall. When the CPF is 'clean', the substrate wall is the only filter present. When the porous substrate wall fills with *PM*, a 'cake' of *PM* builds on the substrate wall, and consequently, this *PM* cake layer becomes the first filter in series (with the substrate wall acting as the second filter in series). In other words, the filtration efficiency of the first filter is zero at initiation, and gradually builds up to a high value (> 95%) as the thickness of the *PM* cake layer increases. On the other hand, the filtration efficiency of the second filter (i.e., the clean substrate wall) is non-zero (60-80% from calibrated CPF model results shown later) at initiation of loading. The filtration efficiency of the clean substrate wall is a function of the volumetric flow rate of the exhaust and the substrate properties such as the clean porosity and clean permeability, and the cumulative loading of *PM* in the substrate wall determines the filtration efficiency of the 'loaded' wall. Figure 27 shows the "two filters in series" approach taken to represent the *PM* cake and substrate wall. Details about the equations used to calculate filtration efficiencies of the *PM* cake and substrate wall filters can be found in references [23 and 25].

OXIDATION

Oxidation of *PM* deposited in the CPF takes place through two mechanisms – NO_2/temperature-assisted and thermal. The NO_2/temperature-assisted mechanism for *PM* oxidation occurs due to the inlet NO_2 as well as NO_2 produced as the exhaust gas mixture passes through the substrate wall. A description of the oxidation sub-model used in the CPF model is given in references [9,23,25].

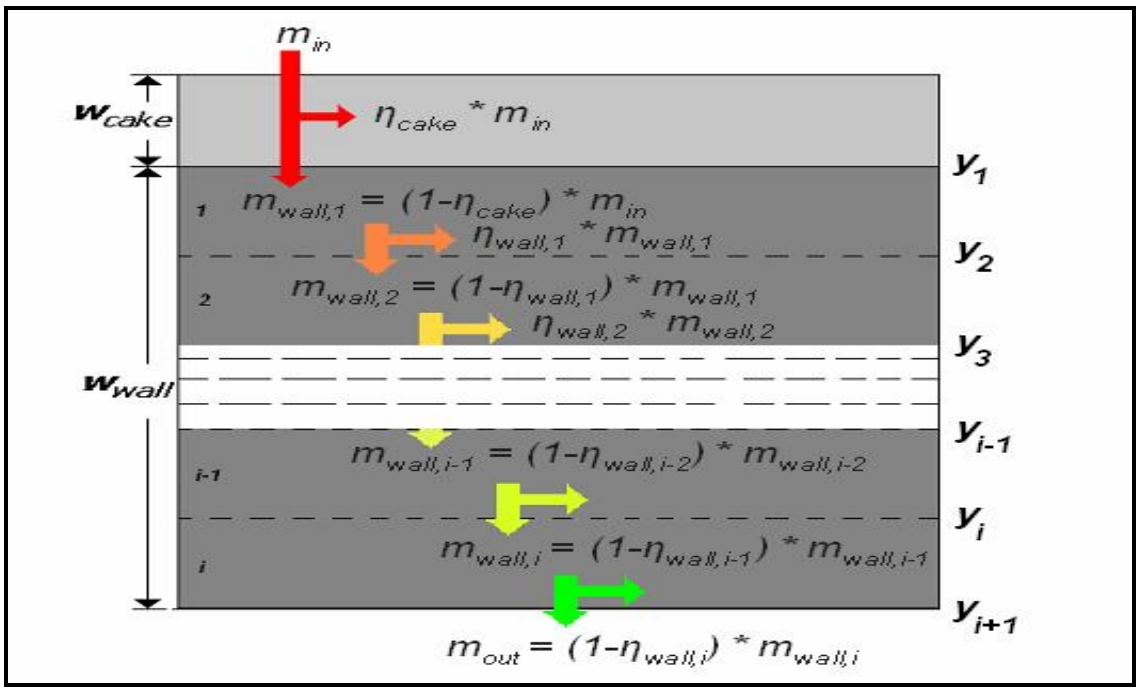

Figure 27: Schematic representation of the two filters in series approach in the CPF model

4.2 EXPERIMENTAL PROCDEDURES

The experimental work involved in this study was conducted on a John Deere 6.8 liter 6 cylinder in-line (turbocharged and after-cooled) engine coupled to a GE AC dynamometer of 750/700 HP rating at 1575-2400 rpm speed range. The fuel used for all experiments was ULSF with a sulfur content of 11.6 ppm and an API gravity of 37 at 15°C. Table 5 shows the specifications of the engine and fuel specifications are given in Table 6.

Table 5: John Deere engine specifications

Model	2004 John Deere 6068H (Development engine)
Type	4 stroke
Cylinders	6, in-line
Aspiration	Turbocharged, After-cooled
Fuel system	High-Pressure common rail
EGR system	Cooled Low-pressure loop EGR
Displacement *(l)*	6.8
Rated Power *(kW)*	187 (@2200 rpm)
Rated Torque *(Nm)*	1000 (@1650 rpm)
Injection Timing	Variable

Table 6: Fuel specifications

ASTM D4502 density @ 15°C *(kg/m^3)*	841.2
Specific gravity @ 15°C	0.8417
API gravity @ 15°C	36.6
Sulfur content *(ppm)*	11.6
Cetane number	48.2
IBP *(°C)*	183
FBP *(°C)*	350

Table 7: DOC and CPF specifications

Parameter	***DOC***	***CPF***
Substrate material	Cordierite	Cordierite
Cell structure	Square	Square
Diameter *(in.)*	10.5	10.5
Channel length *(in.)*	6	12
Cell density *(cpsi)*	400	200
Thermal conductivity *(W/m-K)*	1.3	1.0
Specific heat *(J/kg-K)*	836.8	1000.0

The Johnson-Matthey CCRT® (hereafter referred to as a DOC-CPF) system that was used for the experiments consisted of a *10.5 in. x 6 in., 400 cpsi* DOC and a *10.5 in. x 12 in., 200 cpsi* CPF. Table 7 shows the DOC and CPF specifications in detail.

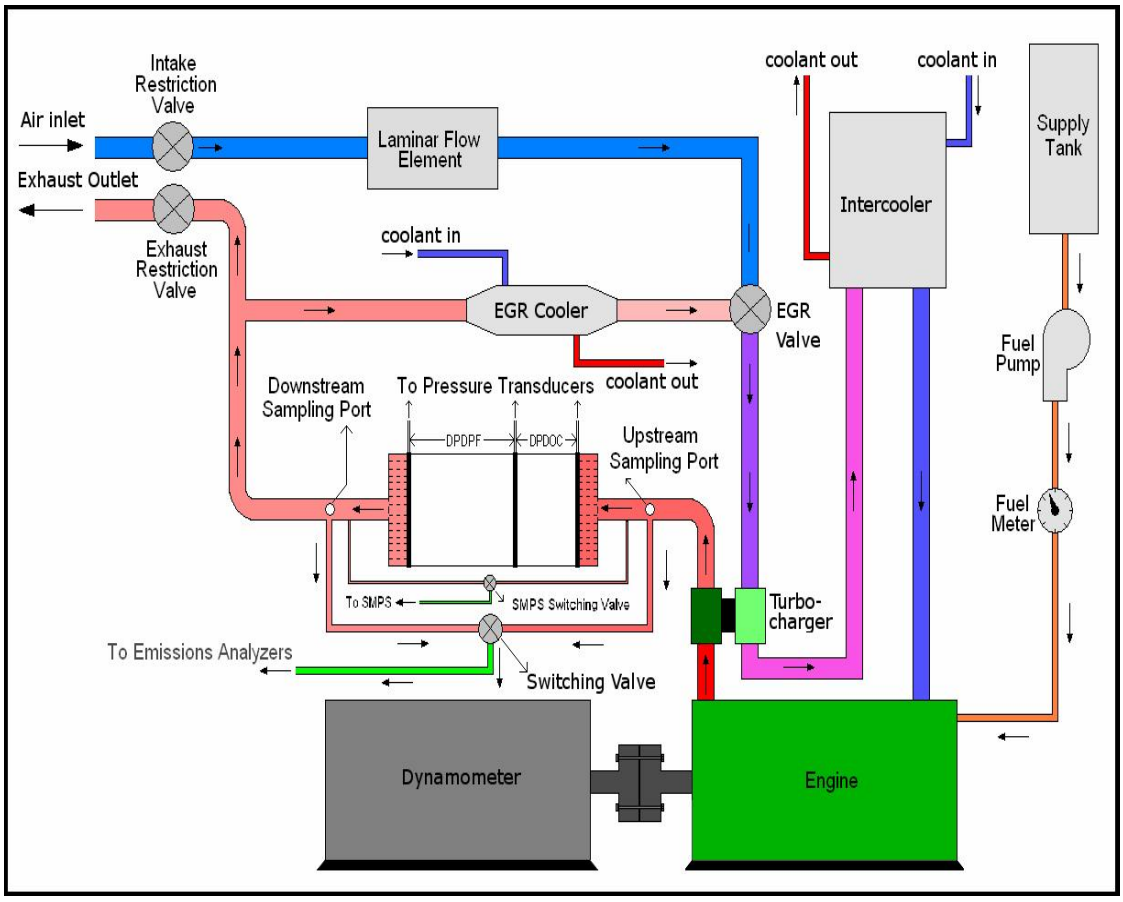

Figure 28: A schematic of the experimental setup [25]

Test matrices were designed to evaluate the performance of the DOC and CPF separately and in combination at two engine speeds. Two DOC experiments were conducted at 2200 and 1650 rpm respectively, and each experiment consisted of engine loads being varied from a minimum of 5% to a maximum of 100% of the engine load at each speed, in steps of 5% engine load with a step-time of 12 minutes. The CPF and DOC+CPF experiments were conducted at 25%, 50%, 75% and 100% of maximum engine load at 2200 and 1650 rpm. These experiments were conducted for a total duration of 9 hours, except in some engine load cases where the CPF pressure drop was steady for more than 3 hours.

4.3 Results and Discussion

4.3.1 Experimental Results

From the DOC-only experiments conducted, the pressure drop across the DOC, DOC inlet and outlet temperatures, and DN-DOC concentrations of 8 species – CO_2, H_2O, O_2, N_2, *CO*, *HC*, *NO* and NO_2 - were obtained as functions of the actual volumetric flow-rate of exhaust through the DOC and absolute exhaust temperatures, which in turn depends on the engine load. Experimental DOC pressure drop and DN-DOC concentrations of species are compared to model-predicted values later in this section. Species concentrations of *CO*, *HC*, *NO* and NO_2 downstream of the DOC predicted by the DOC model calibrated to experimental data at 2200 and 1650 rpm are presented in Appendix A.

Table 8 shows the major engine performance parameters measured for the experiments in the CPF and DOC+CPF configurations at 2200 and 1650 rpm. Proprietary data such as *EGR* have been presented as values normalized to maximum values at given engine speed conditions. UP-CPF temperatures presented in Table 8 are the average steady state values. Standard values of CPF inlet *PM* concentrations $\left(C_{in,std}\right)$ and volumetric flow-rate of exhaust $\left(\dot{V}_{std}\right)$ (at standard conditions of 25°C and 1 atm.) were calculated from the measured values of experimental variables. Total CPF inlet *PM* for the entire loading experiment $\left(PM_{inlet}\right)$ was then calculated for each experiment, as the product of $C_{in,std}$, $\dot{V}_{std}$ and $t_{loading}$ (total loading time in each case). Mathematically,

$$PM_{inlet} = C_{in,std}\,\dot{V}_{std}\,t_{loading}\left(\frac{3600}{1000}\right) \tag{28}$$

Table 9 shows the *PM* oxidation levels (expressed as a percentage of the inlet *PM*) calculated from measuring mass of *PM* deposited in the CPF during the entire loading experiment, for various engine loads. The *PM* oxidation levels in the CPF were higher for higher engine loads (owing to higher temperatures involved) and higher for DOC+CPF configuration compared to CPF configuration (clearly a beneficial effect of the presence of the DOC). The reasons for this are discussed later in this section. Table 9 also shows UP-CPF and DN-CPF concentrations of NO_2 and *NO*, measured during the loading experiments to evaluate the NO_2 available for oxidization with *PM* in the CPF and the amount of NO_2 consumed and produced in the CPF. An effective decrease in NO_2 concentrations was observed in all engine load cases except for the 100% engine load case in the CPF configuration (indicated by the negative sign in the '*NO* increase' and 'NO_2 decrease' rows).

Table 8: Engine data measured from experiments in CPF and DOC+CPF configurations

Engine load (%)	**25**		**50**		**75**		**100**	
	CPF	**DOC+CPF**	**CPF**	**DOC+CPF**	**CPF**	**DOC+CPF**	**CPF**	**DOC+CPF**
2200 rpm								
Load *(Nm)*	203	203	406	406	608	608	811	811
Power *(kW)*	47	47	94	94	140	140	187	185
A/F ratio	43	43	31	32	27	27	24	24
BSFC *(.)*	0.98	1	0.91	0.93	0.86	0.88	0.81	0.83
UP-CPF temp. *(°C)*	250	267	343	364	379	408	405	428
EGR *(.)*	1	0.99	0.99	0.97	0.98	0.95	0.93	0.91
$C_{in,std}$ *(mg/std.m^3)*	6.04	4.16	3.92	2.53	2.82	2.41	2.72	2.96
$\dot{V}_{std}$ *(std.m^3/s)*	0.13	0.13	0.18	0.18	0.22	0.22	0.24	0.25
$t_{loading}$ *(hrs)*	9.0	8.3	9.0	8.1	9.0	8.1	9.0	8.1
PM_{inlet} *(g)*	25.3	16.0	23.0	13.1	19.7	15.4	21.4	21.1
1650 rpm								
Load *(Nm)*	250	250	500	500	750	750	955	940
Power *(kW)*	43	43	86	86	130	130	165	164
A/F ratio	34	34	25	24	21	21	20	20
UP-CPF temp. *(°C)*	272	285	392	420	436	464	490	502
EGR *(.)*	1	1	0.97	0.97	0.96	0.95	0.90	0.90
$C_{in,std}$ *(mg/std.m^3)*	5.43	5.53	2.75	3.15	4.28	6.33	8.52	10.1
$\dot{V}_{std}$ *(std.m^3/s)*	0.09	0.09	0.12	0.11	0.15	0.14	0.17	0.17
$t_{loading}$ *(hrs)*	9.0	8.3	9.0	8.1	9.0	8.1	9.0	8.1
PM_{inlet} *(g)*	16.2	15.1	10.4	10.1	20.2	26.2	48.2	50.0

4.3.2 DOC Modeling Results

In this sub-section, results from the DOC model calibrated to experimental data measured at 2200 rpm are presented. Relevant results obtained from the DOC model calibrated to experimental data at 1650 rpm and species concentration comparisons at 2200 and 1650 rpm are presented in Appendix A.

Table 9: *PM* oxidation levels and NO_2 concentrations measured across the CPF at various loads at 2200 rpm

Engine load (%)		**25**		**50**		**75**		**100**	
		CPF	**DOC+CPF**	**CPF**	**DOC+CPF**	**CPF**	**DOC+CPF**	**CPF**	**DOC+CPF**
***PM**$_{inlet}$ (g)*		25.3	16.0	23.0	13.1	19.7	15.4	21.4	21.1
***PM**$_{dep.}$(g)* [§]		19[§]	12[§]	16[§]	6	12	3	5	2
***% PM**$_{oxid}$ (g)*[§]		25.0[§]	25.1[§]	30.3[§]	54.3	38.9	80.5	76.6	90.5
CPF inlet temp. *(°C)*		250	267	343	364	380	408	405	428
NO_2 conc. *(ppm)*	UP-DOC	-	44	-	45	-	39	-	29
	UP-CPF	38	144	44	101	37	111	27	127
	DN-CPF	12	125	21	65	19	74	33	91
***NO* conc.** *(ppm)*	UP-DOC	-	154	-	99	-	149	-	230
	UP-CPF	160	46	101	44	156	80	264	145
	DN-CPF	185	72	126	81	174	114	259	170
NO increase (ppm)		25	26	25	36	18	34	-5	26
NO_2 decrease (ppm)		27	20	23	40	17	41	-6	36

The DOC pressure drop model calculates the total pressure drop across the DOC according to equation (A.1), and Figure 29. Figure 60 (in Appendix B) show the pressure drop predictions from the DOC model and experimental DOC pressure drop values plotted against actual volumetric flow-rates in each engine load case at 2200 and 1650 rpm respectively. The model-predicted values of DOC pressure drop, although linearly proportional to the actual volumetric flow-rate, were lower than the experimental values of the same. This was due to the fact that the DOC pressure drop equation gives the pressure drop across the substrate only, whereas in the DOC experiments, the pressure drop measured was across the DOC unit, which included the baffles used to make the exhaust flow laminar. It was also found out that by introducing a factor '*C*' in the equation for DOC pressure drop and using a value of *C=2*, DOC pressure drops could be

[§] - PM deposited and therefore, % PM oxidized in some load cases were corrected to account for moisture absorbed in the CPF substrate during weighing procedure (details given in reference [25]).

modeled accurately (within 5% of experimental values), as shown by the 'Model-predicted *ΔP*' plot compared to 'Experimental *ΔP*' values in Figures 29 and 60.

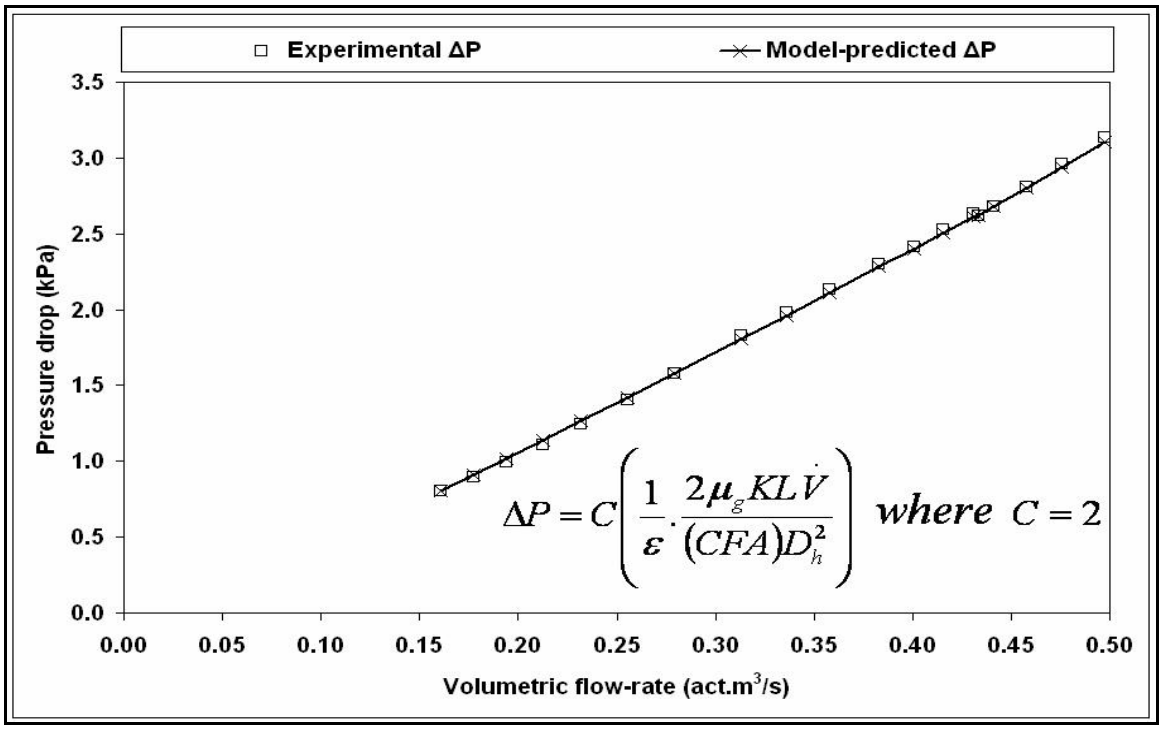

Figure 29: Experimental and model-predicted DOC pressure drop from DOC model calibrated to experimental data at 2200 rpm

Determination of kinetic parameters required for predicting the DOC outlet concentrations of CO, HC, NO and NO_2 as a result of CO, HC and NO oxidation reactions was done using the procedure explained in Appendix A, for experimental data for each engine load case set at 2200 and 1650 rpm respectively. A single set of kinetic parameters which best represent the kinetics occurring at both engine speeds is given in Table 10. Using these values, however, model-predicted values of species concentrations varied considerably from experimental values, especially at certain engine load ranges (See Appendix A).

Table 10: Kinetic parameters obtained from DOC model calibrated to experimental data at 2200 and 1650 rpm

Reactant Species	**Pre-exponential factor**	**Activation Energy**
	(gmol/m^2.s)	*(J/gmol)*
CO	1.82x10^{19}	102821
HC	1.95x10^{24}	95260
NO	2.08x10^{12}	87312

In summary, the DOC model kinetic parameters obtained as shown in Table 10 can be used as 'starting values' for experimental data in the future and model-predicted values of outlet concentrations obtained thus be verified against experimental values. Also, the inhibition factors involved in reaction equations (20) thru (22) need to be changed if found to be necessary from model calibration in the future.

4.3.3 DPF Model Calibration and Modeling Results

The CPF model was calibrated to experimental data measured during CPF loading experiments at 8 engine load cases (4 engine load cases *x* 2 configurations, i.e., CPF and DOC+CPF) at 2200 rpm. The experimentally measured variables used for model calibration were:

1. CPF pressure drop vs. time,
2. Mass of *PM* deposited at the end of each CPF loading experiment,
3. Particle size distribution data from the SMPS system measured at DN-CPF location, and
4. DN-CPF concentrations of NO_2.

The process of calibration of the CPF model involved finding the set of input parameters that produced model-predicted values of the major variables that agreed with experimental values. The effect of changing each of the calibration variables on model results is as follows:

1. Clean wall permeability $\left(k_{t,0}\right)$ was adjusted to match 'clean' (initial) CPF pressure drop values predicted by the model.
2. Adjusting percolation factor $\left(\psi\right)$ changes the initial rate of increase in *PM* cake efficiency with time. A higher value of percolation factor (>0.90) generally means a faster increase in the *PM* cake filtration efficiency during the initial stages of filtration.
3. *PM* packing density in the wall $\left(\rho_{pw}\right)$ determines the rate of increase of volume of wall *PM* collectors per unit *PM* deposited. This means that a particular case with lower ρ_{pw} value (less densely packed *PM*) will have more volume increase of wall collectors (and hence a higher pressure drop due to substrate wall) compared to another case with a higher ρ_{pw} value, all other variables being the same.
4. *PM* cake layer permeability $\left(k_p\right)$ affects the cake pressure drop and hence its contribution to the overall pressure drop. A higher value of k_p (or a more permeable *PM* cake) means lower pressure drop at all times during CPF loading simulation due to the cake compared to a case with a high value of k_p. Since the *PM* cake pressure drop increases from zero in all cases, and since the cake pressure drop is significant during *PM* cake filtration, this variable is adjusted to change the pressure drop characteristics in the *PM* cake filtration regime.
5. *PM* cake layer packing density $\left(\rho_p\right)$ is similar in its function to ρ_{pw}. A simulation with a lower value of ρ_p will have a higher *PM* cake layer thickness at all times compared to one with lower ρ_p values. For this study, a relation between ρ_p and global Peclet number $\left(Pe\right)$ as given in reference [16] is used to interpolate values of ρ_p from global *Pe* values calculated from the initial average wall-flow velocity in each engine load case and initial porosity of the wall. Figure 69 (in Appendix B) shows the curve depicting the relationship between ρ_p and *Pe* (adapted from reference [16]). Since volumetric flow-rates (and hence wall-flow velocities) in similar engine load cases were equal, equal values of ρ_p were also used.
6. Maximum cake efficiency parameter $\left(A_\eta\right)$values affect *PM* cake filtration efficiencies as predicted by a parametric equation (Equation (47) in reference [23]) at every time-step

during simulation. Therefore, the value of this parameter was adjusted to match DN-CPF *PM* volume concentrations to experimental DN-CPF *PM* data calculated from PSD data measured by the SMPS system.

7. Cake collector efficiency ratio parameter $\left(\frac{\eta_c}{d_{c,cake}}\right)$ determines the rate of increase of cake filtration efficiency to its maximum value. In a model simulation using a higher value of $\frac{\eta_c}{d_{c,cake}}$ (in other words, a more efficient *PM* cake layer), the filtration efficiency of the *PM* cake layer increases to its maximum value faster than in a case with a lower value of $\frac{\eta_c}{d_{c,cake}}$.
8. Frequency factor for thermal *PM* oxidation (A_{th}) was kept constant at the value determined from previous research (given in reference [9]).
9. Frequency factor for NO_2/temperature-assisted *PM* oxidation (A_{NO_2}) was adjusted to control the reaction rate of NO_2/temperature-assisted *PM* oxidation reaction occurring in the *PM* cake. A higher value of A_{NO_2} means higher *PM* oxidation rates and hence more *PM* oxidized in the same amount of simulation time than a case with lower value of A_{NO_2}.
10. Frequency factor for NO_2/temperature-assisted *PM* oxidation in the wall $(A_{NO_2,wall})$ was adjusted to change the reaction rate of the NO_2/temperature-assisted *PM* oxidation taking place in the substrate wall. Higher values of $A_{NO_2,wall}$ will result in more *PM* oxidation in the substrate wall, all other variables remaining the same.
11. Frequency factor for NO_2 production (A_{NO}) was adjusted to control the amount of NO_2 produced in the substrate wall as the exhaust gas mixture passes through the substrate wall, so as to match DN-CPF NO_2 concentrations observed from experiments at each engine load case. In general, higher values of A_{NO} will result in higher DN-CPF NO_2 concentrations for a typical model simulation.

The process of calibration of the CPF model involves changing one or more of the variables mentioned above, since some of these variables affect the filtration and/or oxidation processes simultaneously, and compensating for the change of one on the effect of one major variable may involve modification of one or more calibration variables. As mentioned earlier, the quality of a calibrated model is dependent on the level of agreement of model-predicted values of experimentally measured variables. The values of all calibration variables obtained from the calibrated CPF model are given in Tables 17,18,19, and 20 in Appendix C.

Table 11 shows a comparison of experimental initial pressure drop with model-predicted values of the same, showing a -26 to +49% variation in the model-predicted CPF initial pressure drop from experimental values of the same. The variation is due to the following reasons:

- Clean wall permeability $(k_{t,0})$ values given as input to the 1-D CPF model were not constant in all load cases. This was because of the experimental setup design with a single exhaust line which allowed the exhaust gas to pass through the CPF from the time the engine was started. Since the engine reached steady operating state about 2-5 minutes

after starting the engine (which was the time at which pressure drop measurements started), CPF pressure drops were measured at a certain time after small amounts of *PM* was collected in the CPF, and hence the pressure drops recorded were not for the 'clean' filter.

- CPF substrate wall temperatures were not measured because of constraints in measurement of the same, although the CPF initial pressure drop as calculated by the CPF model is a function of initial substrate wall temperatures $(T_{w,0})$also. Hence, initial wall temperatures were assumed to be the average of inlet and outlet temperatures. This assumption could have caused a difference in the actual and calculated values of initial wall temperatures, since the thermal inertia of the substrate was not taken into consideration in the calculations. Due to this, initial pressure drop values calculated by the model also varied accordingly.

Calibration of clean filter permeability values can be carried out effectively using the CPF model by the addition of a 'baseline' to the exhaust line, whereby exhaust gas is routed through the CPF only after the engine has reached steady operating conditions, and the substrate wall temperature can be assumed to be equal to the ambient temperature (Reference [9]).

Figure 30 shows a comparison of experimentally measured and model-predicted pressure drops obtained from the calibrated CPF model in the CPF configuration at the 4 engine load cases (25, 50, 75 and 100%) at 2200 rpm, and Figure 31 shows a similar comparison for the 4 engine load cases in the DOC+CPF configuration at 2200 rpm. A point-to-point comparison of pressure drop between experimental and model-predicted values showed a maximum variation of 0.85 kPa (in the 50% engine load case) in the CPF configuration and 0.80 kPa in the DOC+CPF configuration for the model-predicted values of ΔP. In the DOC+CPF configuration at 100% engine load case, a maximum variation of 1.22 kPa of the model-predicted ΔP from the experimental ΔP was observed, which is due to the CPF pressure drop model not being able to predict the highly transient variation in *PM* oxidation rates in the wall. Overall, good agreement of model-predicted CPF pressure drops was obtained in all cases, especially in the cake filtration regime.

Table 11: Experimental vs. model-predicted CPF initial pressure drop at 2200 rpm

Engine load (%)	**25**		**50**		**75**		**100**	
	CPF	**DOC+CPF**	**CPF**	**DOC+CPF**	**CPF**	**DOC+CPF**	**CPF**	**DOC+CPF**
Expt. ΔP_i *(kPa)*	1.63	1.83	3.25	2.90	4.48	5.20	5.98	6.56
Model ΔP_i *(kPa)*	2.43	2.53	4.32	3.00	4.62	4.75	5.66	4.83
Difference *(kPa)*	.80	.71	1.07	.10	.14	-.45	-.32	-1.7
Difference *(%)*	49	39	33	3	3	-9	-5	-26

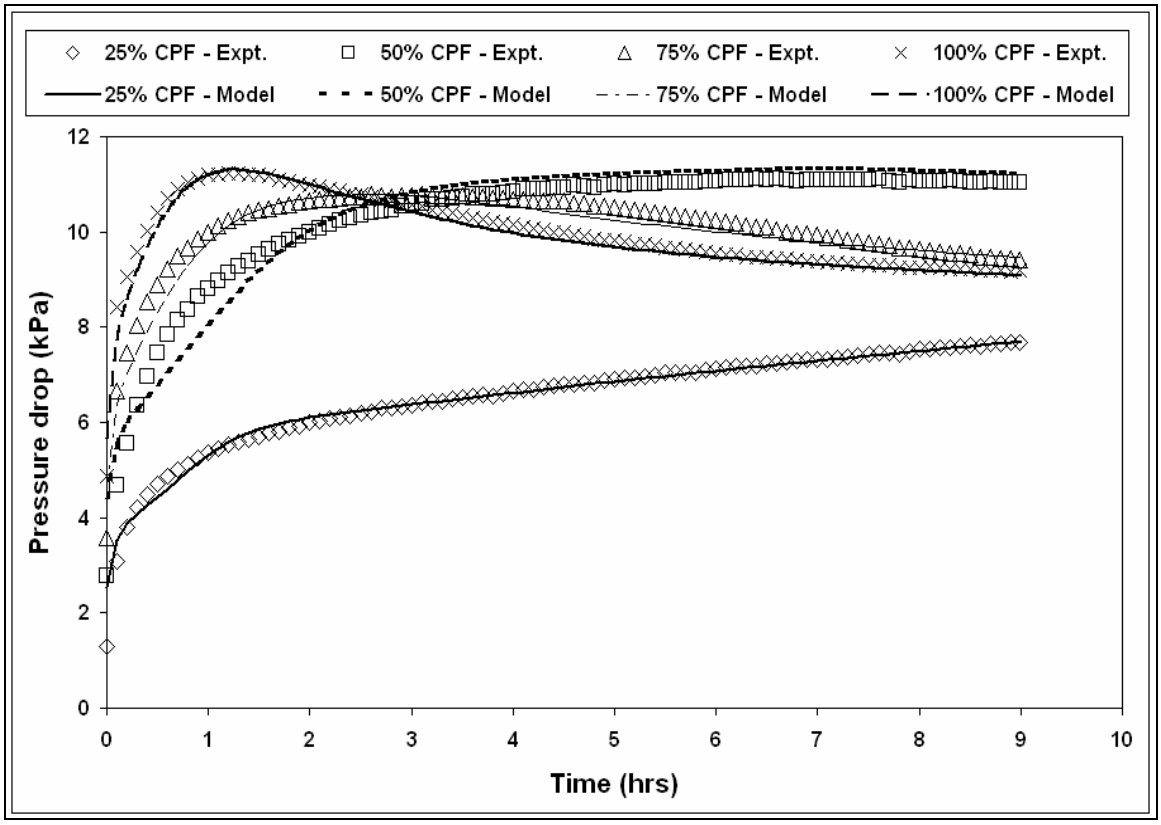

Figure 30: Comparison of experimental and model-predicted CPF pressure drop at various engine load cases in the CPF configuration at 2200 rpm

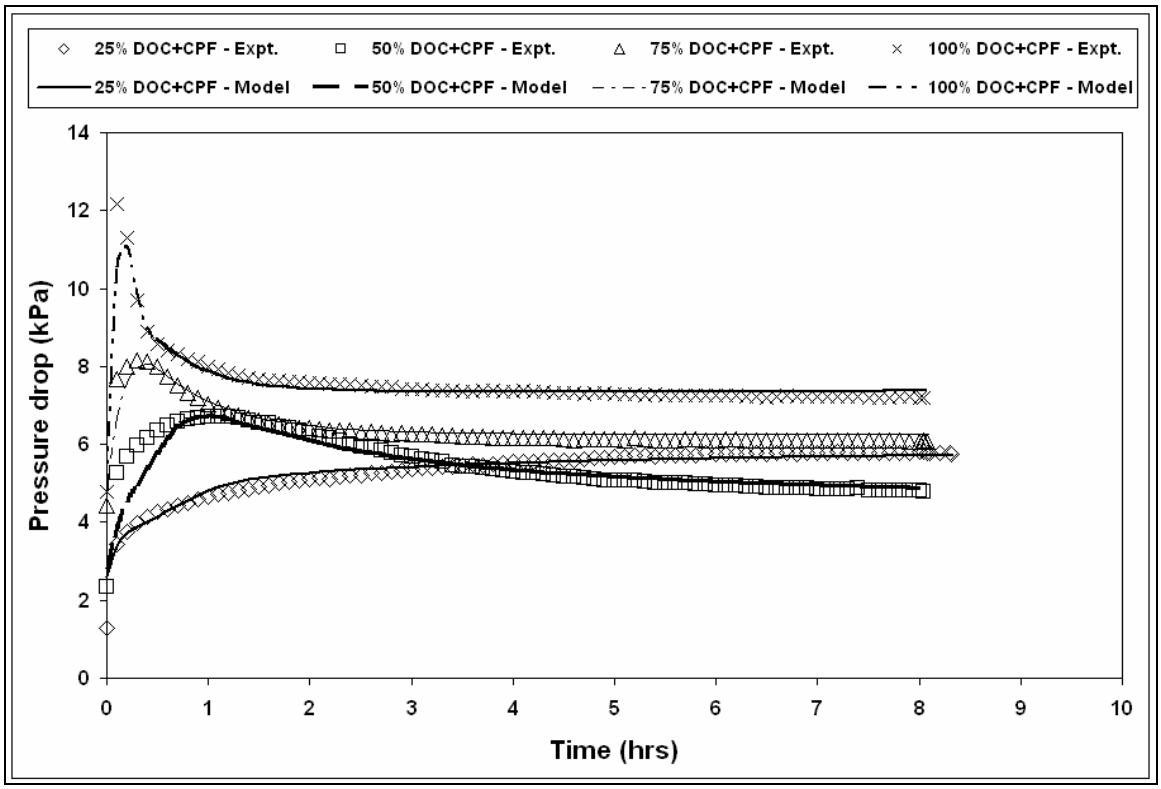

Figure 31: Comparison of experimental and model-predicted CPF pressure drop at various engine load cases in the DOC+CPF configuration at 2200 rpm

The calibrated CPF model also predicts the cumulative CPF mass balance (i.e., a distribution of total *PM* inlet into *PM* deposited, *PM* oxidized and outlet *PM*) at every time-step of simulation. Table 12 shows a comparison of *PM* deposited and *PM* oxidized as obtained from experiments and from model simulations. Since the experimental values of *PM* mass deposited were obtained at different loading times (as shown by the $t_{loading}$ row in Table 13), model-predicted values of the same were also obtained at simulation times equal to the total loading time in each engine load case. Differences for values of '*PM* deposited' in the range of -3.5 to +8.9% were observed between experimental and model-predicted values, and the differences in values of '*PM* oxidized' were in the range of -14 to +12% between experimental and model-predicted values.

Table 12: Comparison of *PM* mass deposited and *PM* oxidized between experimental and model values

Engine load (%)	**25**		**50**		**75**		**100**	
	CPF	**DOC+CPF**	**CPF**	**DOC+CPF**	**CPF**	**DOC+CPF**	**CPF**	**DOC+CPF**
PM_{inlet} *(g)*	25.3	16.0	23.0	13.1	19.7	15.4	21.4	21.1
$PM_{dep.}^{expt.}$ *(g)*	19	12	16	6	12	3	5	2
$PM_{oxid.}^{expt.}$ *(g)*	6.1	3.9	6.8	7.8	7.5	12.2	16.2	19.4
$PM_{dep.}^{model}$ *(g)*	19.3	10.3	15.8	5.9	12.2	3.0	5.4	2.2
$PM_{oxid.}^{model}$ *(g)*	5.6	5.5	6.7	8.0	7.2	12.1	15.7	19.1
Diff. in PM deposited. *(%)*	-2.9	8.9	-1.0	-0.2	-2.6	-1.8	-3.5	-2.1
Diff. in PM oxidized *(%)*	1.7	-14	-1.1	1.7	1.9	1.6	8.0	12.0

Filtration efficiency of the CPF and DN-CPF PM concentrations are also important parameters to be monitored during calibration of the CPF model. Overall filtration efficiency of the CPF at any instant of simulation time determines the instantaneous amount of *PM* exiting the CPF (i.e., DN-CPF PM concentration). The overall filtration efficiency of the CPF, in turn, depends on the individual efficiency of the *PM* cake layer and substrate wall, and is in turn dependent on *PM* loading in the *PM* cake layer and the substrate wall as well as the physical properties of the *PM* cake and the wall.

Table 23: DN-CPF particle volume concentrations - a comparison of experimental and model-predicted values from samples at 3 loading times

Engine Load (%)	**25**		**50**		**75**		**100**	
	CPF	**DOC+CPF**	**CPF**	**DOC+CPF**	**CPF**	**DOC+CPF**	**CPF**	**DOC+CPF**
$t_{loading}$ = 4 hrs								
Expt. DN-CPF PVC *($m^3/std.m^3$)*	**3.6**	**1.0**	**1.1**	**2.5**	**0.9**	**1.5**	**2.9**	**3.1**
Model DN-CPF PVC *($m^3/std.m^3$)*	**3.0**	**1.3**	**1.3**	**1.5**	**1.1**	**1.8**	**3.2**	**3.3**
Difference *(%)*	**-18**	**31**	**20**	**-38**	**13**	**27**	**11**	**7**
$t_{loading}$ = 6 hrs								
Expt. DN-CPF PVC *($m^3/std.m^3$)*	**3.6**	**1.0**	**1.1**	**2.5**	**0.9**	**1.5**	**2.9**	**3.1**
Model DN-CPF PVC *($m^3/std.m^3$)*	**2.9**	**1.4**	**1.2**	**1.6**	**1.1**	**1.8**	**3.3**	**3.3**
Difference *(%)*	**-20**	**33**	**14**	**-34**	**15**	**27**	**14**	**7**
$t_{loading}$ = 8 hrs								
Expt. DN-CPF PVC *($m^3/std.m^3$)*	**3.6**	**1.0**	**1.1**	**2.5**	**0.9**	**1.5**	**2.9**	**3.1**
Model DN-CPF PVC *($m^3/std.m^3$)*	**2.8**	**1.4**	**1.2**	**1.7**	**1.1**	**1.8**	**3.4**	**3.3**
Difference *(%)*	**-22**	**35**	**12**	**-32**	**19**	**27**	**17**	**8**

DN-CPF *PM* concentration obtained from the experiments conducted were not reliable since outlet *PM* concentrations were not accurately measurable (details are given in reference [25]). Due to this, PSD data obtained from the SMPS system was used to obtain DN-CPF *PM* volume concentrations (instead of the usual DN-CPF *PM* mass concentrations) obtained as functions of loading time. The same were calculated from the model as functions of simulation time, and values at the same times were compared to obtain a direct comparison between experimental and model-predicted values of outlet PM concentrations (as shown in Table 13) and hence, CPF filtration efficiencies.

For each engine load case in Table 13, 3 loading times (*4, 6 and 8 hrs*) were chosen to compare experimental and model-predicted values. The rows labeled 'Difference' show

that the variation in the model-predicted values of DN-CPF *PM* concentrations were in the -38 to 35% range. It is also worth mentioning here that the overall filtration efficiencies corresponding to this seemingly large variation in model-predicted DN-CPF *PM* concentrations were within ±0.5% of the experimental values. This is because $C_{out} = C_{in}(1-\eta)$ and a small variation in η causes a large change in C_{out} (Shende et al. - Reference [30]).

Calibrating the CPF model filtration efficiencies (as explained above) also resulted in good agreement in the DN-CPF PSD predicted by the model as compared to experimental values.

Figure 32 and Figure 33 show experimental average UP-CPF PSD data (used as input to the CPF model) and comparisons of DN-CPF PSD from experimental values and model-predicted values at the same loading time (*8 hrs*) for the 25% and 100% engine load cases in the CPF configuration, while Figure 76 and Figure 77 (in Appendix B) show similar plots for the 25% and 100% engine load case in the DOC+CPF configuration, showing the agreement of experimental and model-predicted PSD values for the particle size range measured (*~15-650 nm dia.*). DN-CPF PSD comparisons of all engine load cases for which the CPF model was calibrated to are given in reference [25].

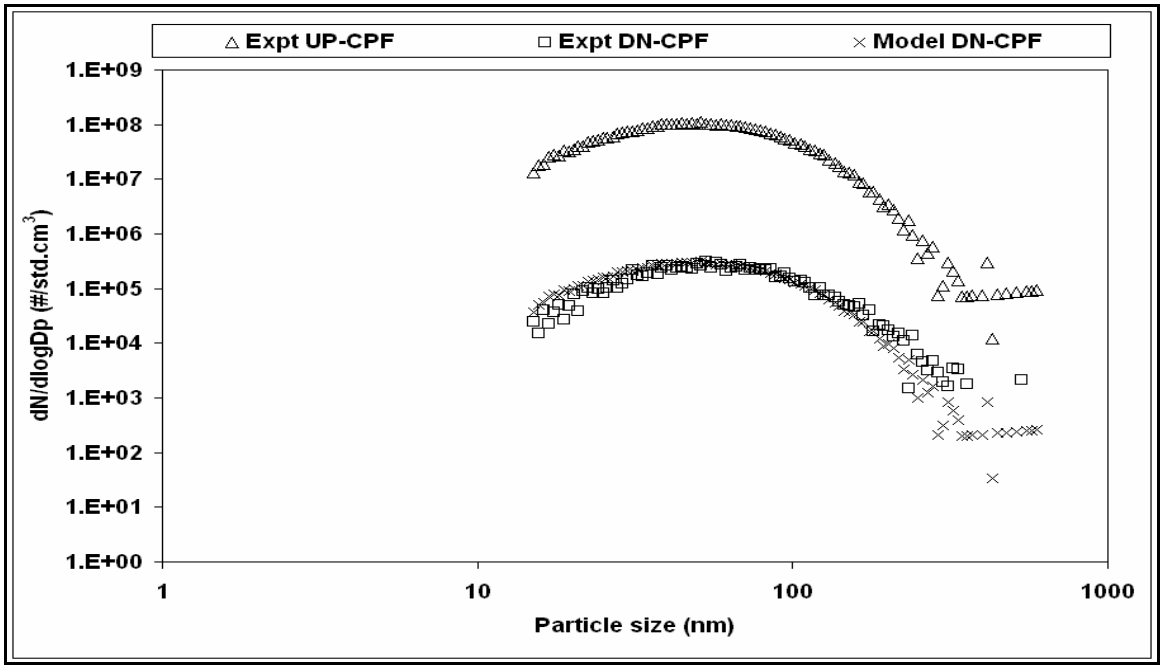

Figure 32: Average UP-CPF PSD and a comparison of experimental DN-CPF PSD at 8 hours of loading time and model-predicted DN-CPF PSD at 8 hrs of simulation time, for the 25% engine load case in the CPF configuration at 2200 rpm

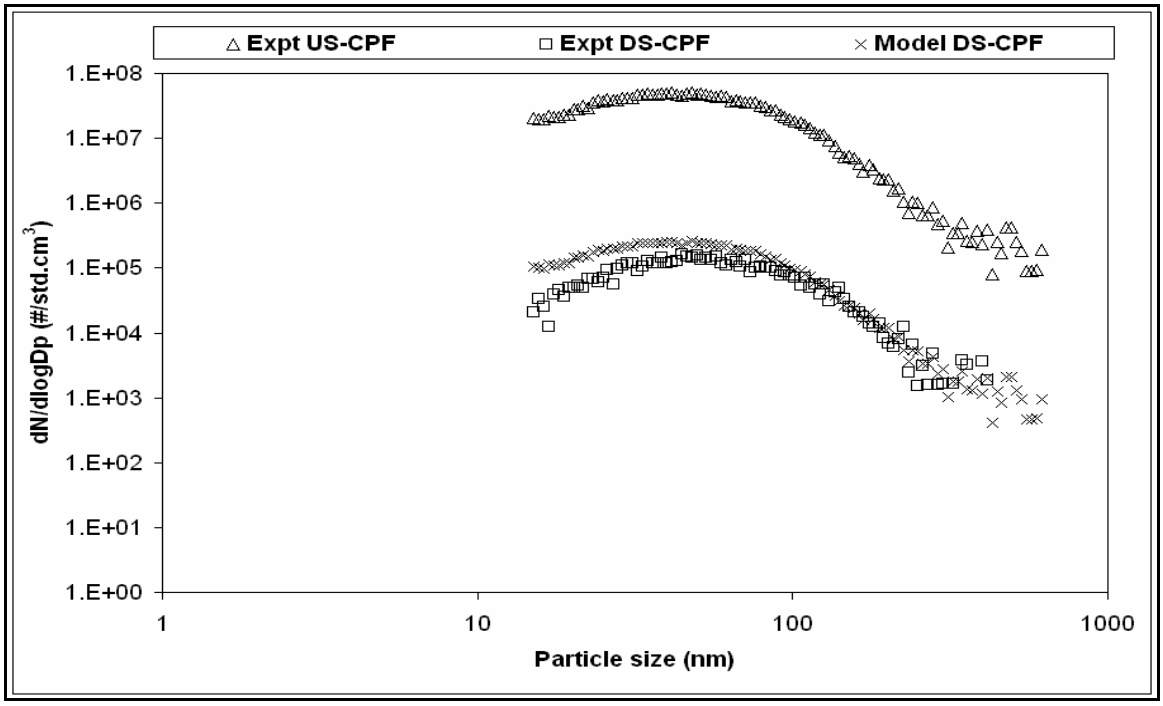

Figure 33: Average UP-CPF PSD and a comparison of experimental DN-CPF PSD at 8 hours of loading time and model-predicted DN-CPF PSD at 8 hrs of simulation time, for the 100% engine load case in the CPF configuration at 2200 rpm

DN-CPF concentrations of NO_2 were also of interest in this study, since from previous research using a similar DOC+CPF system on a different engine (shown in reference [31]), it was observed that NO_2 was produced as the exhaust gas mixture passed through the substrate wall, and in the CPF configuration, this NO_2 further helped in oxidizing more *PM* via the NO_2/temperature-assisted *PM* oxidation mechanism in the wall. Table 14 shows the experimentally measured values of UP-CPF and DN-CPF NO_2 concentrations during this study, and a distribution of NO_2 produced and consumed by *PM* in the CPF, as obtained from the calibrated model. From the experimental values, it is notable that the NO_2 production trend in the CPF used in this study was different from that in previous research [31]. DN-CPF NO_2 concentrations in all engine load cases (except in the 100% engine load case in the CPF configuration) were lower than the UP-CPF NO_2 concentrations, indicating that consumption of NO_2 was more than production of NO_2 in the CPF substrate wall. This results in outlet NO_2 concentrations being lower than that observed from previous research. This also meant that as the exhaust gas mixture passed through the substrate wall of the CPF, lower amount of NO_2 was available for *PM* oxidation and resulted in lower wall oxidation rates compared to a CPF in which there is substantial NO_2 production and *PM* oxidation by the NO_2 thus produced (41-63% of *PM* oxidation by NO_2 generated in the CPF was observed in CPF configuration in previous research at MTU – reference [31]).

Model-predicted DN-CPF NO_2 concentrations excluding NO_2 production were always higher than experimental DN-CPF NO_2 concentrations, indicating that *PM* oxidation was not the only mechanism through which NO_2 was being consumed. The other possible mechanism that consumes NO_2 would be the dissociation of NO_2 to form *NO* and O_2 (which is not currently included in the 1-D CPF model). This is also supported by the fact that the total NO_x concentrations were conserved (within *±2 ppm* of UP-DOC values) at the measurement locations (UP-DOC, UP-CPF, and DN-CPF) as can be seen from the NO_x concentration rows in Table 14. Details about this are given in reference [25].

The variation of DN-CPF NO_2 concentrations from the trends that were expected from previous research at MTU (References [9 and 31]) conducted on a different engine equipped with a similar exhaust after-treatment system could be due to differences in catalyst loading levels. The DOC+CPF unit used in this study showed considerably lower amounts of NO_2 consumed by PM (*3.2 – 8.8 ppm* from Table 14) also, but this is primarily due to the low amounts of CPF inlet *PM* concentrations (or '*PM* available for oxidation with NO_2' *– 2.5-6 mg/std.m*^{3} as shown in Table 8 compared to *11-24 mg/std.m*^{3} as given in Reference [31]). A comparison of the important model parameters obtained from the calibrated CPF model in this study and the previous research work (Reference [31]) are shown in Appendix B.

Table 14: A comparison of NO_2 produced vs. NO_2 consumed as predicted by the CPF model in various engine load cases

Engine Load (%)		**25**		**50**		**75**		**100**	
		CPF	**DOC+CPF**	**CPF**	**DOC+CPF**	**CPF**	**DOC+CPF**	**CPF**	**DOC+CPF**
NO_x (ppm)	UP-DOC	-	198	-	143	-	188	-	259
	UP-CPF	198	198	145	145	193	188	291	260
	DN-CPF	196	197	147	146	193	188	292	261
NO (ppm)	UP-DOC	-	154	-	99	-	149	-	230
	UP-CPF	160	46	101	44	156	80	264	145
	DN-CPF	185	72	126	81	174	114	259	170
NO_2 (ppm)	UP-DOC	-	44	-	45	-	39	-	29
	UP-CPF	38	144	44	101	37	111	27	127
	DN-CPF	12	125	21	65	19	74	32	91
NO_2 consumed by *PM* oxidation *(ppm)*		3.2	7.8	5.5	6.7	3.5	4.9	4.5	8.8
Model outlet NO_2 excluding NO_2 prodn. *(ppm)*		35	136	39	94	34	106	23	118
NO_2 produced *(ppm)*		0	0	0	0	0	0	8.7	0
Model outlet NO_2 including NO_2 prodn. *(ppm)*		35	136	39	94	34	106	31	118

ANALYSIS OF CALIBRATED CPF MODEL RESULTS

In order to understand the effect of engine load (with increasing engine loads, the volumetric flow rates of the exhaust and exhaust temperature also increase) and configuration (CPF as compared to DOC+CPF), the simulation results from the CPF model calibrated to experimental data at 25% and 100% engine load cases in CPF and DOC+CPF configurations at 2200 rpm are discussed. Data from CPF model simulations at 50% engine load case in CPF and DOC+CPF configurations at 2200 rpm is shown in Appendix B.

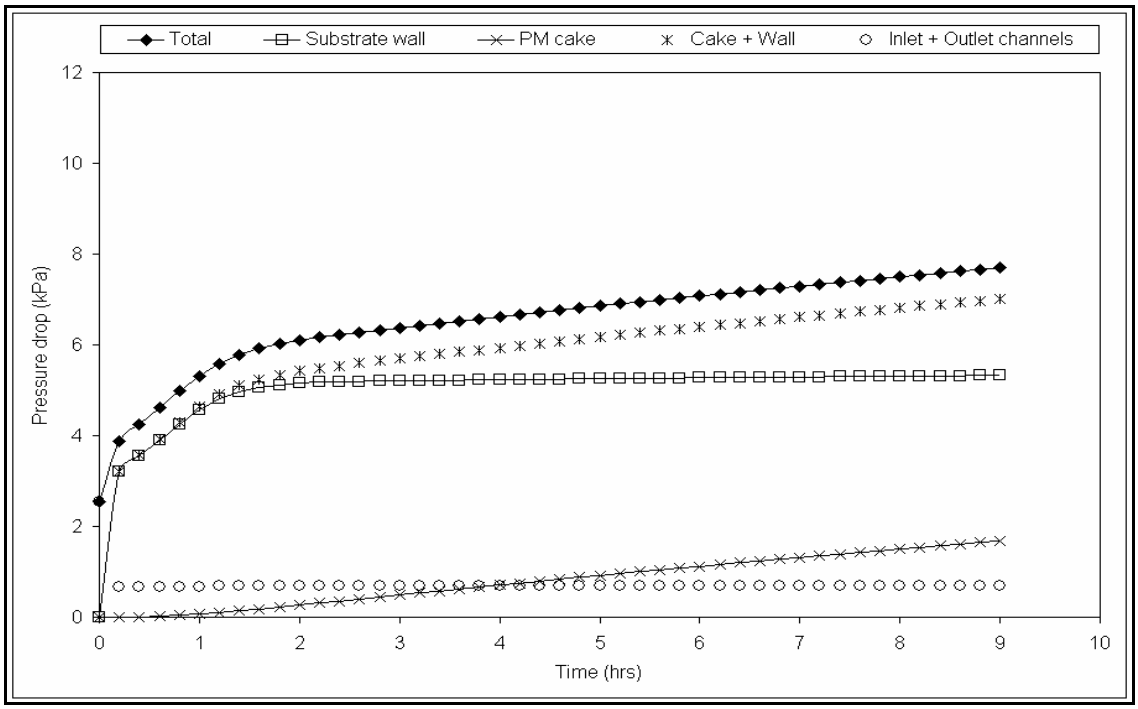

Figure 34: Components of CPF pressure drop from calibrated CPF model in CPF configuration at 25% engine load at 2200 rpm

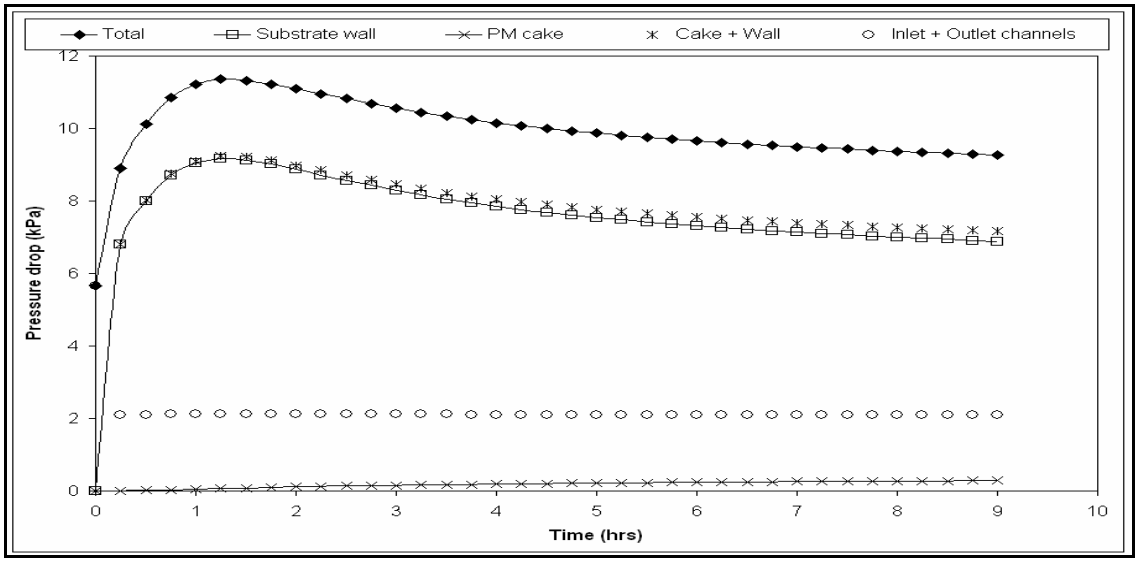

Figure 35: Components of CPF pressure drop from calibrated CPF model in CPF configuration at 100% engine load at 2200 rpm

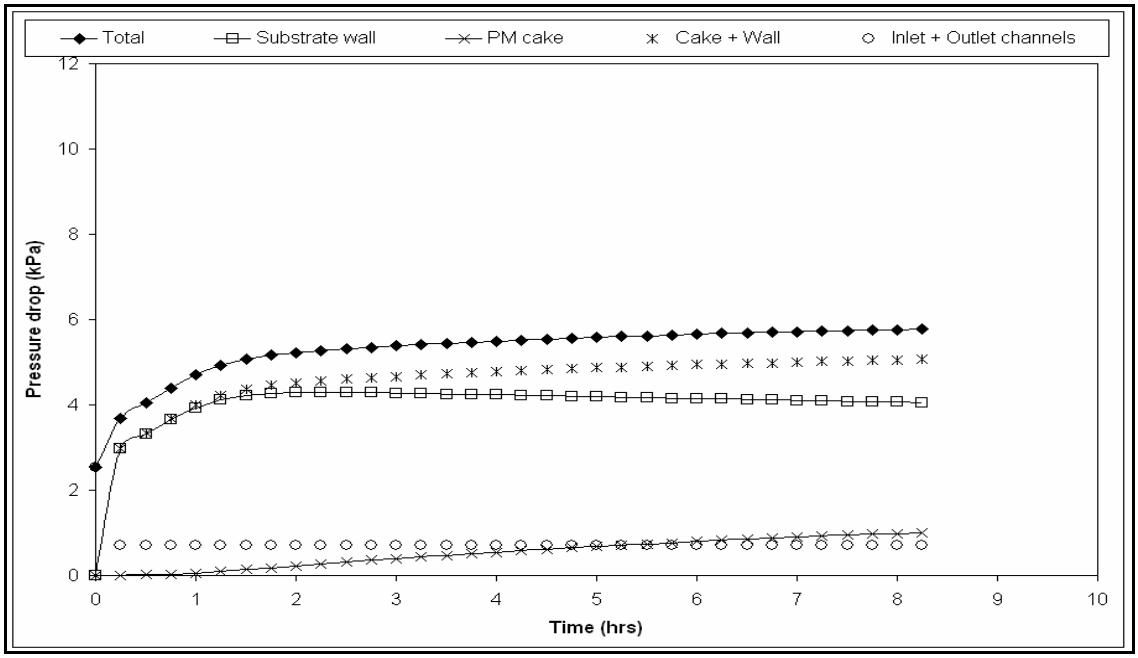

Figure 36: Components of CPF pressure drop from calibrated CPF model in DOC+CPF configuration at 25% engine load at 2200 rpm

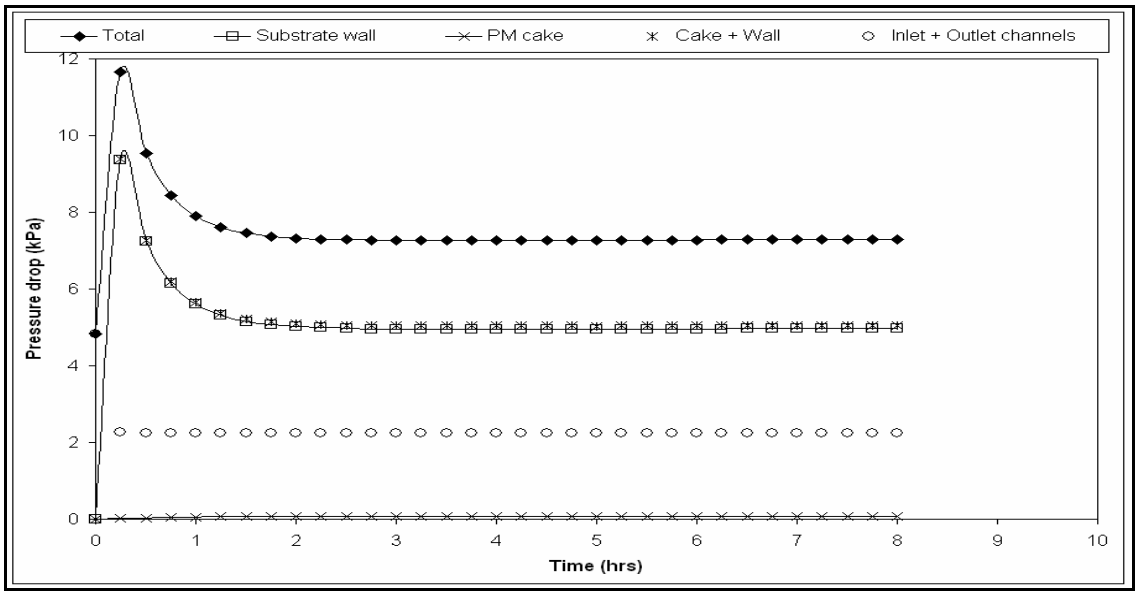

Figure 37: Components of CPF pressure drop from calibrated CPF model in DOC+CPF configuration at 100% engine load at 2200 rpm

The CPF model uses a pressure drop model which calculates the individual components of the pressure drop as the exhaust gas mixture passes through the inlet channel, *PM* cake layer, substrate wall and outlet channel, and hence, the model predicts the overall pressure drop as well as its components. Figure 34 and Figure 35 show the distribution of pressure drop from the calibrated CPF model in the 25% and 100% engine load cases respectively, in the CPF configuration at 2200 rpm, and Figure 36 and Figure 37 show similar plots at 25% and 100% engine load cases respectively, in the DOC+CPF configuration, so that a 'vertical' comparison of plots gives the effect of engine load and a 'horizontal' comparison gives the effect of configuration on CPF pressure drop components. A comparison of pressure drop components in same configurations at different engine load cases (Figure 34 vs. Figure 35 and Figure 36 vs. Figure 37) shows

that the overall CPF pressure drop in a higher engine load case was always higher than that in a lower engine load case, which can be attributed to higher actual exhaust volumetric flow-rates and higher exhaust temperatures as engine load increases. Also, inlet and outlet channel pressure drop, being linear functions of volumetric flow rates, increased with increasing engine loads, and were similar for the same engine load case in different configurations.

Another relevant observation was that the pressure drop due to *PM* cake layer was always lower in the higher engine load cases in both configurations (CPF and DOC+CPF). The reason for this is the higher oxidation level (as explained later) observed at higher engine load case in both configurations, compared to lower engine load cases. This means that the *PM* cake layer is thinner in the higher engine load cases, causing the pressure drop across the *PM* cake to be lower compared to that in lower engine load cases with thicker *PM* cake layers. This will be shown in later figures in this section.

A study of the effect of configuration (CPF vs. DOC+CPF) on pressure drop components can also be made by comparing Figure 34 with Figure 36 and Figure 35 with Figure 37. The important observation here is that higher oxidation levels in the *PM* cake as well as in the substrate wall in the DOC+CPF configuration (as seen from Figure 56 and Figure 57 later in this section) cause the overall pressure drop to be lower than those in the CPF configuration. Also, at 100% engine load case, the peak in pressure drop in the DOC+CPF configuration was observed to be sharper than that in the CPF configuration, and occurred at *6 minutes* of loading time for the DOC+CPF configuration compared to about *1 hr* in the CPF configuration.

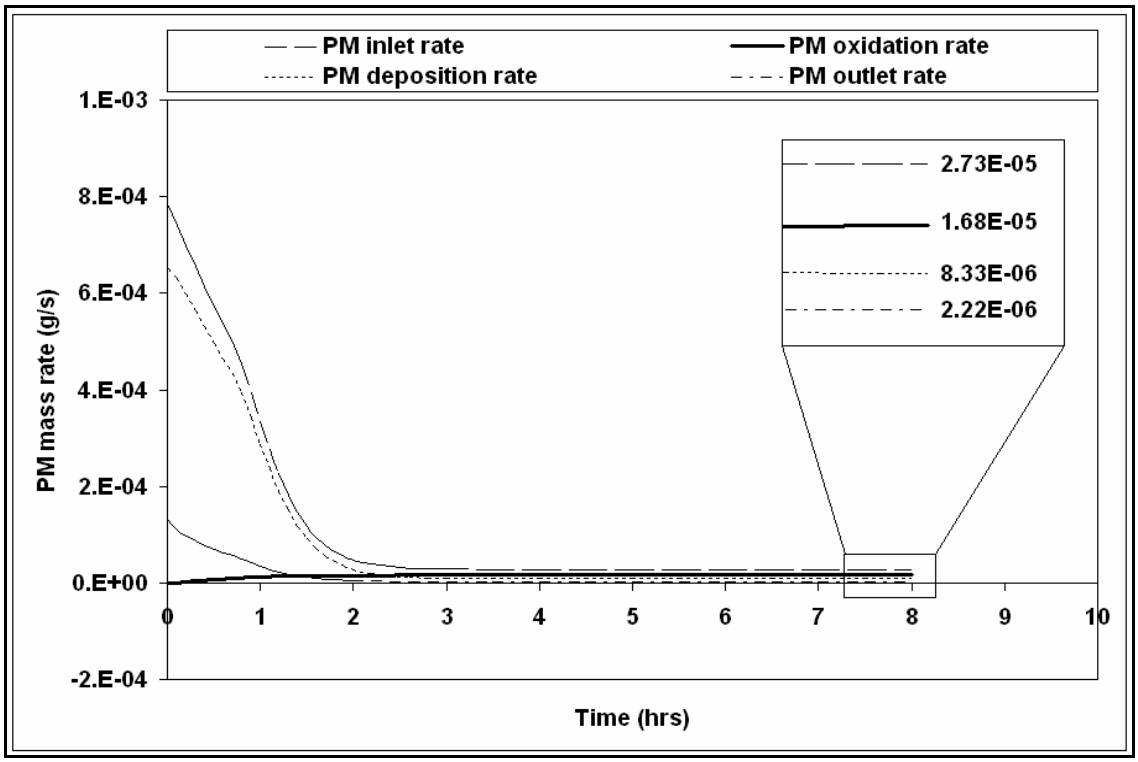

Figure 38: PM mass rates in the substrate wall at 25% engine load case in the CPF configuration at 2200 rpm

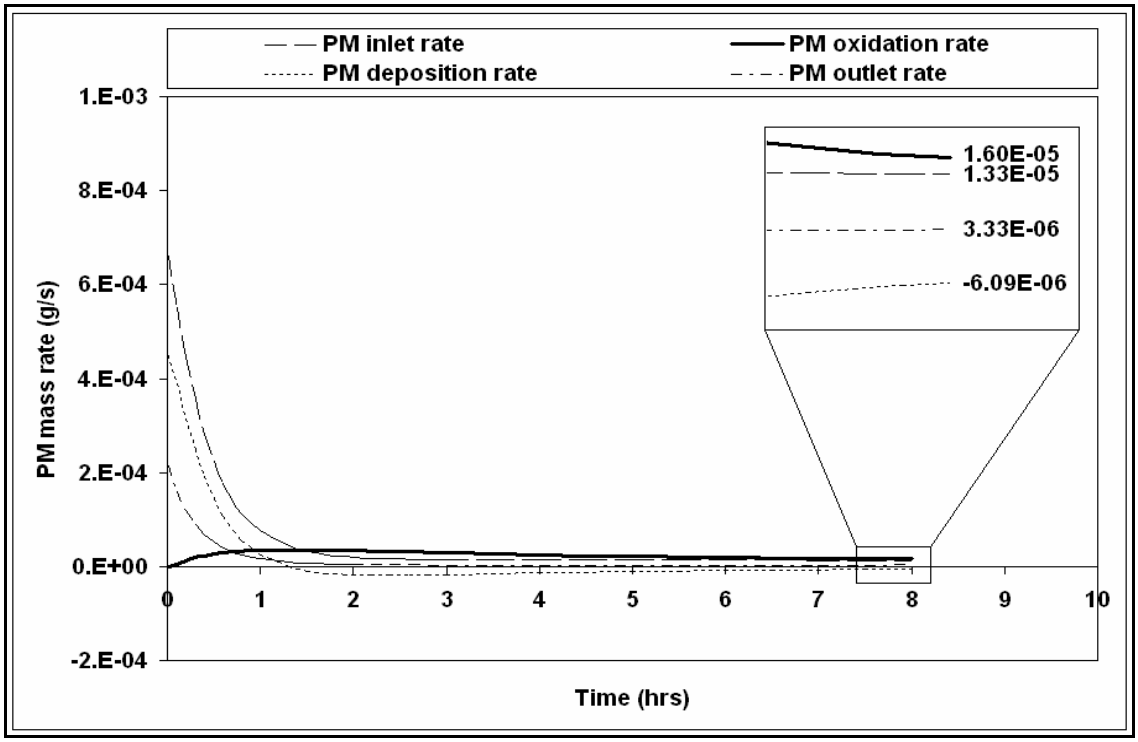

Figure 39: PM mass rates in the substrate wall at 100% engine load case in the CPF configuration at 2200 rpm

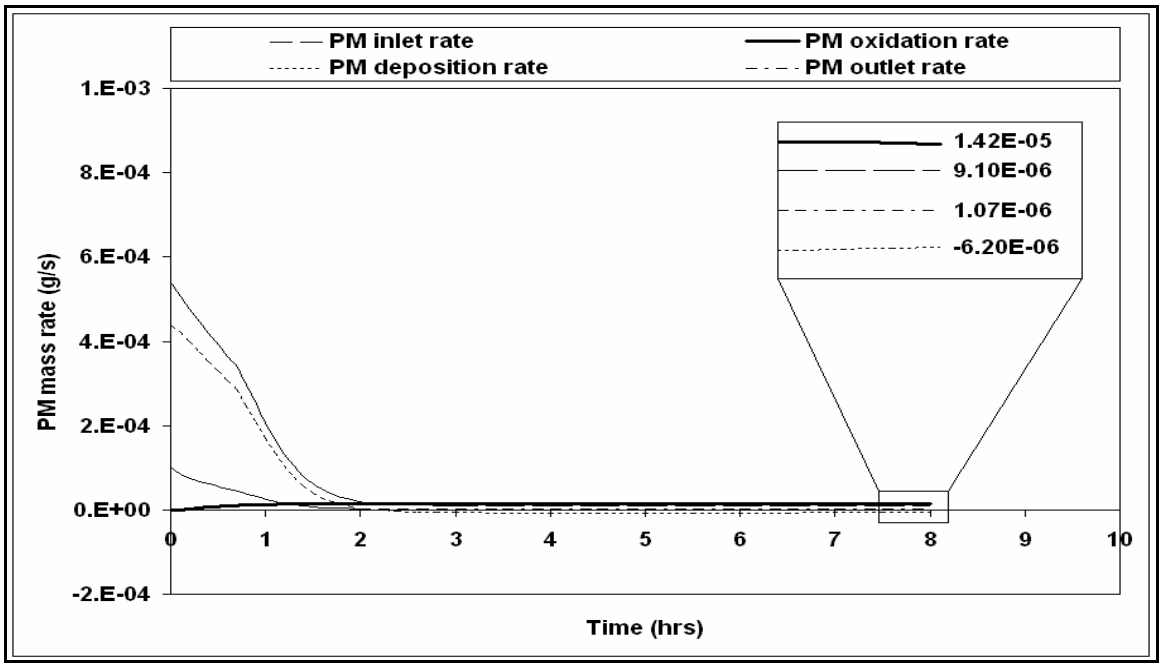

Figure 40: PM mass rates in the substrate wall at 25% engine load case in the DOC+CPF configuration at 2200 rpm

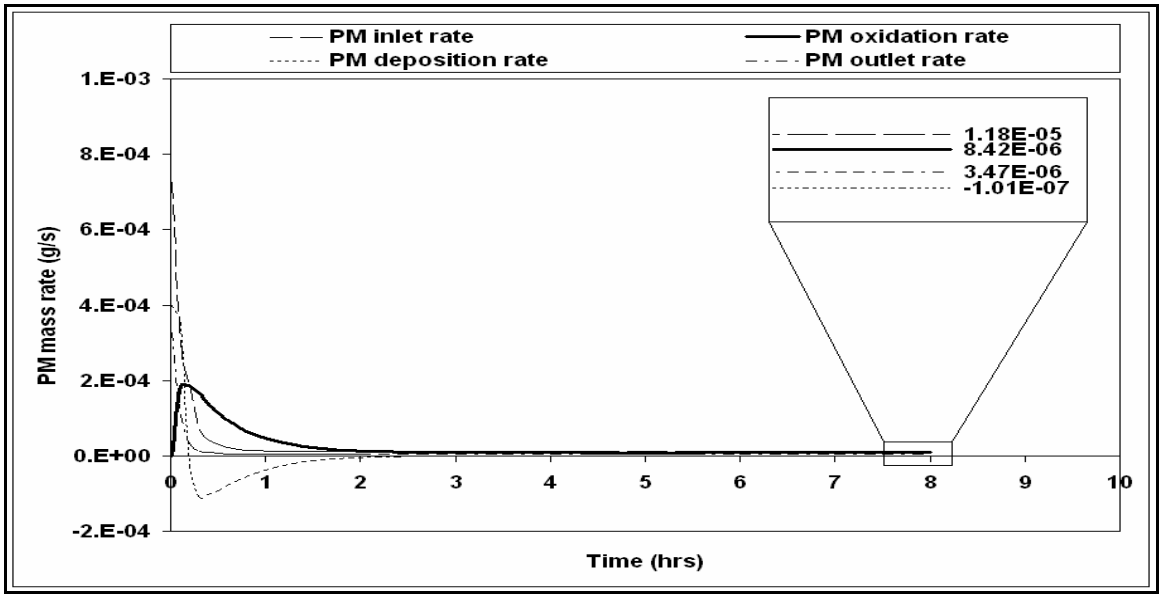

Figure 41: PM mass rates in the substrate wall at 100% engine load case in the DOC+CPF configuration at 2200 rpm

Figure 38 thru 41 show plots of distribution of PM mass rates in the substrate wall as functions of loading time, at the 25 and 100% engine load cases in CPF and DOC+CPF configurations. Corresponding plots for 50% engine load case are shown in Appendix B (Figure 80 thru Figure 83). The PM mass rates (resulting from PM mass rate balance) can be sub-divided into inlet rate, oxidation rate, deposition rate and outlet rate. At any time instant during simulation, the sum of PM oxidation rate, PM deposition rate and PM outlet rate is equal to the PM inlet rate. This is a new feature of the CPF model. Since PM deposition rates in the substrate wall (along with 'ρ_{pw}' values used) determine the pressure drop due to the wall and hence the overall pressure drop, PM mass rate plots in the substrate wall can be used to explain the pressure drop characteristics of the CPF in various engine load cases.

At all engine load cases, the PM inlet rates in the substrate wall are equal to the outlet rates in the PM cake layer, since the PM cake is the first filter in series. PM inlet rates in the substrate wall at initiation of simulation (*time = 0*) are always equal to the PM inlet rate into the CPF, since the PM cake layer is not present at this time instant, and PM inlet rates in the substrate wall always decrease with time during the initial (deep-bed) stage of filtration, since the PM cake layer is building up during this time, and become steady once the PM cake layer efficiency has reached its maximum value (as specified by the user input, A_η).

PM oxidation rates in the substrate wall are dependent on the substrate wall temperatures and also PM available for oxidation and NO_2 available to oxidize the PM present. Therefore, wall PM oxidation rates at the same engine load case in the DOC+CPF configuration were higher than those for CPF configuration.

At any given time instant at a particular engine load case, a positive value of PM deposition rate in the substrate wall means an increase in the CPF pressure drop (as can be seen from comparing, for example, Figure 38 with Figure 40 or Figure 39 with Figure 41), and a negative value of PM deposition rate in the substrate wall means a decrease in

CPF pressure drop (as can be seen by comparing Figure 35 with Figure 37 or Figure 34 with Figure 36). An extension to this observation is that the 'peak' in the CPF pressure drop at any engine load case occurs at the time instant where the PM deposition rate in the substrate wall crosses the x axis (from positive to negative values).

PM outlet rates are always positive, since the CPF does not attain 100% overall filtration efficiency at any time instant.

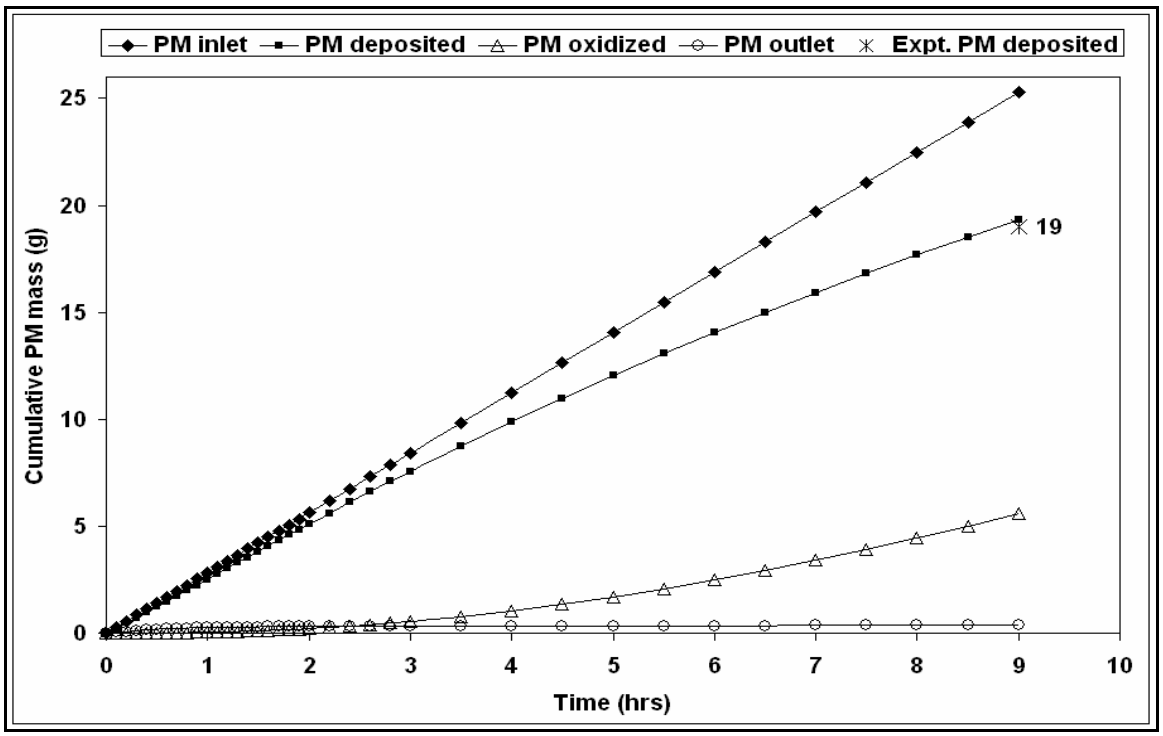

Figure 42: *PM* mass balance curves obtained from the calibrated CPF model at 25% engine load case in the CPF configuration at 2200 rpm

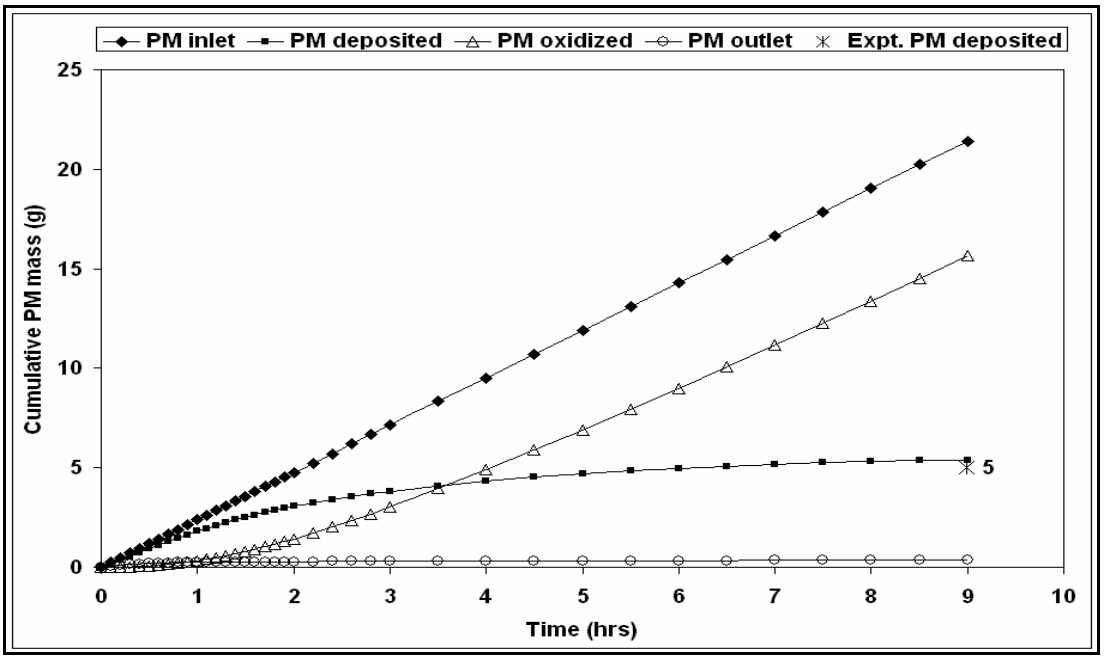

Figure 43: *PM* mass balance curves obtained from the calibrated CPF model at 100% engine load case in the CPF configuration at 2200 rpm

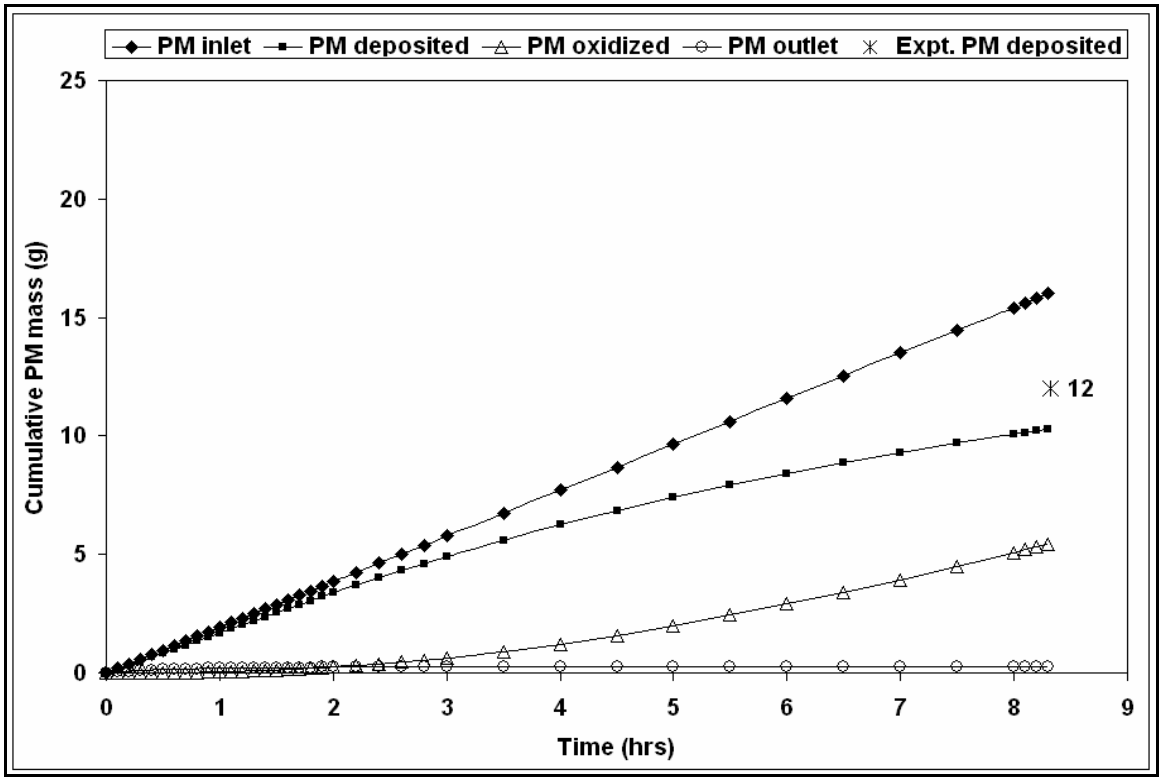

Figure 44: *PM* mass balance curves obtained from the calibrated CPF model at 25% engine load case in the DOC+CPF configuration at 2200 rpm

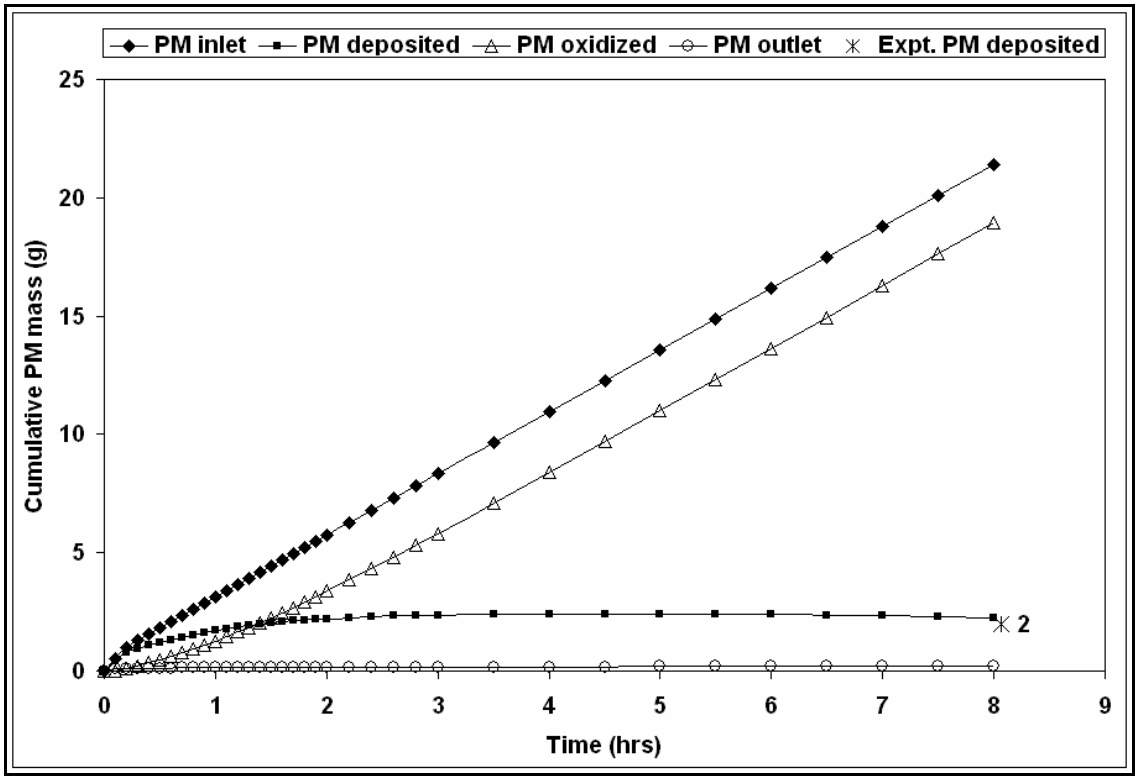

Figure 45: *PM* mass balance curves obtained from the calibrated CPF model at 100% engine load case in the DOC+CPF configuration at 2200 rpm

Figure 42 thru Figure 45 show the mass balance curves from the calibrated CPF model outputs for the 4 engine load cases studied. The experimental *PM* mass deposited in the CPF at the end of loading are also shown, labeled by their numeric values in *grams*. '*PM* inlet' curves for each engine load case were linear since the CPF inlet *PM* concentrations and volumetric flow rates for the CPF model were considered to be the load-average values. '*PM* deposited' for each engine load case shows the cumulative values, and was the sum of *PM* deposited in the *PM* cake layer as well as the substrate wall, although the majority of *PM* mass deposited was in the *PM* cake layer, as will be discussed later in this section. Similarly, '*PM* oxidized' curves also were the sums of *PM* mass oxidized in the *PM* cake layer and substrate wall. '*PM* outlet' curves show the cumulative *PM* mass that had exited the CPF till the particular loading time since start of loading simulation.

Cumulative *PM* mass oxidized was always higher for higher engine load cases in the same configuration, as can be seen from a comparison of Figure 42 vs. Figure 43 and Figure 44 vs. Figure 45. This is clearly an effect of higher exhaust temperatures and NO_2 flow-rates causing higher *PM* oxidation rates, mainly in the *PM* cake layer.

PM mass oxidized in the DOC+CPF configuration compared to the CPF configuration in the same engine load case were also higher due to higher *PM* oxidation rates in the DOC+CPF configuration due to the availability of higher concentrations of NO_2 from the DOC present in the DOC+CPF configuration. A comparison of the model-predicted and experimental values of percentage *PM* oxidized and *PM* deposited in all the 8 engine load cases that the CPF model was calibrated to is also given in Table 12, which augment the findings about the trends discussed above.

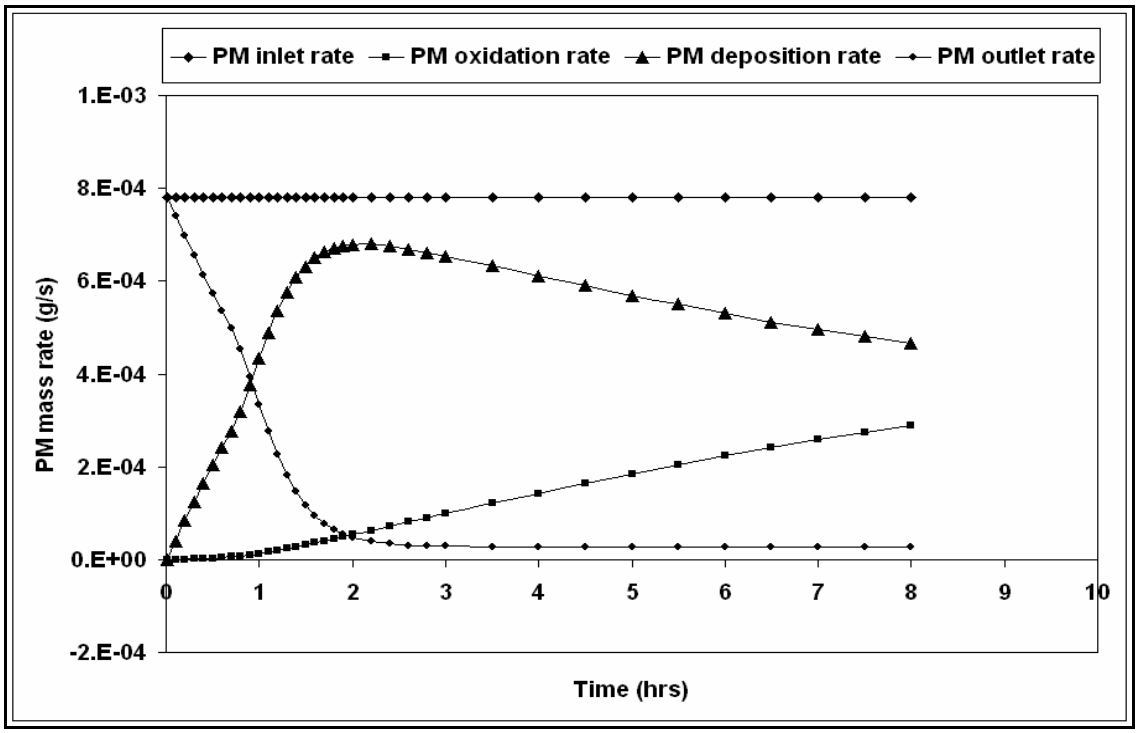

Figure 46: PM mass rates in the PM cake layer at 25% engine load case in the CPF configuration at 2200 rpm

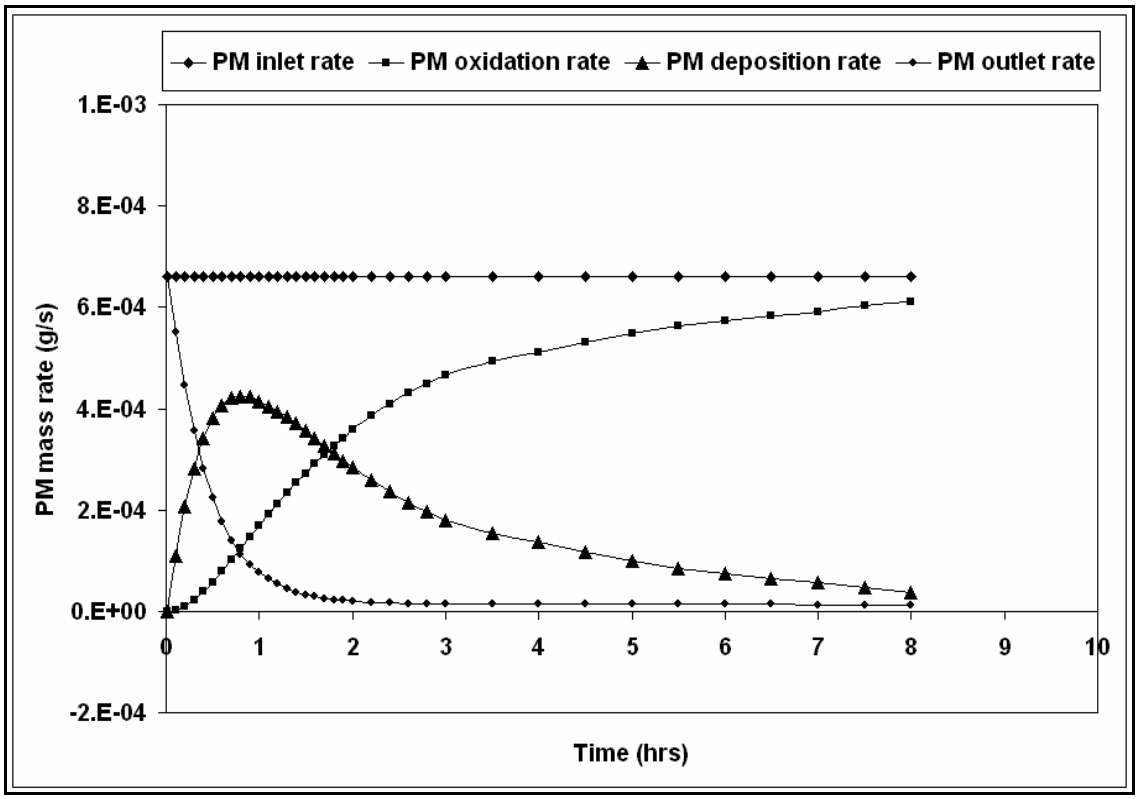

Figure 47: PM mass rates in the PM cake layer at 100% engine load case in the CPF configuration at 2200 rpm

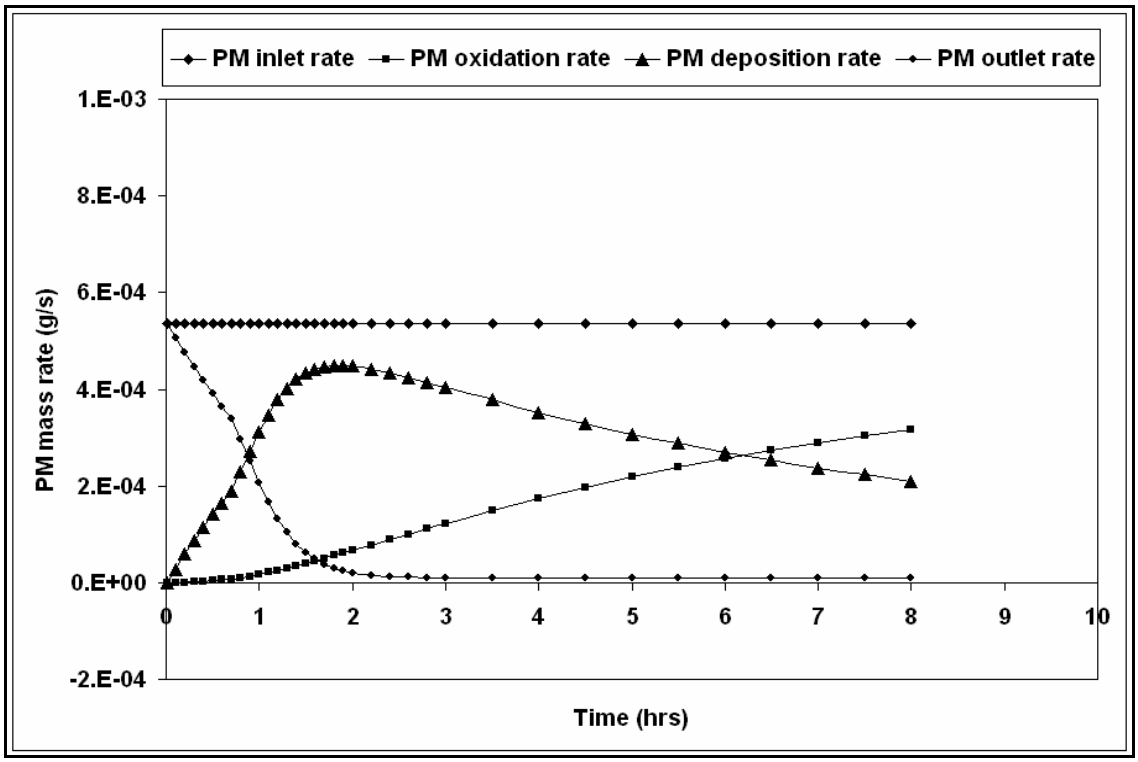

Figure 48: PM mass rates in the PM cake layer at 25% engine load case in the DOC+CPF configuration at 2200 rpm

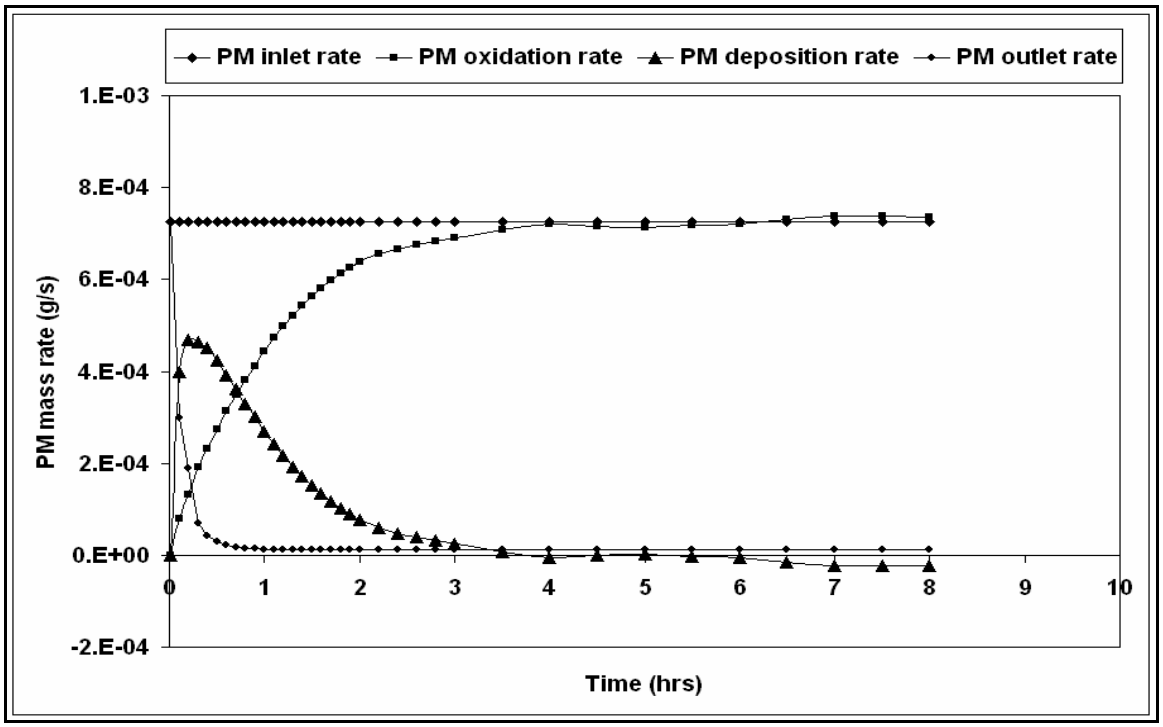

Figure 49: PM mass rates in the PM cake layer at 100% engine load case in the DOC+CPF configuration at 2200 rpm

Another new feature in the CPF model is the PM mass rate output. PM mass rates in the PM cake layer were obtained from a PM mass rate balance for the PM cake layer filter. Figure 46 thru Figure 49 show the PM mass rates in the PM cake layer for the 25 and 100% engine load cases in the CPF and DOC+CPF configurations. Similar plots for the 50% engine load case are shown in Figures 80 thru 83 in Appendix B. Since majority of PM oxidized is in the PM cake layer (as can be seen later in this section – Figure 59), a comparison of PM mass rates in the PM cake layer will facilitate better understanding of the oxidation process in the CPF.

PM inlet rates in the PM cake layer are the input values calculated from standard CPF inlet PM concentrations $\left(C_{in,std}\right)$ and standard exhaust volumetric flow rates $\left(\dot{V}_{std}\right)$, and were in the range of ($5.5\text{x}10^{-4}$ – $8.0\text{x}10^{-4}$). These values were constant because the input values of $C_{in,std}$ and $\dot{V}_{std}$ were average values (as given in Table 8).

PM oxidation rates in the PM cake layer were observed to be similar in trends in the CPF and DOC+CPF configurations at 25% engine load case, mainly because the NO_2/temperature assisted PM oxidation did not significantly increase the PM oxidation levels in the DOC+CPF configuration (although higher NO_2 concentrations were available for PM oxidation – *144 ppm* at UP-CPF location in the DOC+CPF configuration compared to *38 ppm* in the CPF configuration) due to overall exhaust temperatures being low (267°C in DOC+CPF compared to 250°C in CPF). This is reflected in the cumulative 'PM oxidized' curves as shown in Figure 42 and Figure 44. In the 100% engine load case, however, the difference in PM oxidation rates between CPF and DOC+CPF was more pronounced (as can be observed from comparing Figure 47 with Figure 49), mainly due to higher NO_2 concentrations in DOC+CPF (127 ppm in DOC+CPF compared to 27 ppm) at high UP-CPF exhaust temperatures (428°C in DOC+CPF and 405°C in CPF).

It was also observed that positive values of PM deposition rates always corresponded to growing PM cake layer (as can be seen from 25% engine load case in CPF configuration – refer Figure 46 and Figure 50), while negative values of PM deposition rates in the PM cake meant depleting PM cake layer (as was observed from 100% engine load case in DOC+CPF configuration - refer Figure 49 and Figure 53).

PM outlet rates in the PM cake layer always decreased from values equal to the PM inlet rates (since the PM cake was not present at initiation) to stabilize at a certain constant low value once the cake efficiency reached its maximum value, (as specified by the user input, A_η).

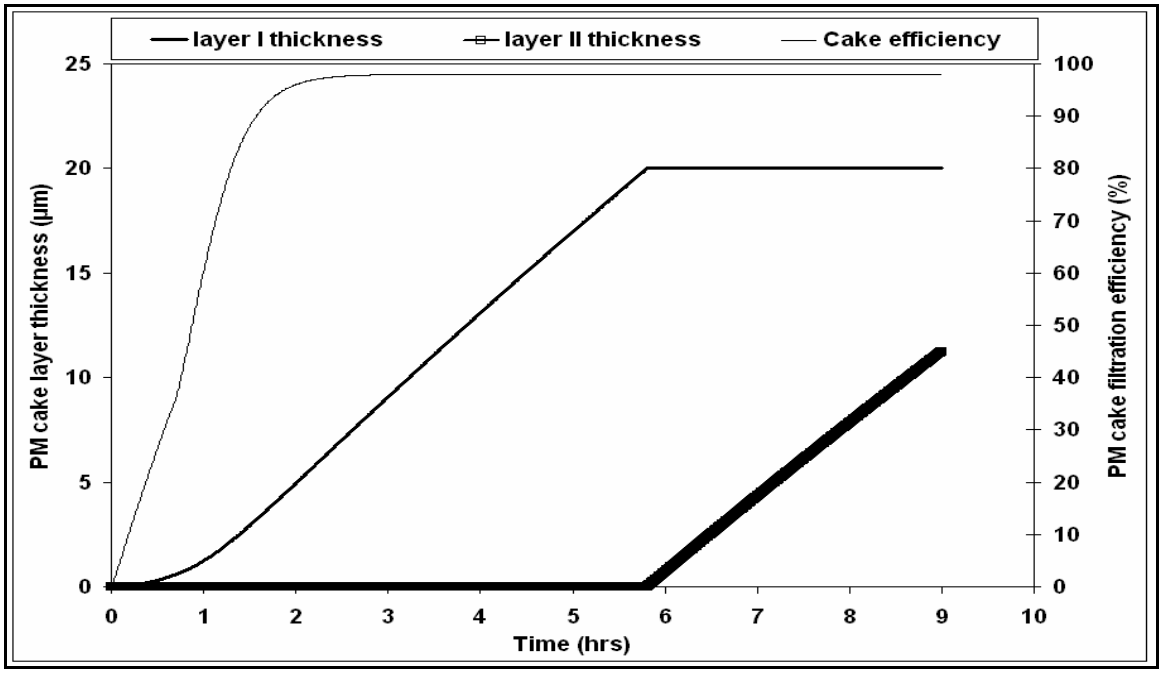

Figure 50: Thickness of *PM* cake layers I and II and *PM* cake layer efficiency in CPF configuration at 25% engine load case at 2200 rpm

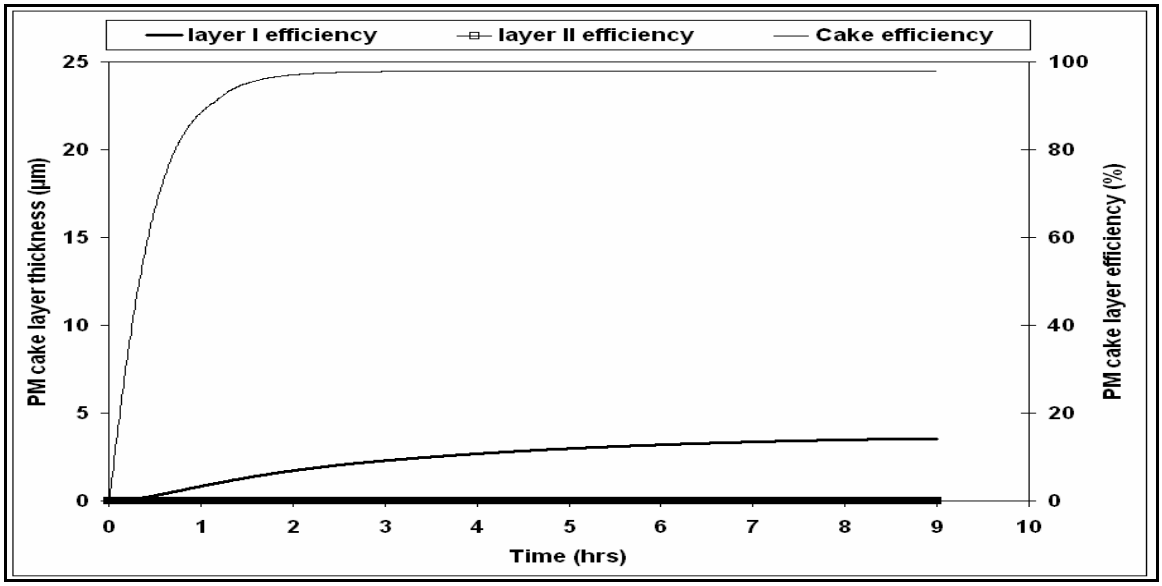

Figure 51: Thickness of *PM* cake layers I and II and *PM* cake layer efficiency in CPF configuration at 100% engine load case at 2200 rpm

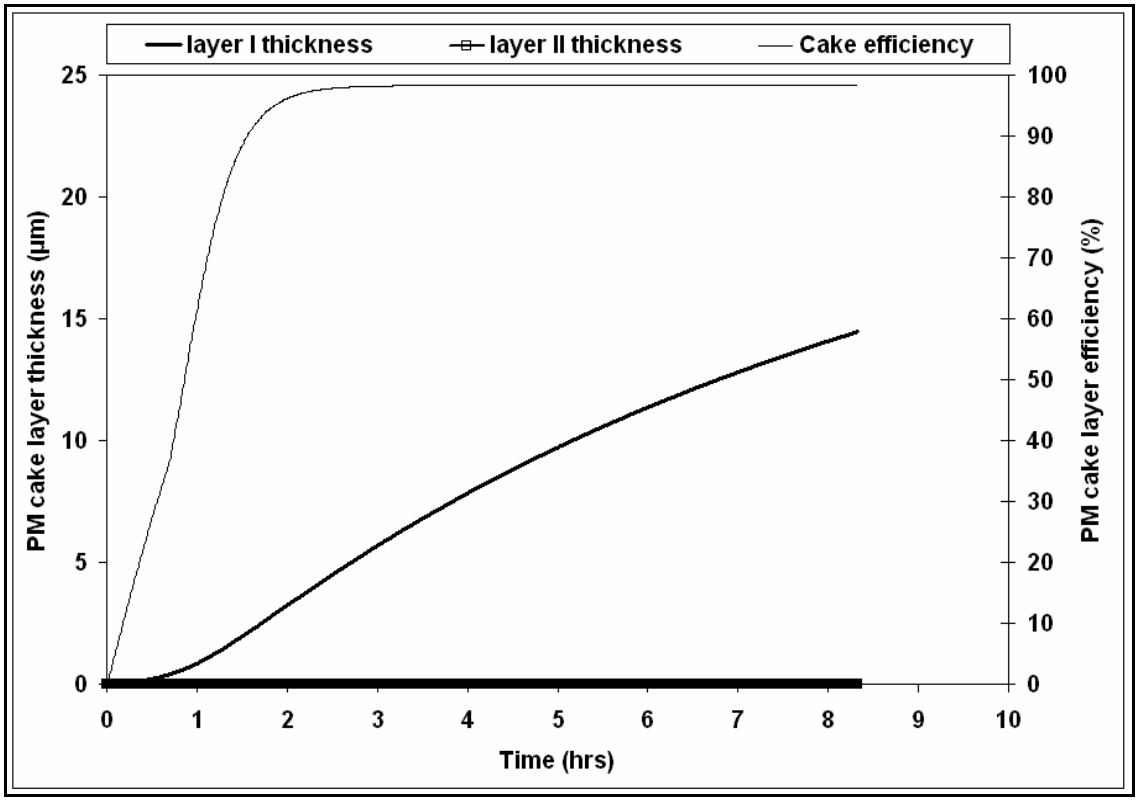

Figure 52: Thickness of *PM* cake layers I and II and *PM* cake layer efficiency in DOC+CPF configuration at 25% engine load case at 2200 rpm

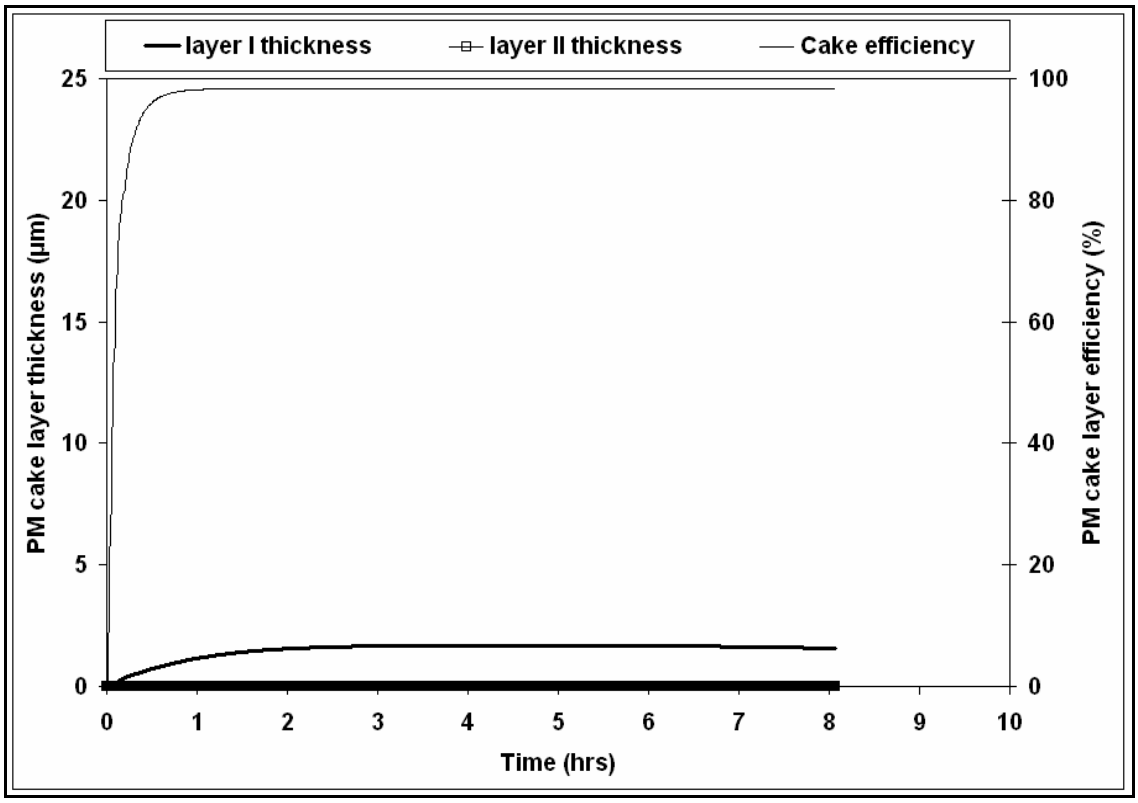

Figure 53: Thickness of *PM* cake layers I and II and *PM* cake layer efficiency in DOC+CPF configuration at 100% engine load case at 2200 rpm

In the CPF model, the *PM* cake layer is assumed to be in two layers – layer I, which is the layer in contact with the substrate wall directly (and hence with the catalyst wash-coat on the substrate wall), and layer II, which forms on top of layer I. For computational purposes, a certain maximum thickness of the *PM* cake layer is specified, beyond which layer II is assumed to form. A value of 20 μm was chosen (from reference [9]) for the calibration and analysis of the CPF model in all simulated load cases in this study. Figure 50 and Figure 51 show layer I and layer II thickness and corresponding *PM* cake efficiency curves from the calibrated CPF model at 25% and 100% engine load cases respectively in the CPF configuration at 2200 rpm, and Figure 52 and Figure 53 show the corresponding plots for the 25% and 100% engine load cases respectively, in the DOC+CPF configuration at 2200 rpm.

A 'vertical' comparison of *PM* cake layer thickness (Figure 50 vs. Figure 51 and Figure 52 vs. Figure 53) shows that the *PM* cake layer thickness in the 100% engine load cases were lower than that in the 25% engine load case in both configurations. This was due to higher *PM* oxidation rates in the *PM* cake layer (as seen from Figure 57) in the 100% compared to the 25% engine load, which was mainly due to higher exhaust temperatures and higher NO_2 flow rates with increasing engine loads. Layer II was not formed in any engine load case except in the CPF configuration at 25% engine load, where the *PM* oxidation rate was low enough to allow a *PM* cake layer thickness more than 20 µm.

Similarly, a 'horizontal' comparison of *PM* cake layer thickness showed that higher *PM* oxidation levels due to the presence of the DOC upstream of the CPF in the DOC+CPF configuration (which causes higher concentration of NO_2 to enter the CPF and oxidize the *PM*) caused lower *PM* cake layer thickness in comparable engine load cases. In the DOC+CPF configuration at 100% engine load case, (which showed higher *PM* oxidation rates, as is discussed later) the *PM* cake layer thickness was observed to be depleting after about 5 hours of loading time, due to the *PM* oxidation rate being higher than the *PM* deposition rate.

Figure 54 and Figure 55 show the *PM* cake layer and substrate wall filtration efficiency curves obtained from the calibrated CPF model at the 25% and 100% engine load cases in the CPF and DOC+CPF configurations. In all 4 cases, *PM* cake layer efficiencies grew to a maximum value in different amounts of loading time. The 100% engine load case in both configurations showed faster growth of *PM* cake layer efficiencies to their maximum values as compared to the 25% engine load case in both configurations.

On the other hand, substrate wall filtration efficiencies were generally lower at higher engine loads in both configurations. This can also be understood from oxidation levels in various load cases – higher oxidation rates in the substrate wall at higher engine loads (due to higher exhaust temperatures and higher NO_2 flow rates) translate to lower *PM* loadings in the substrate wall, which in turn translates to lower filtration efficiency values of the substrate wall, as shown in Figure 55.

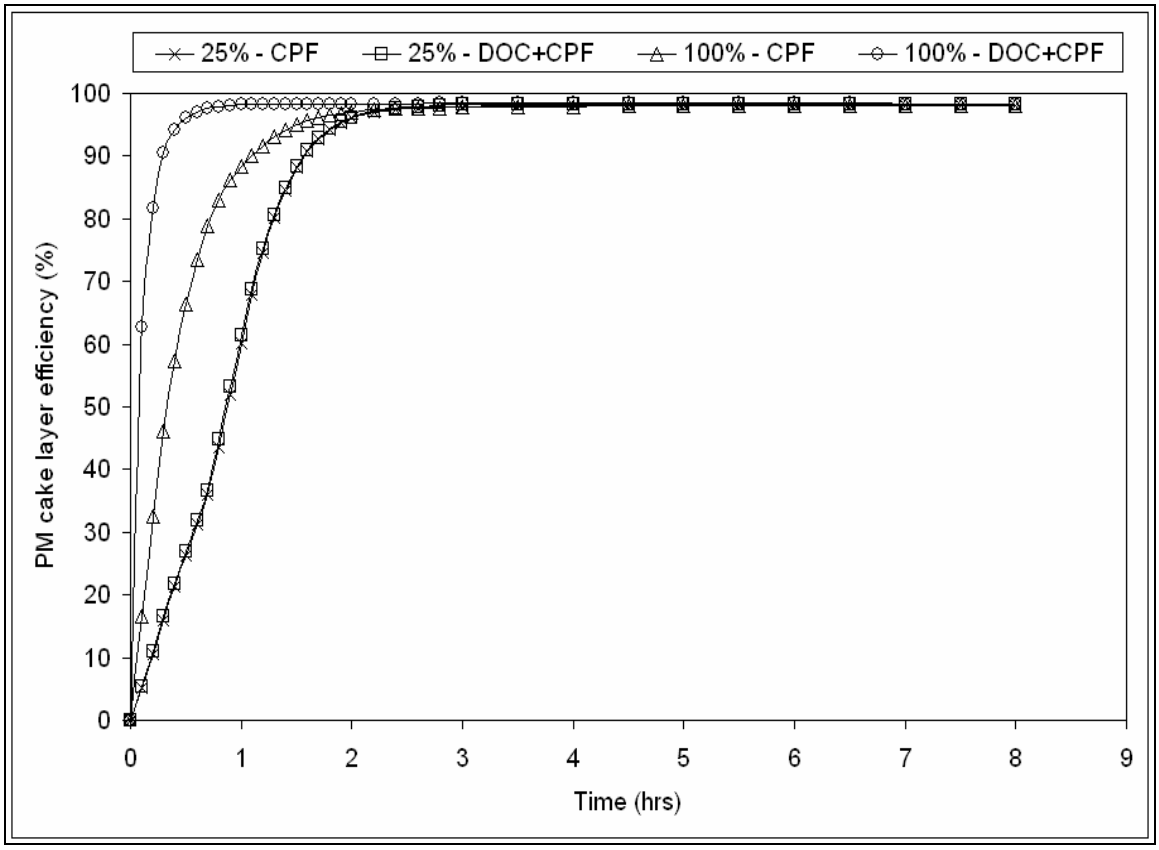

Figure 54: A comparison of *PM* cake filtration efficiency vs. loading time for the 25% and 100% engine load cases in CPF and DOC+CPF configurations at 2200 rpm

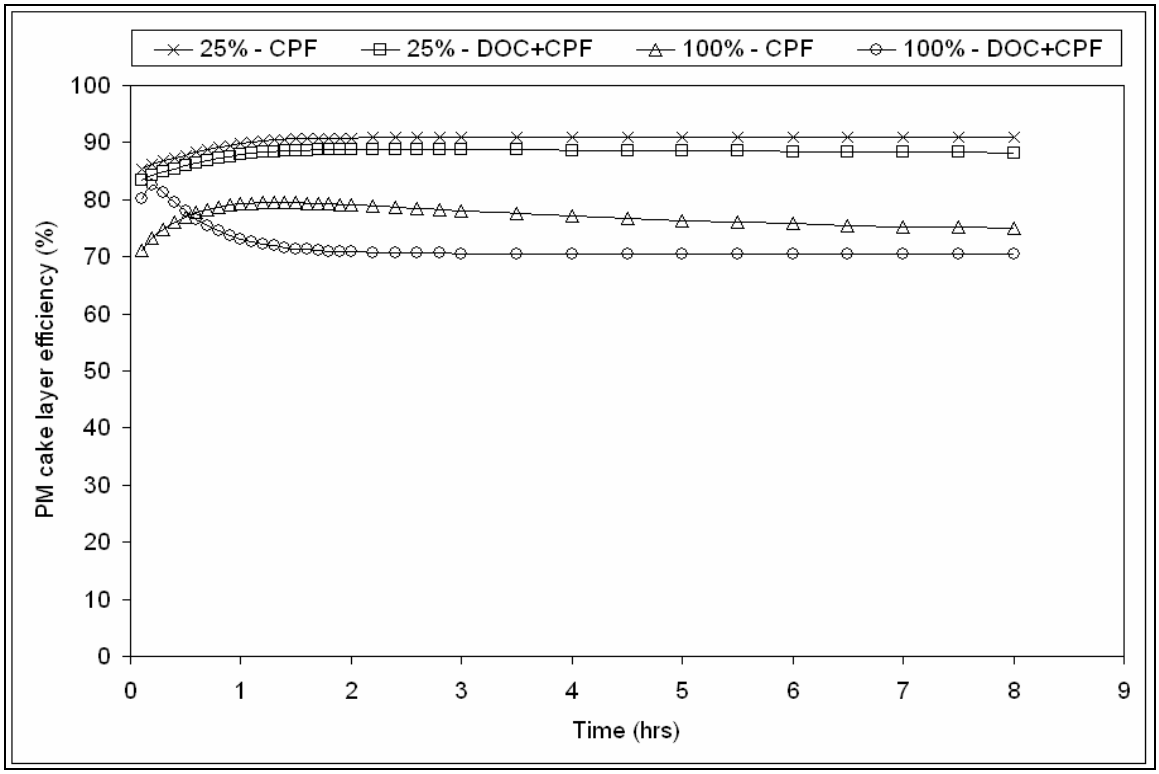

Figure 55: A comparison of substrate wall filtration efficiency vs. loading time for the 25% and 100% engine load cases in CPF and DOC+CPF configurations at 2200 rpm

Figure 56 shows the total *PM* oxidation rate and Figure 57 shows the *PM* oxidation rates in the *PM* cake layer and the substrate wall, for the 4 load cases studied. Figure 56 also shows the total *PM* inlet rates along with total *PM* oxidation rates, from which it can be concluded that as engine loads increased, overall *PM* oxidation rates increased and became comparable to *PM* inlet rates. In the 100% engine load case in the DOC+CPF configuration, for instance, the total *PM* oxidation rate became greater than the total *PM* inlet rate after about 5 hours of loading time (the effect of which can be observed from Figure 53 as a decrease in the *PM* cake layer thickness, as that is where majority of the *PM* oxidation takes place, as seen from Figure 59). *PM* oxidation rates in the substrate wall were lower than *PM* oxidation rate in *PM* cake layer by an order of magnitude, mainly due to low *PM* mass deposited in the wall compared to that in the *PM* cake.

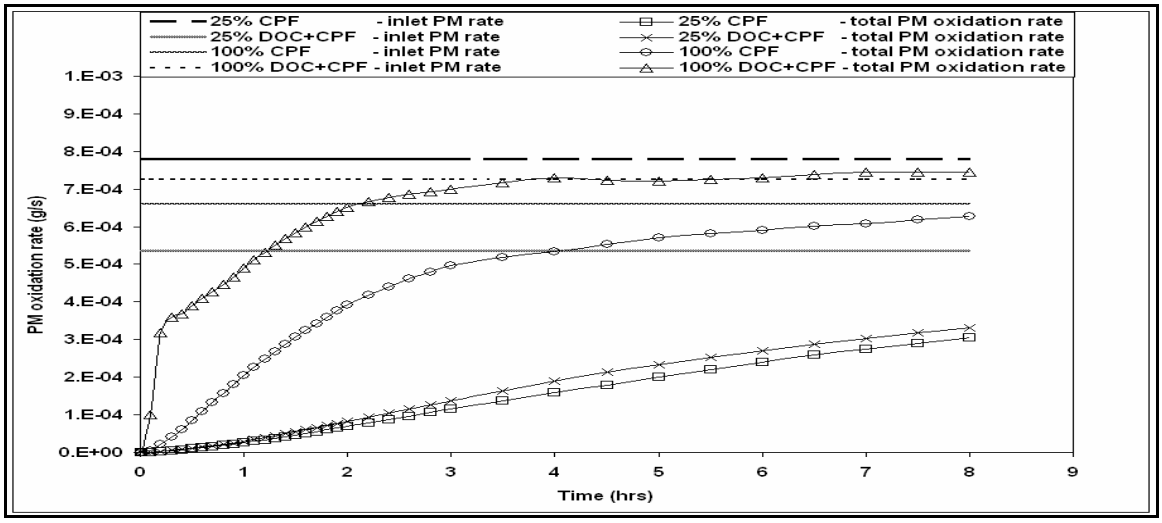

Figure 56: *PM* inlet rates and overall *PM* oxidation rates observed from the calibrated CPF model at 25% and 100% engine load cases in CPF and DOC+CPF configurations at 2200 rpm

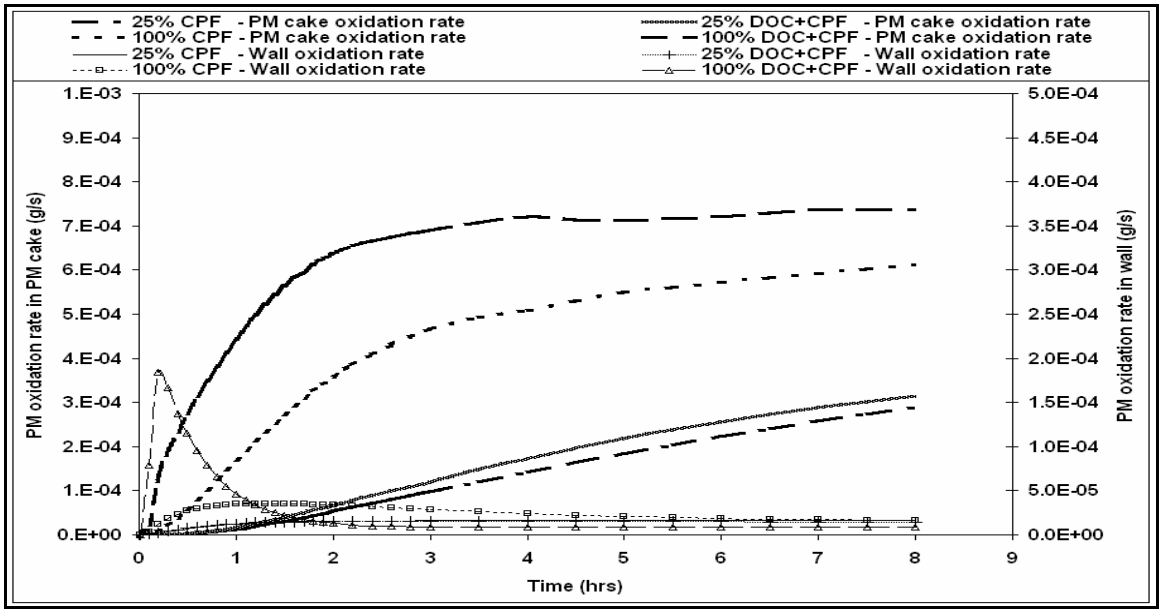

Figure 57: *PM* cake and substrate wall *PM* oxidation rates observed from the calibrated CPF model at 25% and 100% engine load cases in CPF and DOC+CPF configurations at 2200 rpm

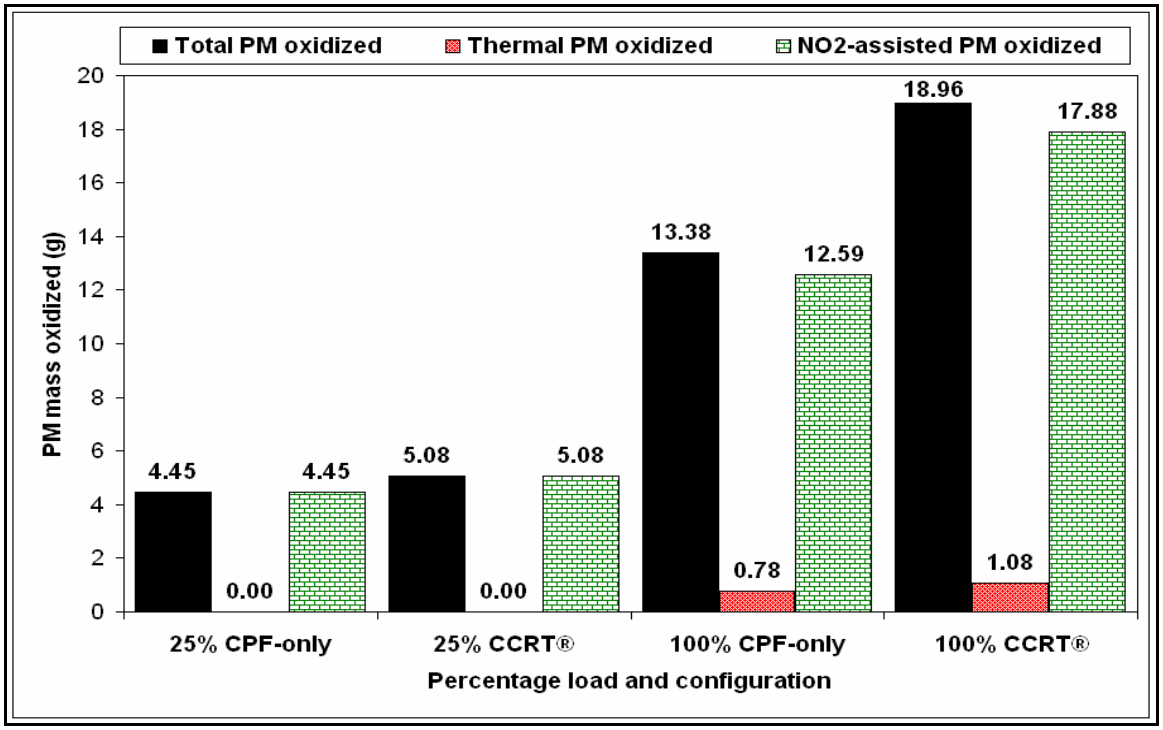

Figure 58: A comparison of *PM* mass oxidized by mechanism at 25% and 100% engine load cases in CPF and DOC+CPF configurations at 2200 rpm at 8 hours of loading time

A comparison of the total *PM* mass oxidized in the four cases analyzed as well as the distribution of *PM* mass oxidized according to the different mechanisms considered in the CPF model (namely, thermal and NO_2/temperature-assisted) at the same loading time (8 hours) is shown in Figure 58. The data shows that the DOC+CPF configuration had higher *PM* oxidation efficiency compared to the CPF configuration, and the majority of *PM* mass oxidized was via the NO_2/temperature-assisted mechanism. This reinforces the observations from previous research work (references [9 and 31]) that majority of *PM* mass oxidation at all engine load cases occurs due to the NO_2/temperature-assisted mechanism.

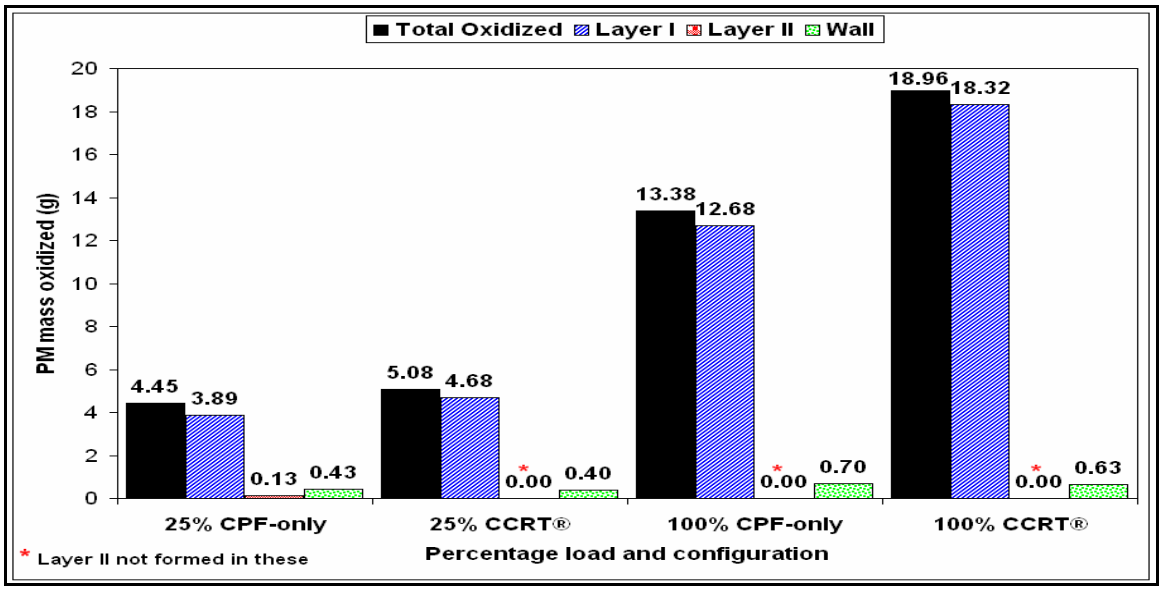

Figure 59: A comparison of *PM* mass oxidized by location at 25% and 100% engine load cases in CPF and DOC+CPF configurations at 2200 rpm at 8 hours of loading time

Figure 59 shows a distribution of the total *PM* oxidized by location (layer I and layer II of the *PM* cake layer and substrate wall), which points to the fact that total *PM* oxidized in the *PM* cake layers I and II (when layer II is present) are much higher than the *PM* oxidized in the wall. This is due to the *PM* cake filter forming a high efficiency (95-98%) filter and filtering out the majority of *PM* in the *PM* cake layer, due to which more *PM* is available for oxidation in the *PM* cake layer than in the substrate wall. Combining the observations from Figure 58 and Figure 59, it can be summarized that in all load cases compared in this study, majority of *PM* mass oxidized was in the *PM* cake layer via the NO_2/temperature-assisted mechanism, and that the DOC+CPF configuration is better than the CPF configuration in oxidizing *PM*, though during the initiation of loading, the pressure drop spikes observed at 100% engine load in the DOC+CPF configuration were higher than those observed in the CPF configuration.

4.3 Summary and Conclusions

Based on the experimental and model results presented and the analyses conducted on the experimental data and calibrated DOC and CPF model simulation results, the following can be summarized and conclusions drawn thereof:

1-D 2-LAYER CPF MODEL

The 1-D 2-layer CPF model was calibrated to experimental data at 8 engine load cases (4 engine loads and 2 configurations, CPF and DOC+CPF). From the simulation results obtained from the calibrated CPF model, the following conclusions can be made:

- CPF pressure drop in the 25% engine load case in both configurations had trends similar to the characteristic pressure drop profile observed in a DPF (uncatalyzed – references [23 and 31]), with an initial non-linear deep-bed filtration region for the first 2 hrs of loading time, followed by a transition region and a linear *PM* cake filtration region characterized by high *PM* cake (and hence) filtration efficiency. This was mainly due to low *PM* oxidation rates in the *PM* cake as well as in the substrate wall (as seen from Figure 57). At the end of loading, a 'loaded' substrate wall was observed in this engine load case.
- At higher engine loads in the CPF configuration, due to higher *PM* oxidation rates and similar *PM* inlet rates, pressure drop profiles always had a peak (refer Figure 30) and afterwards were found to be decreasing. The peak occurred at decreasing loading times as the engine load increased, indicating that the balance between *PM* oxidation rate and *PM* inlet rate was reached faster in the higher engine load cases, due to higher CPF inlet exhaust temperatures and NO_2 flow-rates.
- In the DOC+CPF configuration, the pressure drop profile at the 25% engine load case was similar to that in the same engine load in the CPF configuration, and as engine load increased, the peaks in pressure drop were reached faster than for same engine loads in the CPF configuration, due to higher NO_2/temperature-assisted (and hence, overall) *PM* oxidation rates, which was in turn due to the DOC present upstream of the CPF converting *NO* to NO_2 and providing the CPF with more NO_2 to oxidize *PM* with. In the 100% engine load case in the DOC+CPF configuration, the pressure drop was found to be reaching a 'steady' value of *7.2 kPa* after about *4 hours* of loading time, due to the balance between inlet *PM* rate, *PM* oxidation rate and *PM* outlet rate in the substrate wall (as seen from Figure 41). A 'clean' substrate wall was observed in this engine load case.

Regarding *PM* filtration and oxidation in the CPF, the following conclusions are presented:

- Majority of *PM* filtration and oxidation in the CPF at all engine load cases was carried out by the *PM* cake layer once it was formed.

- Percentage *PM* oxidized by the CPF increased with increasing engine load due to higher exhaust temperatures and higher NO_2 flow-rates as engine load increased.

- Percentage *PM* oxidized in the DOC+CPF configuration was higher than that in the CPF configuration for the same engine load, due to the conversion of *NO* to NO_2 in the DOC present upstream of the CPF in the DOC+CPF configuration.

From this study, the conclusions that can be arrived at about the filtration efficiency of the CPF are as follows:

- Overall CPF filtration efficiency was greater than 99%, primarily due to the *PM* cake layer formation which acts as an efficient filter (95-98% filtration efficiency of the *PM* cake was observed in all engine load cases) after it reaches a thickness of *0.6-2 μm*.

- Wall filtration efficiencies decreased with increasing engine loads due to increasing *PM* oxidation rates in the wall. However, this decrease did not affect the overall filtration efficiency due to the presence of a *PM* cake layer doing the majority of the filtration in all engine load cases.

Regarding NO_2 production and consumption in the CPF, the conclusions that can be drawn from this study (Reference [25]) and a comparison to trends observed from previous research work (References [9 and 31]) are as follows:

- NO_2 production was not observed in the CPF in any engine load case except the 100% engine load case in the CPF configuration, whereas considerable production of NO_2 and *PM* oxidation by the NO_2 generated was observed in the previous research work. This difference in NO_2 production behavior of the CPF between the two studies (References [25 and 31]) could be due to differences in catalyst loading levels between the CPF units used.

- The consumption of NO_2 observed in this study was more than that required for *PM* oxidation by NO_2 via the NO_2/temperature-assisted mechanism. Also, the total NO_x concentrations at all engine load cases at UP-DOC, UP-CPF and DN-CPF locations were conserved (to within *±2 ppm* of UP-DOC values). This means that in the CPF in this study, there was some amount of dissociation of NO_2 taking place, due to which NO_2 was being consumed to form *NO* and O_2.

- NO_2 consumption due to *PM* oxidation via the NO_2/temperature-assisted mechanism observed in this study were lower than the corresponding values for previous research, which is due to lower CPF inlet *PM* concentrations in this study (*2.5-6 mg/std.m*^{3} [25], which is in turn due to low engine-out PM emissions) compared to those in previous research (*11-24 mg/std.m*^{3} [9]).

From the results obtained from the calibrated CPF model, an efficient way of periodically cleaning the CPF (especially when the engine is operated at low engine loads for majority of its operation) is to employ an active regeneration strategy in the CPF system that will clean the PM cake partially and oxidize the PM in the substrate wall completely in order to maintain a *PM* cake layer thickness in the CPF of *0.6-2 μm* so as to maintain high CPF filtration efficiencies while keeping the engine back-pressure at acceptable levels.

Complete oxidation of the *PM* cake and the substrate wall will also result in periodic pressure drop 'spikes' due to periodic loading of the wall before the *PM* cake is formed.

1-D DOC MODEL

The 1-D DOC model was calibrated to experimental data at 2200 and 1650 rpm and kinetic parameters (pre-exponential factors and activation energies as given in Table 10) arrived at thus were used to predict the DN-DOC concentrations of *CO*, *HC*, *NO* and NO_2 at various engine load cases at 2200 rpm. The use of this single set of kinetic parameters resulted in model-predicted values of CO from -14 to +51%, HC's from -14 to +45%, NO from -30 to +35% and NO_2 from -9 to 17% of experimental values at 2200 rpm. In the 10-15% and 80-100% engine load range, considerable variation of model-predicted values of DN-DOC concentrations of all species (CO – 0 to 67%, HC – -15 to 132%, NO – 0 to 25%, and NO_2 – -21 to 4%) was observed, indicating that the model needs further improvement in the kinetics scheme used. In particular,

- NO_2 dissociation reaction has to be considered at all engine load conditions. The equilibrium constants for *NO* oxidation and NO_2 dissociation need to be included as functions of local DOC channel temperature.

- The expressions used for determining adsorption constants used in the DOC model need to be modified, since values of the same from published literature (reference [27]) were found out to be insufficient to accurately explain the kinetics in the DOC used in this study.

5. REFERENCES

[1] http://www.Dieselnet.com/news/

[2] Huynh, C.T., Johnson, J.H., Yang, S.L., Bagley, S.T., and Warner, J.R. *A One-Dimensional Computational Model for Studying the Filtration and Regeneration Characteristics of a Catalyzed Wall-Flow Diesel Particulate Filter*. SAE Paper No. 2003-01-0841. (2003)

[3] Huynh C. T., *"A Study of the Filtration and Regeneration Characteristics of A Catalyzed Wall-Flow Diesel Particulate Filter: One-Dimensional Model Calibrated and Validated with Experimental Data"*, MS Thesis, Michigan Technological University, Houghton, MI, 2002.

[4] Konstandopoulos, Athanasios G., and Kostoglou, Margaritis. *Periodically Reversed Flow Regeneration of Diesel Particulate Traps*. SAE Paper No. 1999-01-0469. (1999)

[5] Bissett, Edward J. *Mathematical Model of the Thermal Regeneration of a Wall-Flow Monolith Diesel Particulate Filter*. Chemical Engineering Science Vol. 39, Nos. 7/8 pp. 1233-1244 (1984)

[6] Konstandopoulos, Athanasios G. and Johnson, John H. *Wall-Flow Diesel Particulate Filters – Their Pressure Drop and Collection Efficiency*. SAE Paper No. 890405. (1989)

[7] Konstandopoulos, A.G., Kostoglou, M., Skaperdas, E., Papaioannou, E., Zarvalis, D. and Kladopoulou, E. *Fundamental Studies of Diesel Particulate Filters: Transient Loading, Regeneration and Aging*. SAE Paper No. 2000-01-1016. (2000)

[8] Murphy, M.J.; Hillenbrand, L.J.; and Trayser, D.A. *Assessment of diesel particulate control – direct and catalytic oxidation*. SAE Paper No. 810112. (1981)

[9] Hasan M. *"The Filtration and Oxidation Characteristics of a Diesel Oxidation Catalyst and a Catalyzed Particulate Filter: Development of a 1-D 2-Layer Model."*, M.S. Thesis, Michigan Technological University, Houghton, MI, 2005

[10] Davies C.N. *Air Filtration*. Academic Press Inc. 1973.

[11] Davies C.N. *Aerosol Science*. Academic Press Inc. 1966.

[12] Konstandopoulos, A.G., Skaperdas, E., Warren, J. and Allanson, R. *Optimized Filter Design and Selection Criteria for Continuously Regenerating Diesel Particulate Traps*. SAE Paper No. 1999-01-0468. (1999)

[13] Koltsakis G.C. and Stamelos A.M., *"Modes of Catalytic Regeneration in Diesel Particulate Filters."* Ind. Eng. Chem. Res. 36, pp. 4155-4165, 1997.

[14] Koltsakis G.C. and Stamelos A.M., *"Modeling Catalytic Regeneration of Wall-Flow Particulate Filters."* Ind. Eng. Chem. Res. 35, pp. 2-13, 1996.

[15] Triana, P. A., Johnson J.H., Yang, S.L., and Baumgard K.J. *An Experimental and Numerical Study of the Performance Characteristics of the Diesel Oxidation Catalyst in a Continuously Regenerating Diesel Particulate Filter*. SAE Paper No. 2003-01-3176. (2003)

[16] Konstandopoulos, A.G., Skaperdas, E., Masoudi, M. *Microstructural Properties of Soot Deposits in Diesel Particulate Traps*. SAE Paper No. 2002-01-1015. (2002)

[17] Ranalli, M., Hossfeld, C. Kaiser, R., Schmidt, S., and Elfinger, G. 2004. "*Soot Loading Distribution as a Key Factor for a Reliable System: an Innovative Development Methodology*", SAE 2002-01-2158

[18] Maly, M., Claussen, M., Carlowitz, O., Kroner, P., Ranalli, M., and Schmidt, S., 2004. "*Influence of the Nitrogen Dioxide Based Regeneration on Soot Distribution*", SAE 2004-01-0823

[19] Allansson, R., Blakeman, P.G., Cooper, B.J., Hess, H., Silcock, P.J., Walker, A.P., 2002. "*Optimizing the Low Temperature Performance and Regeneration Efficiency of the Continuously Regenerating Diesel Particulate Filter (CR-DPF) System*", SAE 2002-01-0428

[20] DECSE 2000a. "*Phase I Interim Data Report No. 4: Diesel Particulate Filters*", U.S. DOE, January 2000.
[21] http://www.Dieselnet.com. *CRT Filter*. (2002) & (2004)
[22] Konstandopoulos, A. G., and Kostoglou, M. *Microstructural Aspects of Soot Oxidation*. SAE Paper No. 2004-01-0693. (2004)
[23] Hasan M., Triana A., Johnson J., and Yang S. "*An Advanced 1D 2-Layer Catalyzed Diesel Particulate Filter Model to Simulate: Filtration by the Wall and Particulate Cake, Oxidation in the Wall and Particulate Cake by NO_2 and O_2 and Heat Addition*", SAE 2006-01-0467
[24] Dieselnet online resource. http://www.dieselnet.com/standards/us/offroad.html . Accessed Jan. 2005.
[25] K.C.Premchand. "An Experimental and Modeling Study of the Filtration and Oxidation Characteristics of a Diesel Oxidation Catalyst and a Catalyzed Particulate Filter," Master's thesis, Michigan Technological University, 2006.
[26] H.Oh and J.C.Cavendish. "Transients of Monolithic Catalytic Converters: Response to Step Changes in Feedstream Temperature as Related to Controlling Automobile Emissions," Ind. Eng. Chem. Prod. Res. Dev., 21:29–37, 1982.
[27] G.C.Koltsakis, O.A.Haralampous, C.K.Dardiotis, Z.C.Samaras, C.D.Vogt, E.Ohara, Y.Watanabe, and T.Mizutani. "Performance of Catalyzed Particulate Filters without Upstream Oxidation Catalyst," SAE 2005-01-0952, 2005.
[28] A.P.Triana. "Development of Models to Study the Emissions, Flow and Kinetic Characteristics from Diesel Oxidation Catalysts and Particulate Filters," PhD thesis, Michigan Technological University, 2005.
[29] P.M.Laing, M.D.Shane, Son, Seha, A.A.Adamczyk, and P.Li. "A Simplified Approach to Modeling Exhaust System Emissions – SIMTWC," SAE 1999-01-3476, 1999.
[30] A.S.Shende, J.H.Johnson, S.L.Yang, S.T.Bagley, and A.M.Thalagavara. "The Filtration and Particulate Matter Oxidation Characteristics of a Catalyzed Wall-Flow Diesel Particulate Filter," SAE 2005-01-0949, 2005.
[31] H.Mohammed, V.R.Lakkireddy, J.H.Johnson, and S.T.Bagley. "An Experimental and Modeling Study of a Diesel Oxidation Catalyst and a Catalyzed Particulate Filter Using a 1-D 2-Layer Model," SAE 2006-01-0466, 2006.
[32] B.R.Bird, W.E.Stewart, and E.N.Lightfoot. "Transport Phenomena," John Wiley and Sons, 1960.

6.0 APPENDIX

6.1 APPENDIX A

DOC MODEL - GOVERNING EQUATIONS

PRESSURE DROP MODEL

The pressure drop across the DOC is obtained by solving for axial momentum conservation and mass conservation, assuming fully developed laminar flow through a channel with a square channel. DOC pressure drop is given by:

$$\Delta P = \frac{1}{\varepsilon}\frac{2\mu_g K L \dot{V}}{(CFA) D_h^2} \tag{A.1}$$

where K can be expressed as:

$$K = (\mathrm{Re}_g)(C_f) \tag{A.2}$$

CFA is simply the converter frontal area given by:

$$CFA = \pi \frac{D^2}{4} \tag{A.3}$$

C_f is the skin friction coefficient given as:

$$C_f = \frac{\tau_{wall}}{\left(\frac{1}{2}\rho_g u^2\right)} \tag{A.4}$$

and:

$$D_h = \frac{1}{\sqrt{\sigma}}\left(1 - w_t\sqrt{\sigma}\right) \tag{A.5}$$

MASS AND ENERGY BALANCE IN THE GAS-PHASE

The conservation of mass for the single channel can be expressed as:

$$\frac{\partial \rho_g}{\partial t} + \frac{\partial(\rho_g u)}{\partial x} = 0 \tag{A.6}$$

At steady state, (A.1) reduces to:

$$\frac{\partial(\rho_g u)}{\partial x} = 0 \tag{A.7}$$

For a 1-D bulk flow model, velocity of exhaust gas (u) can be expressed simply as:

$$u = \frac{\dot{V}}{\varepsilon\left(\frac{\pi D^2}{4}\right)} \tag{A.8}$$

where ε can be expressed as:

$$\varepsilon = \left(1 - w_t\sqrt{\sigma}\right)^2 \tag{A.9}$$

Conservation of energy for the exhaust gas in the channel is given as:

$$\frac{\partial T_g}{\partial t} = -u\frac{\partial T_g}{\partial x} + \frac{Gah_g}{\varepsilon\rho_g c_{pg}}\left(T_w - T_g\right) + \frac{Sp}{\varepsilon\rho_g c_{pg}}\sum_{i=1}^{3} -\Delta H_i R_i \tag{A.10}$$

where:

$$Ga = 4\left(1 - w_t\sqrt{\sigma}\right)\sqrt{\sigma} \tag{A.11}$$

and:

$$Sp = \rho_{soot} A_{soot} \tag{A.12}$$

h_g is obtained from Re_g, Pr_g and Nu_g as per the following relations:

$$h_g = \frac{Nu_g \lambda_g}{D_h} \tag{A.13}$$

$$Nu_g = 2.709\left(\mathrm{Re}_g\ \mathrm{Pr}_g\right)^{0.179} \tag{A.14}$$

$$\mathrm{Re}_g = \frac{\dot{m} D_h}{\varepsilon(CFA)\mu_g} \tag{A.15}$$

c_{pg}, μ_g and λ_g are expressed as functions of absolute temperature of exhaust gas [25] as:

$$c_{pg} = 962.097 + 0.1507T_g \tag{A.16}$$

$$\mu_g = \left(0.00268T_g + 1.384\right)\left(1x10^5\right) \tag{A.17}$$

$$\lambda_g = \left(8.459x10^{-3}\right) + \left(5.7x10^{-5}T_g\right) \tag{A.18}$$

The heat source term in Equation (A.10) $\left(\sum_{i=1}^{3} -\Delta H_i R_i\right)$ is the summation of heat release due to:

1. *NO_2*/temperature-assisted *PM* oxidation,
2. Thermal *PM* oxidation, and
3. Catalytic *PM* oxidation.

$$\begin{aligned}\sum_{i=1}^{3} -\Delta H_i R_i &= \left(-\Delta H_{NO_2} R_{NO_2}\right) \\ &+ \left(-\Delta H_{th} R_{th}\right) + \left(-\Delta H_{cat} R_{cat}\right)\end{aligned} \tag{A.19}$$

where the heating values of combustion for the 3 reactions are given as:

$$(-\Delta H)_{NO_2} = (g_{CO})(\Delta h_f^0)_{CO} + (1-g_{CO})(\Delta h_f^0)_{CO_2} + (2-g_{CO})(\Delta h_f^0)_{NO} + (2-g_{CO})(\Delta h_f^0)_{NO_2} \quad \text{(A.20)}$$

$$(-\Delta H)_{th} = (f_{CO}^{thermal})(\Delta h_f^0)_{CO} + (1-f_{CO}^{thermal})(\Delta h_f^0)_{CO_2} \quad \text{(A.21)}$$

$$(-\Delta H)_{cat} = (f_{CO}^{catalytic})(\Delta h_f^0)_{CO} + (1-f_{CO}^{catalytic})(\Delta h_f^0)_{CO_2} \quad \text{(A.22)}$$

For quasi-steady state, Equation (A.10) reduces to:

$$\frac{\partial T_g}{\partial x} = \left(\frac{Ga}{\varepsilon \rho_g c_{pg} u}\right) h_g (T_w - T_g) + \left(\frac{Sp}{\varepsilon \rho_g c_{pg} u}\right)\left(\sum_{i=1}^{3}(-\Delta H_i) R_i\right) \quad \text{(A.23)}$$

The system of equations representing individual species conservation in the gas-phase can be expressed as:

$$\frac{\partial c_{g,j}}{\partial t} = -u\frac{\partial c_{g,j}}{\partial x} - \left(\frac{Ga.k_{m,j}}{\varepsilon}\right)(c_{g,j} - c_{s,j}) + \left(\frac{Sp}{\varepsilon}\right)\left(\sum_{i=1}^{3}\zeta_i R_i\right) \quad \text{(A.24)}$$

Here, j is the number of species considered in the DOC model, which in this study is equal to 8. So, the species conservation equation system is actually a system of 8 individual equations.

For quasi-steady state, the unsteady term can be dropped from Equation (A.24) and the resulting equation system is:

$$\frac{\partial c_{g,j}}{\partial x} = \left(\frac{Ga.k_{m,j}}{\varepsilon u}\right)(c_{s,j} - c_{g,j}) + \left(\frac{Sp}{\varepsilon u}\right)\left(\sum_{i=1}^{3}\zeta_i R_i\right) \quad \text{(A.25)}$$

MASS AND ENERGY BALANCE IN THE SOLID-PHASE

The species conservation in the solid-phase is based on the balance between the rate of transport of individual species of the exhaust gas mixture from the gas-phase to the substrate wall (solid-phase) and the rate of disappearance of the particular species due to wall reaction (and these reactions are assumed to take place at the local wall temperature). Convection of species in the solid-phase is not assumed to be occurring. Mathematically,

$$\frac{\partial c_{s,j}}{\partial t} = -\frac{Ga.k_{m,j}}{(1-\varepsilon)}(c_{s,j} - c_{g,j}) - \frac{G_{ca} R_j}{(1-\varepsilon)} \quad \text{(A.26)}$$

where G_{ca} is approximated as equal to G_a. For quasi-steady state, Equation (A.26) reduces to:

$$k_{m,j}(c_{s,j} - c_{g,j}) = -R_j \quad \text{(A.27)}$$

The wall energy balance equation can be written as:

$$\frac{\partial T_w}{\partial t} = -\frac{Ga\,.h_g}{(1-\varepsilon)\rho_w c_{pw}}(T_w - T_g) - \frac{S_{ext}\,h_\infty}{(1-\varepsilon)\rho_w c_{pw}}(T_w - T_\infty) + \frac{\lambda_w}{\rho_w c_{pw}}\frac{\partial^2 T_w}{\partial x^2} + \frac{G_{ca}}{(1-\varepsilon)\rho_w c_{pw}}\sum_{j=1}^{n}(-\Delta H_j)R_j \quad \text{(A.28)}$$

where:

$$S_{ext} = \frac{\pi D_{can}}{\left(\frac{\pi D_{can}^2}{4}\right)} = \frac{4}{D_{can}} \quad \text{(A.29)}$$

and c_{pw} and λ_w are treated as functions of absolute substrate wall temperature [28] as:

$$c_{pw} = 1071 + 0.156T_w - \frac{3.435x10^7}{T_w^2} \quad \text{(A.30)}$$

$$\lambda_w = 3x10^{-6}T_w^2 - 0.0037T_w + 2.0553 \quad \text{(A.31)}$$

h_∞ is obtained from the following relation:

$$h_\infty = h_{amb}\frac{Nu_\infty \lambda_\infty}{D_{can}} \quad \text{(A.32)}$$

Nu_∞ and λ_∞ are calculated from the following relations:

$$Nu_\infty = 0.53(Gr_\infty \Pr_\infty)^{0.25} \quad \text{(A.33)}$$

$$Gr_\infty = \frac{g(T_w - T_\infty)D_{can}^3 \lambda_\infty}{T_\infty \mu_\infty^2} \quad \text{(A.34)}$$

$$\Pr_\infty = \frac{\mu_\infty c_{p\infty}}{\lambda_\infty} \quad \text{(A.35)}$$

$$c_{p\infty} = c_{pg}(T_\infty) \quad \text{(A.36)}$$

$$\mu_\infty = \mu_g(T_\infty) \quad \text{(A.37)}$$

$$\lambda_\infty = \lambda_g(T_\infty) \quad \text{(A.38)}$$

In Equation (A.28), the 'heat release due to chemical reactions' term includes all 5 reactions considered in this study. So, $n = 5$. Mathematically,

$$\sum_{j=1}^{5}(-\Delta H_j)R_j = (-\Delta H_{CO})R_{CO} + (-\Delta H_{NO})R_{NO} + (-\Delta H_{C_3H_6})R_{C_3H_6} + (-\Delta H_{CH_4})R_{CH_4} + (-\Delta H_{C_{16}H_{34}})R_{C_{16}H_{34}} \quad \text{(A.39)}$$

Mass transfer coefficients $k_{m,j}$ are calculated from the following relations given in reference [28]:

$$k_{m,j} = \frac{Sh_{\infty} Dm_j}{D_h}\left(1x10^{-4}\right) \tag{A.40}$$

$$Dm_j = \frac{\left(1 - Y_j\right)}{\sum_{\substack{i=1 \\ i \neq j}}^{8}\left(\frac{Y_i}{D_{ji}}\right)} \tag{A.41}$$

$$D_{ji} = C_{ji}\frac{T^B}{P}\left(1x10^5\right) \tag{A.42}$$

$$C_{ji} = A\left(P_{c,j}P_{c,i}\right)^{\frac{1}{3}}\left(4.64x10^{-4}\right) \left(T_{c,j}T_{c,i}\right)^{\frac{5}{12}-\frac{B}{2}}\left(\frac{1}{MW_j}+\frac{1}{MW_i}\right)^{\frac{1}{2}} \tag{A.43}$$

where A and B are constants and $A = 2.745x10^{-4}$ and $B = 1.823$ for non-polar gas pairs, and $B = 2.334$ for H_2O with a non-polar gas [32].

6.2 APPENDIX B

ADDITIONAL DATA FROM THE CALIBRATED 1-D DOC MODEL

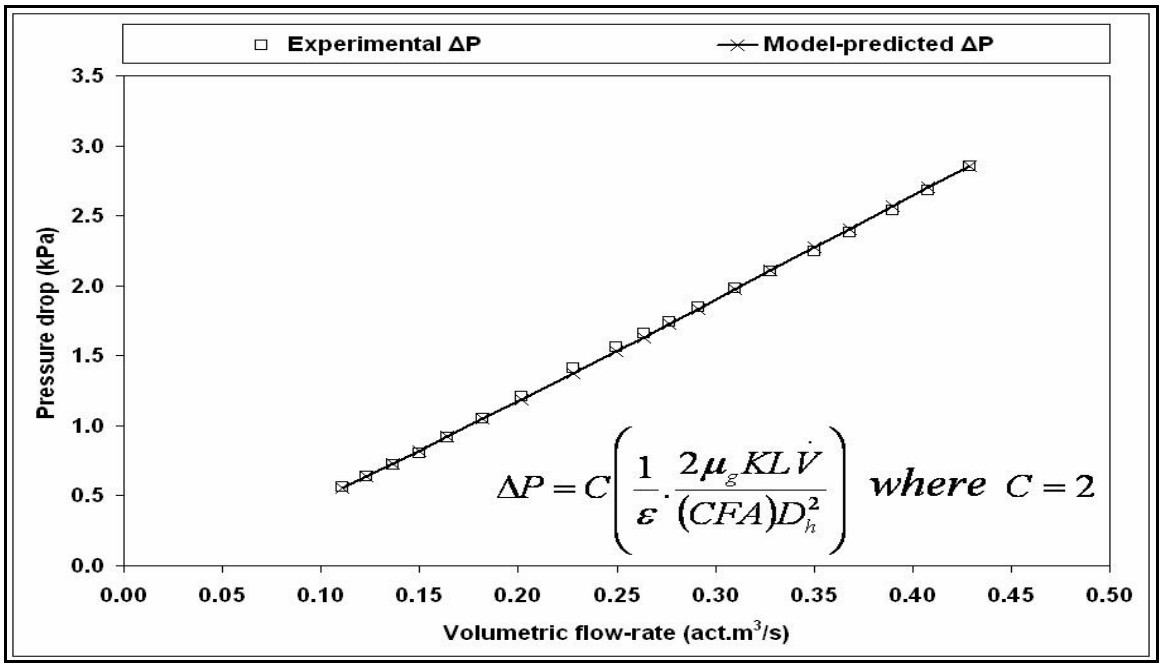

Figure 60: Experimental and model-predicted DOC pressure drop from DOC model calibrated to experimental data at 1650 rpm

An important step in DOC model simulations was to calibrate the DOC model to predict DN-DOC concentrations of *CO*, *HC*, *NO* and NO_2 accurately at both the engine speeds (1650 and 2200 rpm) for which experiments were carried out. The results obtained from the DOC model calibrated to *CO*, *HC*, *NO* and NO_2 concentration data at 1650 rpm are shown in Figure 61, Figure 62, Figure 63 and Figure 64 respectively.

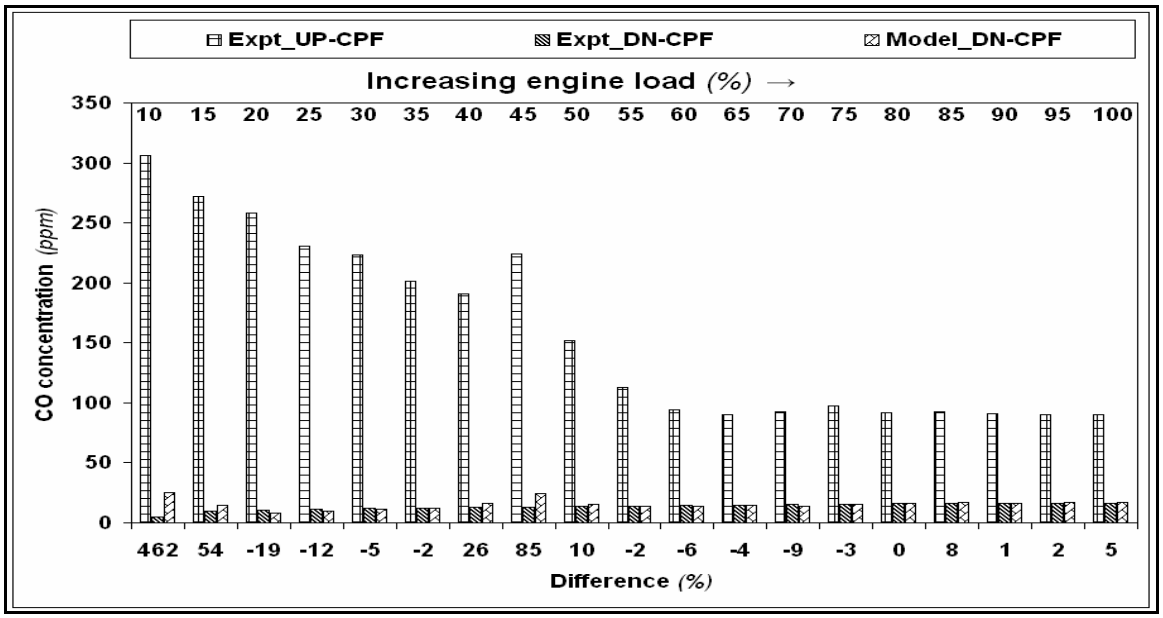

Figure 61: Experimental DOC inlet and outlet *CO* concentrations compared with model-predicted DOC outlet *CO* concentrations at 1650 rpm

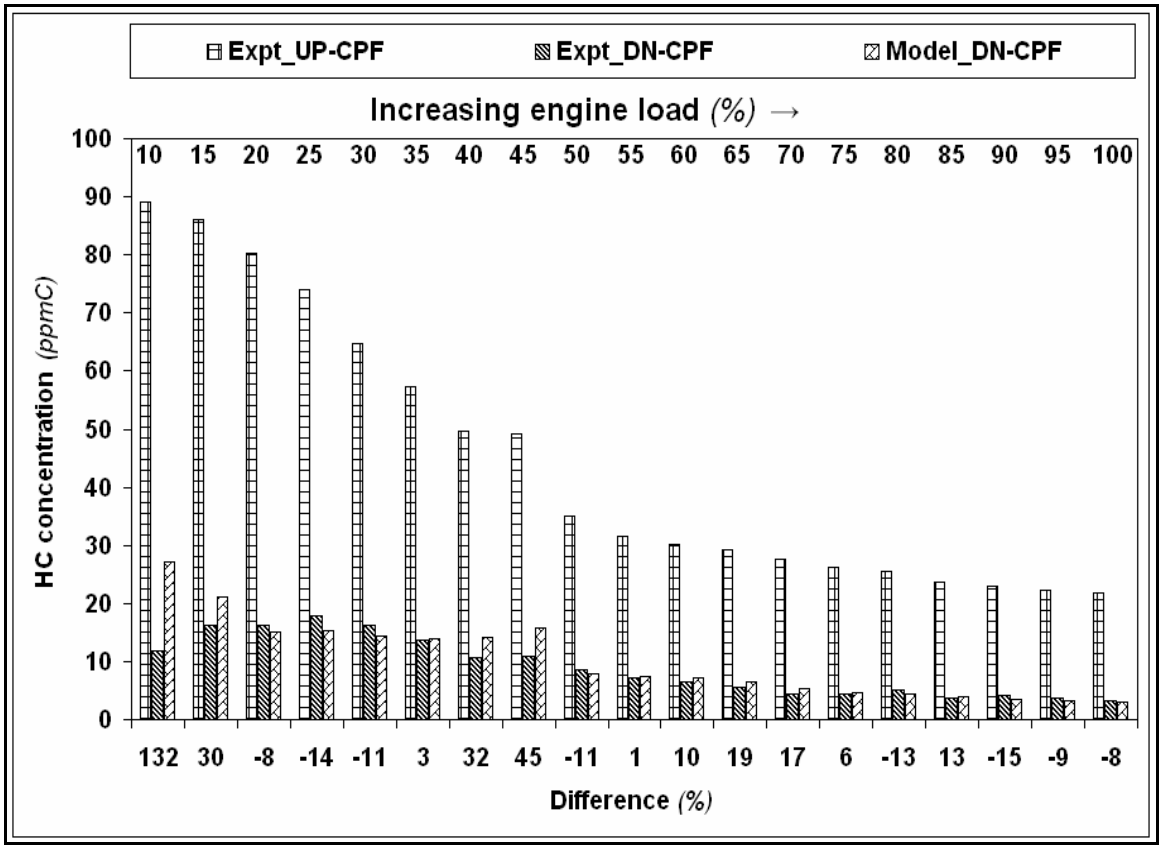

Figure 62: Experimental DOC inlet and outlet *HC* concentrations compared to model-predicted DOC outlet *HC* concentrations at 1650 rpm

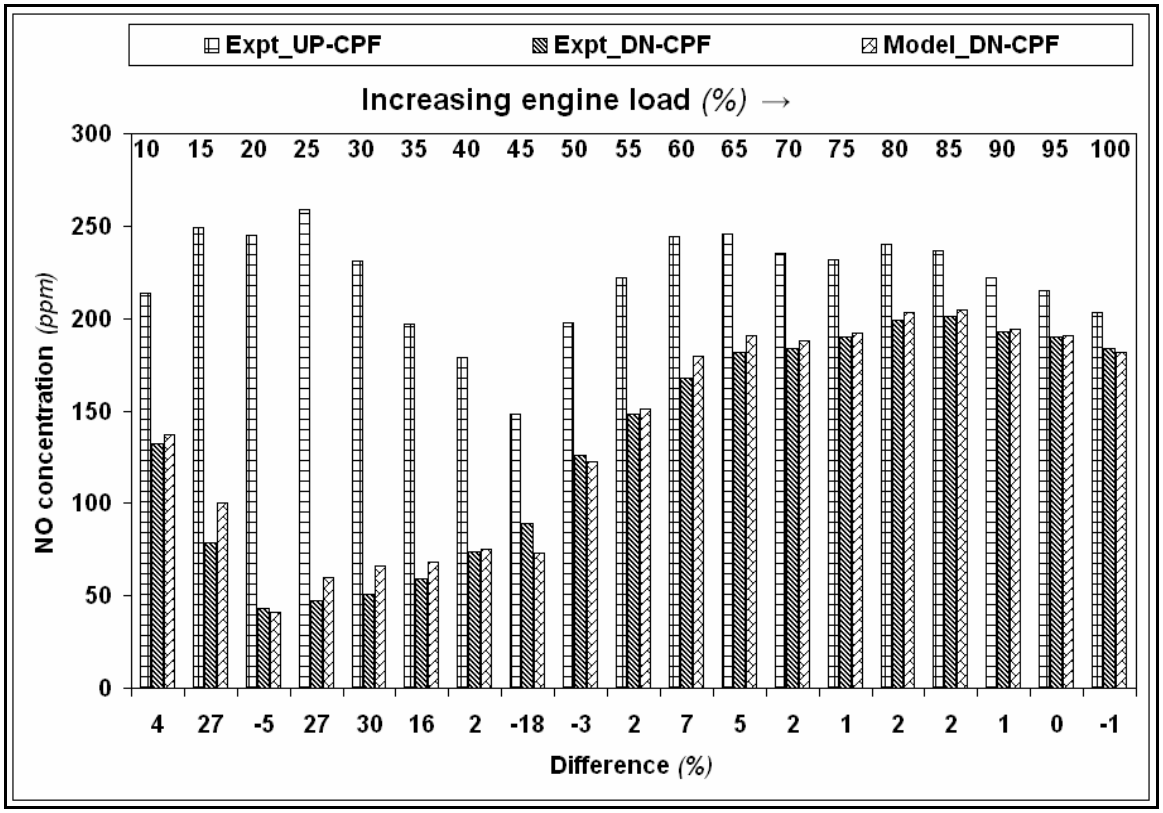

Figure 63: Experimental DOC inlet and outlet *NO* concentrations compared to model-predicted DOC outlet *NO* concentrations at 1650 rpm

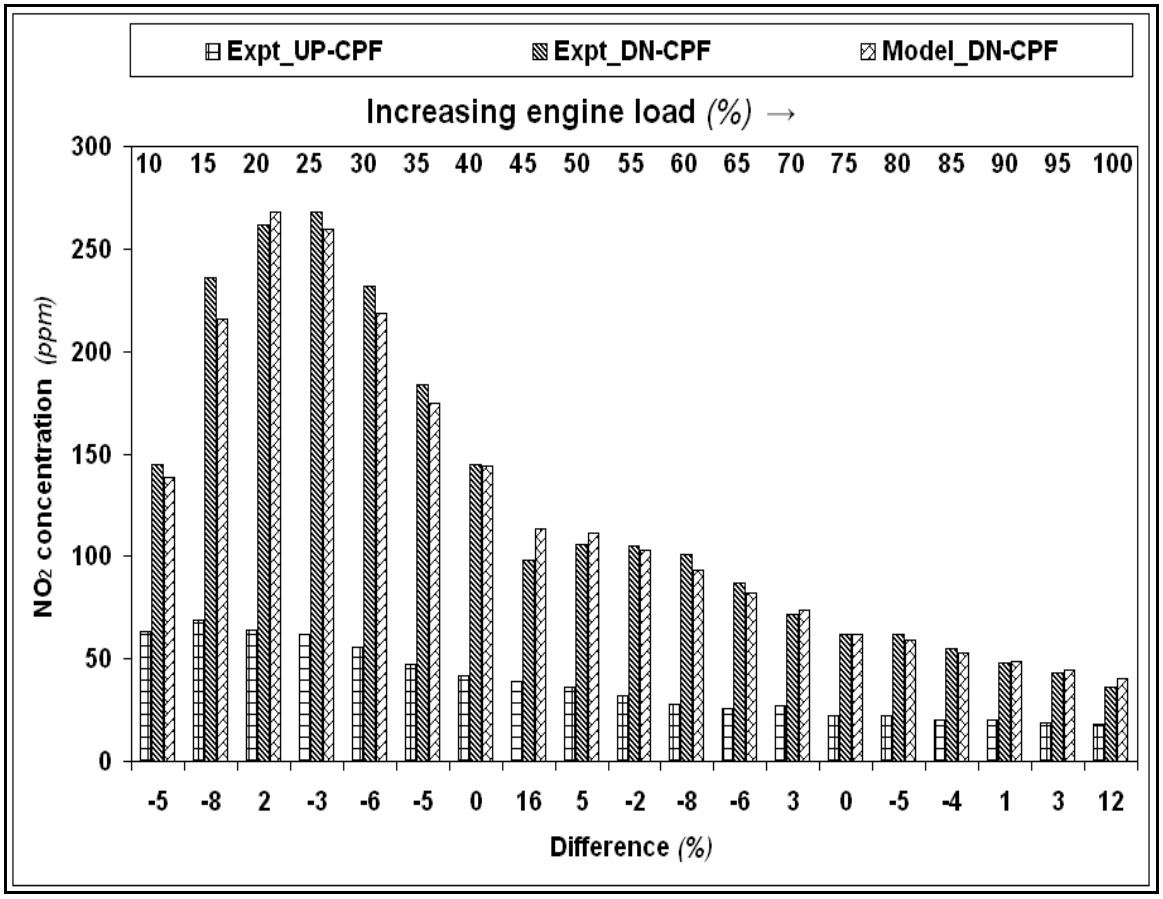

Figure 64: Experimental DOC inlet and outlet NO_2 concentrations compared to model-predicted DOC outlet NO_2 concentrations at 1650 rpm

Model simulation results of *CO*, *HC*, *NO* and NO_2 concentration data at 2200 rpm from the calibrated DOC model as compared to experimental values of the same are shown in Figure 65, Figure 66, Figure 67 and Figure 68 respectively.

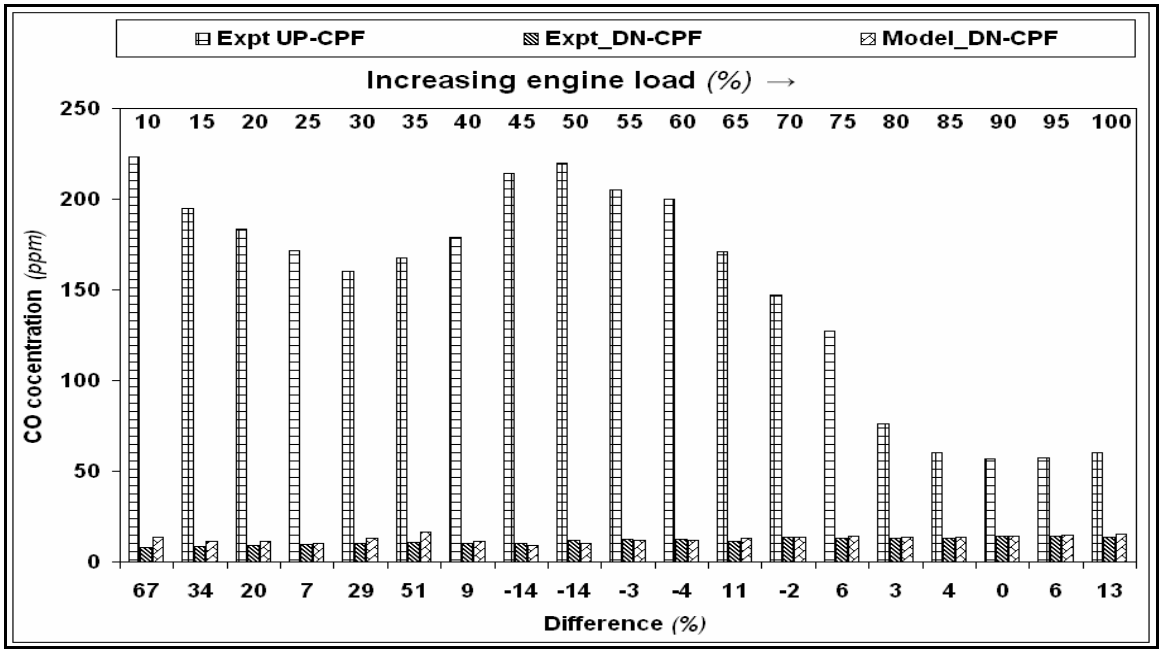

Figure 65: Experimental DOC inlet and outlet *CO* concentrations compared with model-predicted DOC outlet *CO* concentrations at 2200 rpm

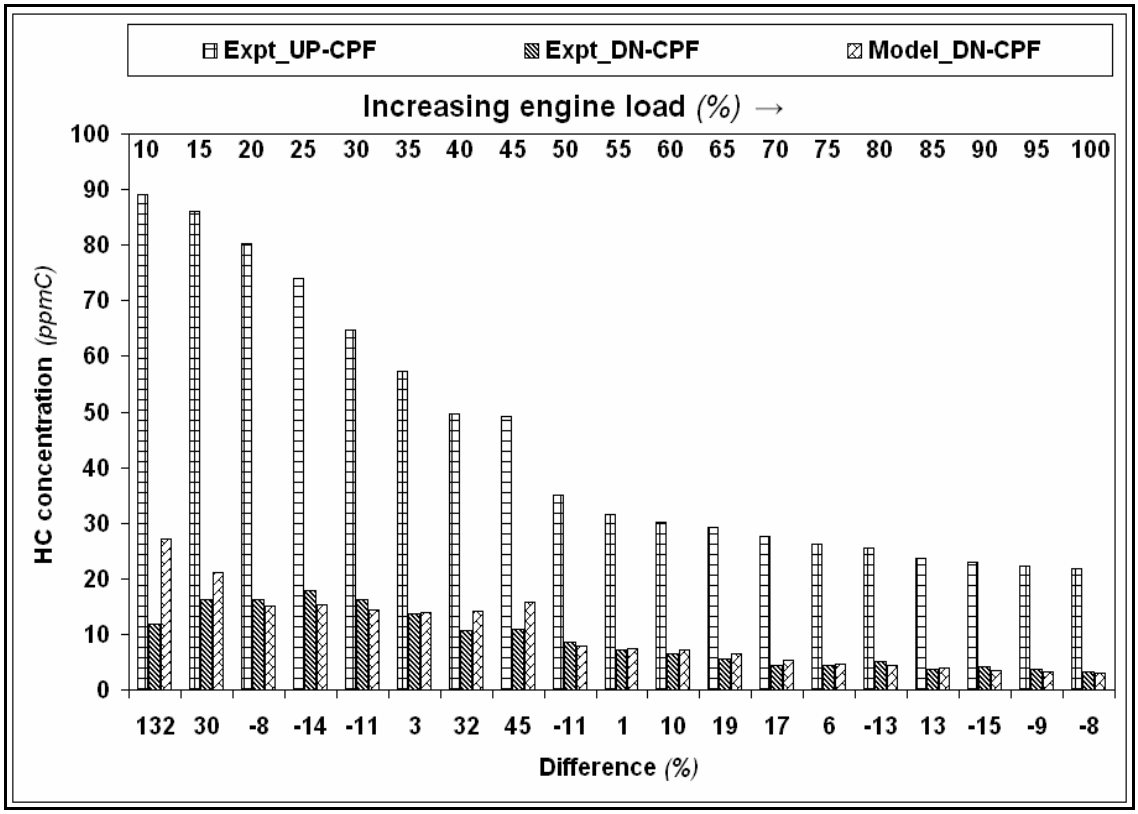

Figure 66: Experimental DOC inlet and outlet *HC* concentrations compared to model-predicted DOC outlet *HC* concentrations at 2200 rpm

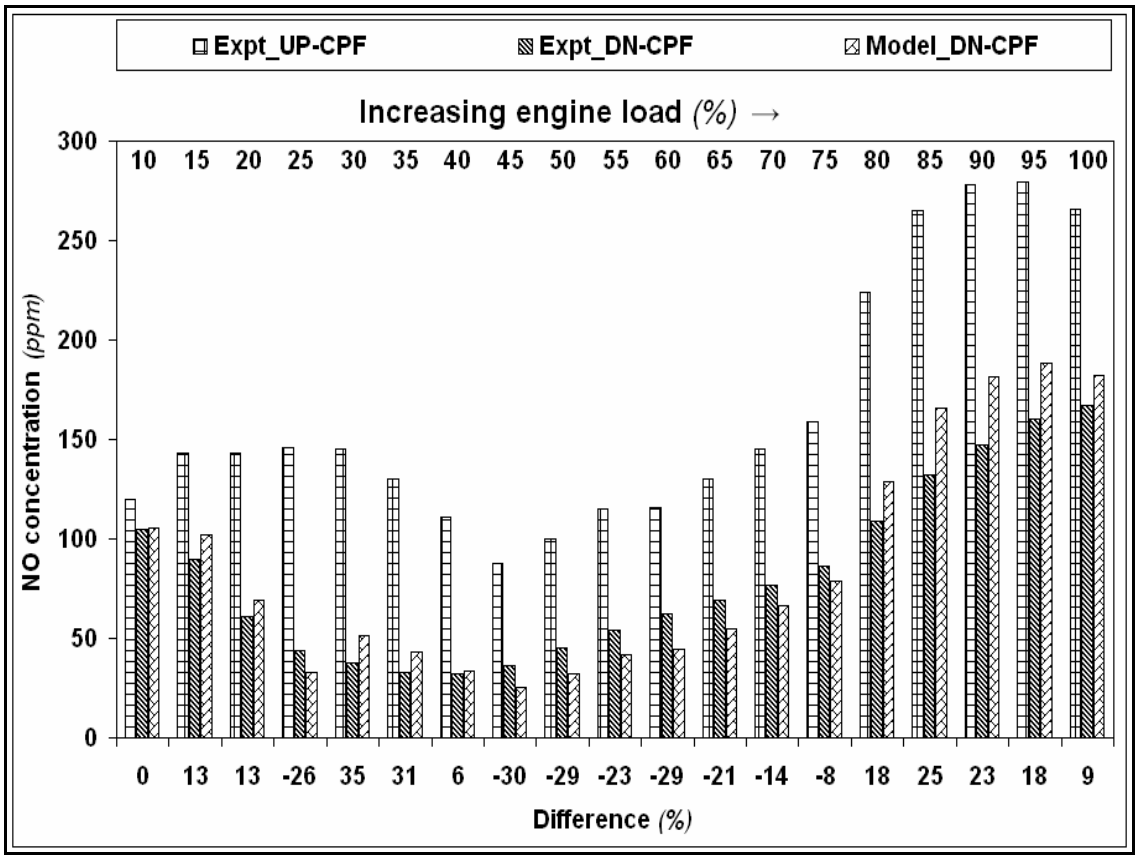

Figure 67: Experimental DOC inlet and outlet *NO* concentrations compared to model-predicted DOC outlet *NO* concentrations at 2200 rpm

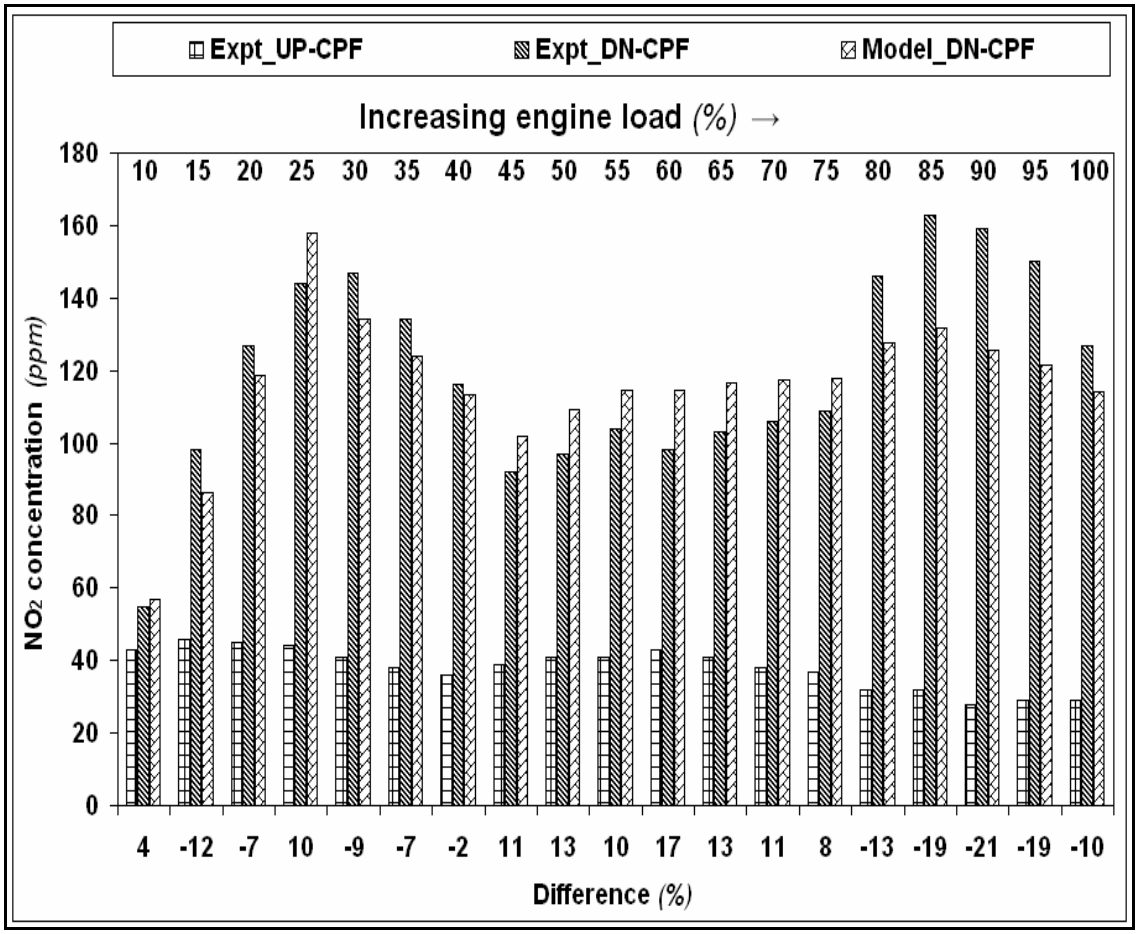

Figure 68: Experimental DOC inlet and outlet NO_2 concentrations compared to model-predicted DOC outlet NO_2 concentrations at 2200 rpm

Table 10 shows the kinetic parameters obtained from the DOC model calibrated to experimental data at 2200 rpm. The single set of kinetic parameters were obtained by matching the model-predicted values of *CO*, *HC*, *NO* and NO_2 to within ±1 ppm for *CO* and *HC*, and within ±5 *ppm* for *NO* and NO_2, of experimental DOC outlet concentrations of the same in each engine load case, and then using a semi-log plot of the individual reaction rate constants ($\ln(k_i)$) plotted vs. inverse of absolute DOC inlet temperatures ($1/T$) and curve-fitting a straight line to this data to get unified values of frequency factors and activation energies for each reaction, as is commonly done for chemical reactions for which rate constants can be expressed in the Arrhenius form. This single set of kinetic parameters were then used in the DOC model to predict the DOC outlet concentrations of *CO*, *HC*, *NO* and NO_2 species at all engine load cases at the rated speed (2200 rpm).

Outlet concentrations of *CO* and *HC* showed good agreement with experimental values in the 50-75% engine load range (-57 to +43% of experimental values for *CO*, and -11 to +27% for *HC* in this range of engine loads), showing that pre-exponential factors determined for these reactions are representative of the respective reaction kinetics. *NO* and NO_2 concentrations in the 10-75% engine load range showed good agreement with experimental values (-39 to +20% variation from experimental values for *NO* and -16 to +33% variation for NO_2). *NO* and NO_2 outlet concentrations in the 80-100% engine load range, however, showed variation with varying engine loads (as can be seen from Figures

65 and 66, mainly due to varying *NO* and NO_2 inlet concentrations), indicating that the reaction rate for this reaction (*NO* oxidation/NO_2 dissociation) may not be accurately represented for the entire range of engine load conditions by the reaction rate expressions currently employed. Due to this, model-predicted values of *CO* and *HC* outlet concentrations were also deviating from the experimental values of the same in the 80-100% engine load case range, due to the inhibition factors G_1 and G_3 appearing in Equations (20) and (22) being predicted inaccurately.

In particular, the order of dependence of the reaction rate on solid-phase *NO* mole fraction may be different from that assumed in the reaction rate equation of *NO* (Equation (21)) used in the DOC model. The advantage, however, of having a single set of kinetic parameters is that the calibrated DOC model can be re-used for other engine speed and load conditions, for which outlet concentrations of *CO*, *HC*, *NO* and NO_2 can be predicted.

6.3 APPENDIX C

ADDITIONAL DATA FROM THE CALIBRATED 1-D 2-LAYER CPF MODEL

Table 15 shows the geometry properties of the *10.5 in. x 12 in., 200 cpsi* cordierite CPF unit that was used for model calibration. These property values were kept constant for all engine load cases which the CPF model was calibrated to.

Table 15: CPF geometry properties used for CPF model calibration to experimental data

Property (units)	***Value***
Channel wall thickness *(m)*	3.048×10^{-4}
Channel width *(m)*	1.49×10^{-3}
Channel length *(m)*	0.3048
Number of inlet cells *(.)*	8659
Diameter *(m)*	0.2667
Clean substrate wall porosity *(.)*	0.50
Clean substrate wall pore diameter *(m)*	11×10^{-6}
Bulk density of substrate wall *(kg/m^3)*	1130
Specific heat capacity of substrate wall *(J/kg-K)*	1000
Specific heat capacity of *PM* cake layer *(J/kg-K)*	1510
Thermal conductivity of *PM (W/m-K)*	2.1
Thermal conductivity of substrate wall *(W/m-K)*	1.0

Exhaust conditions used at various engine load cases collected from experimental data which were used as model inputs for the CPF model during calibration are given in Table 16. Exhaust temperatures presented here are the average exhaust temperatures measured once the engine reached steady state. Also, volumetric flow-rates and *PM* inlet concentrations presented here are in actual units (as opposed to the same values presented in standard units in Table 16).

Table 16: Exhaust conditions at various engine load cases used as input for CPF model calibration at 2200 rpm

	25%		**50%**		**75%**		**100%**	
	CPF	**DOC+CPF**	**CPF**	**DOC+CPF**	**CPF**	**DOC+CPF**	**CPF**	**DOC+CPF**
T_{inf} *(°C)*	250	267	343	364	379	408	405	428
$\dot{V}_{act}$ *(m^3/s)*	.23	.23	.37	.38	.47	.50	.55	.58
C_{in} *(mg/m^3)*	3.4	2.3	1.9	1.2	1.3	1.1	1.2	1.3
Y_{O_2} *(.)*	.13	.13	.10	.10	.09	.08	.07	.07
Y_{NO_2} *(.)*	38	144	44	101	37	111	27	127
Y_{NO} *(.)*	160	53	101	44	156	77	264	134

$Y_{O_2,mix}$ *(.)*	.13	.13	.10	.10	.09	.08	.07	.07
$Y_{N_2,mix}$ *(.)*	.76	.76	.76	.76	.75	.75	.75	.75
$Y_{H_2O,mix}$ *(.)*	.06	.06	.08	.08	.08	.08	.09	.09
$Y_{CO_2,mix}$ *(.)*	.05	.05	.07	.07	.08	.08	.08	.08

Kinetic parameters that were varied to calibrate the CPF model in different engine load cases are presented in Table 17. Activation energies used for the various reaction mechanisms were kept constant, and pre-exponential factors were varied to calibrate the model as explained in 'CPF Model Calibration & Modeling Results' section.

Table 17: Kinetic parameters for various load cases used for CPD model calibration to experimental data at 2200 rpm

	25%		**50%**		**75%**		**100%**	
	CPF	**DOC+CPF**	**CPF**	**DOC+CPF**	**CPF**	**DOC+CPF**	**CPF**	**DOC+CPF**
A_{th} *(m/s-K)*	2.5	2.5	2.5	2.5	2.5	2.5	2.5	2.5
Ea_{th} *(J/kmol)*	1.497×10^8							
A_{cat} *(m/s-K)*	0	0	0	0	0	0	0	0
Ea_{cat} *(J/kmol)*	1.20×10^8							
A_{NO_2} *(m/s-$K^{0.5}$)*	7.5	4.5	1.5	1.2	1.0	1.0	3.2	1.1
$A_{NO_2,wall}$ *(m/s-$K^{0.5}$)*	6.8	1.5	.72	1.8	.60	2.6	.92	2.5
Ea_{NO_2} *(J/kmol)*	0.73×10^8							
A_{NO} *(m/s-K^3)*	0	0	0	0	0	0	80	0
Ea_{NO} *(J/kmol)*	0.906×10^8							

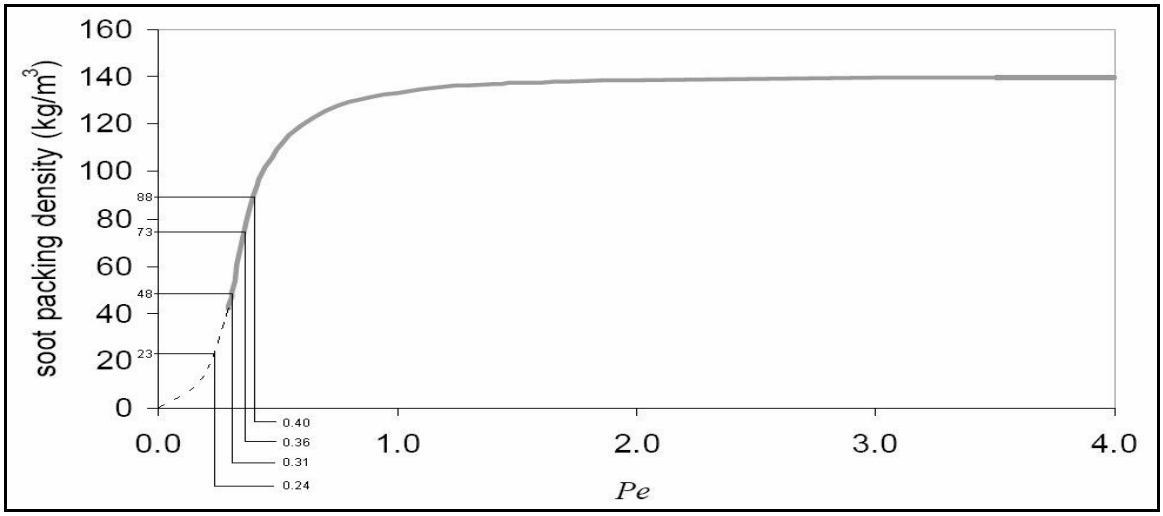

Figure 69: *PM* packing density in the *PM* cake vs. Global Peclet numbers (adapted from [16])

Table 18 shows the substrate wall and *PM* cake properties that were varied with engine load at all 8 engine load cases that the CPF model was calibrated to, which agree in range of values with values obtained from previous research at MTU (references [9 and 31]). Figure 69 shows the relation for *PM* packing density in the *PM* cake layer (ρ_p) as obtained from reference [16], and the interpolated values of the same used for various engine load cases (shown in Table 18).

Table 18: Substrate wall and *PM* cake layer properties that were varied to calibrate the CPF model at various engine load cases at 2200 rpm

	25%		**50%**		**75%**		**100%**	
	CPF	**DOC+CPF**	**CPF**	**DOC+CPF**	**CPF**	**DOC+CPF**	**CPF**	**DOC+CPF**
$k_{t,0}$ $(x10^{-13}\ m^2)$	.42	.47	.52	.47	.63	.80	.65	.77
ψ (.)	.90	.90	.89	.91	.88	.88	.86	.89
$\rho_{p,w}$ (kg/m^3)	6.5	5.3	5.9	2.6	2.5	.95	2.2	.80
k_p (m^2)	.88	.58	.64	1.2	3.3	3.3	2.0	2.5
ρ_p (kg/m^3)	40	40	60	60	73	73	90	90
A_η (.)	.97	.98	.98	.95	.98	.97	.98	.98
$\frac{\eta_c}{d_{c,cake}}$ (m^{-1})	.08	.12	.07	.25	.15	.63	.27	.53

PM mass deposited in the *PM* cake layer and the substrate wall in the CPF at all engine load cases for which the CPF model was calibrated to are presented in Figure 70 and Figure 71 respectively. All results presented are till *8 hours* of loading (simulation) time. Overall levels of *PM* mass deposited in the *PM* cake layer and substrate wall decreased with increasing engine loads in the same configuration and were lower for DOC+CPF than for CPF configuration in the same engine load condition. Substrate wall *PM* deposition characteristics determine the CPF pressure drop characteristics in each engine load case, as majority of CPF pressure drop is contributed to by pressure drop due to the wall, as can be seen from Figure 34 thru Figure 37 (in the 'Results and Discussions' section).

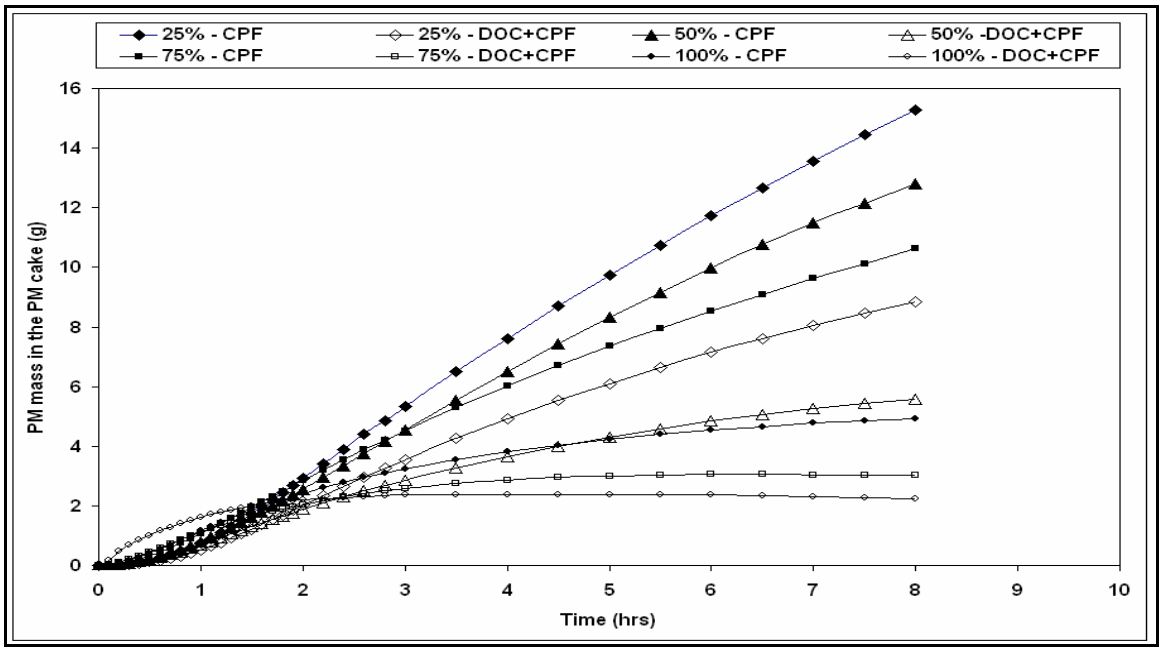

Figure 70: A comparison of *PM* mass in the *PM* cake layer obtained from the calibrated CPF model for the 8 engine load cases at 2200 rpm till 8 hours of loading time

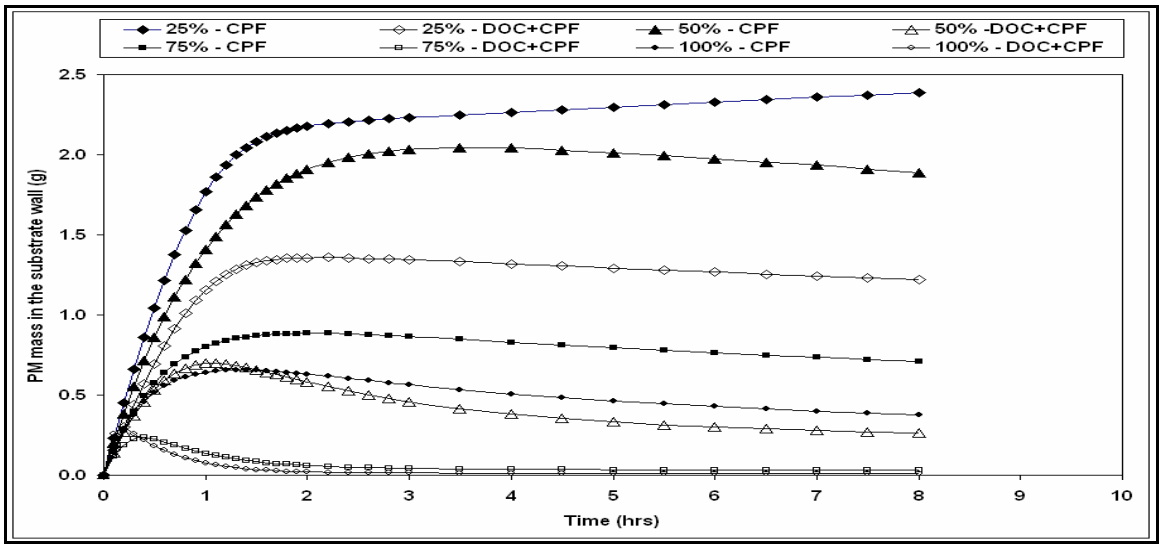

Figure 71: A comparison of *PM* mass in the substrate wall obtained from the calibrated CPF model for the 8 engine load cases at 2200 rpm till 8 hours of loading time

A comparison of the CPF model input parameters obtained from calibrated CPF model in this study (as shown in Table 19) and a previous research at MTU (Reference [31], shown in Table 22) shows that:

- $k_{t,0}$ values used in this study (*0.42-0.80 x10^{-13} m^2*) were lower than the corresponding value for the same used in previous research (kept constant at *2x10^{-13} m^2*).
- ψ values were in the (*0.86-0.90*) range in this study compared to corresponding values (*0.91-0.94*) used in the previous research.

Table 19: CPF model input parameters obtained from calibrated CPF model in this study for 2200 data [25]

	CPF	DOC+CPF	CPF	DOC+CPF	CPF	DOC+CPF	CPF	DOC+CPF
Current study (Reference [25])								
	25%		**50%**		**75%**		**100%**	
$k_{t,0}$ *(x 10^{-13} m^2)*	.42	.47	.52	.50	.63	.80	.65	.77
ψ *(.)*	.90	.90	.89	.91	.88	.88	.86	.89
ρ_{pw} *(kg/m^3)*	6.5	5.3	5.9	2.6	2.5	1.0	2.2	0.8
k_p *(x 10^{-14} m^2)*	.88	.58	.64	1.2	3.3	3.3	2.0	2.5
ρ_p *(kg/m^3)*	40	40	60	60	73	73	90	90
A_η *(.)*	.97	.98	.98	.95	.98	.97	.98	.98
$\frac{\eta_c}{d_{c,cake}}$ *(x10^5 m^{-1})*	8	12	7	25	15	63	27	53
A_{th} *(m/s-K)*	2.5	2.5	2.5	2.5	2.5	2.5	2.5	2.5
A_{NO_2} *(m/s-K$^{.5}$)*	7.5	4.5	1.5	1.2	1.0	1.0	3.2	1.1
$A_{NO_2,wall}$ *(m/s-K$^{.5}$)*	6.8	1.5	.72	1.8	.60	2.6	.92	2.5
A_{NO} *(m/s-K^3)*	0	0	0	0	0	0	80	0

- k_p values in this study were generally in the same range as the values for the same in the previous research.
- ρ_p values used in this study were lower (*40-90 kg/m^3*) than those used in the previous research (*131-134 kg/m^3*), due to lower values of global *Pe* numbers found in this study.
- Values of A_η used in this study varied in the (*0.95-0.98*) range, while those for the previous research varied in the (*0.98-0.99*) range.
- $\frac{\eta_c}{d_{c,cake}}$ values in this study were in the (*7-63x10^5 m^{-1}*) range while those used in previous research were in the (*15-50x10^5 m^{-1}*) range.
- A_{th} value used in this research (*2.5 m/s-K*) was equal to that used in previous research.

- A_{NO_2} values varied in the range of (*7.5-1.0 m/s-K*$^{.5}$) while it was kept constant (*1.0 m/s-K*$^{.5}$) in previous research.
- $A_{NO_2,wall}$ values varied in the (*6.8-0.6 m/s-K*$^{.5}$) range for this study compared to (*3.1-0.8 m/s-K*$^{.5}$) in the previous research.
- A_{NO} values could not be determined accurately in this study except for the 100% engine load case in CPF configuration (*80 m/s-K*^{3}), whereas in the previous research, it varied in the *37000-100* range for CPF and *28000-100* range for DOC+CPF configurations.

Table 20: CPF model input parameters obtained from calibrated CPF model in previous research for 2100 rpm data [9 and 31]

	CPF	**DOC+CPF**	**CPF**	**DOC+CPF**	**CPF**	**DOC+CPF**	**CPF**	**DOC+CPF**
Previous research (References [9 and 31])								
	20%		**40%**		**60%**		**75%**	
$k_{t,0}$ *(x 10*$^{-13}$ *m*^{2}*)*	2.0	2.0	2.0	2.0	2.0	2.0	2.0	2.0
ψ *(.)*	.93	.93	.93	.94	.92	.92	.91	.93
ρ_{pw} *(kg/m*^{3}*)*	1.9	1.9	1.9	1.8	1.8	1.8	1.3	1.3
k_p *(x 10*$^{-14}$ *m*^{2}*)*	.70	.50	.45	2.0	2.5	4.3	1.5	1.5
ρ_p *(kg/m*^{3}*)*	131	131	133	133	133	133	134	134
A_η *(.)*	.99	.99	.98	.99	.99	.98	.98	.98
$\frac{\eta_c}{d_{c,cake}}$ *(x10*^{5} *m*$^{-1}$*)*	49	49	50	15	34	25	33	33
A_{th} *(m/s-K)*	2.5	2.5	2.5	2.5	2.5	2.5	2.5	2.5
A_{NO_2} *(m/s-K*$^{.5}$*)*	1.0	1.0	1.0	1.0	1.0	1.0	1.0	1.0
$A_{NO_2,wall}$ *(m/s-K*$^{.5}$*)*	3.0	2.0	1.7	3.1	.85	1.3	1.0	.80
A_{NO} *(m/s-K*^{3}*)*	3.7e4	2.8e4	1e4	5e3	450	745	100	100

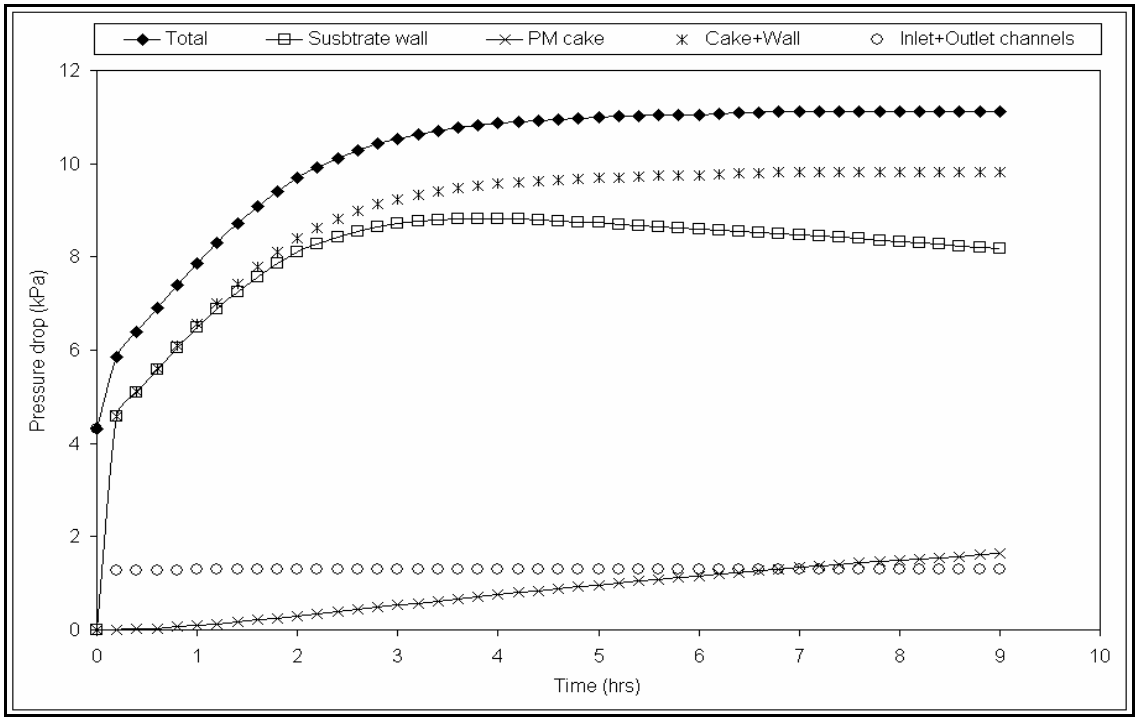

Figure 72: Components of CPF pressure drop from calibrated CPF model in CPF configuration at the 50% engine load case at 2200 rpm

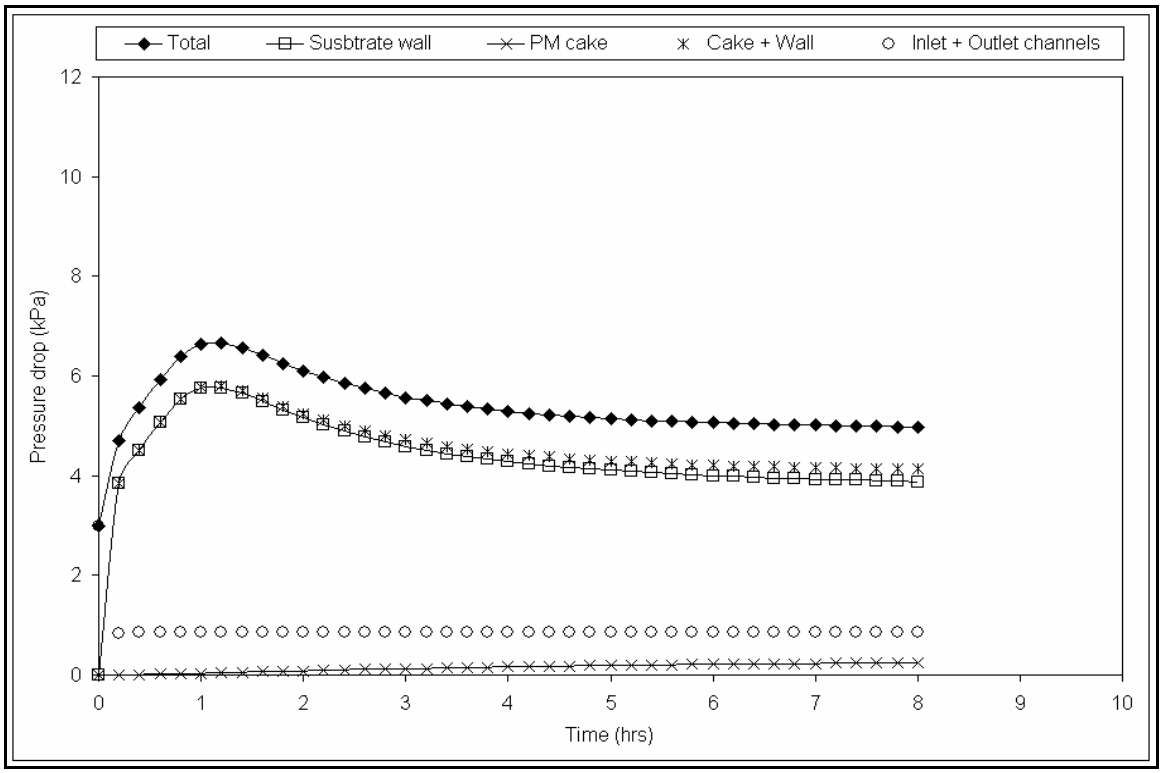

Figure 73: Components of CPF pressure drop from calibrated CPF model in DOC+CPF configuration at the 50% engine load case at 2200 rpm

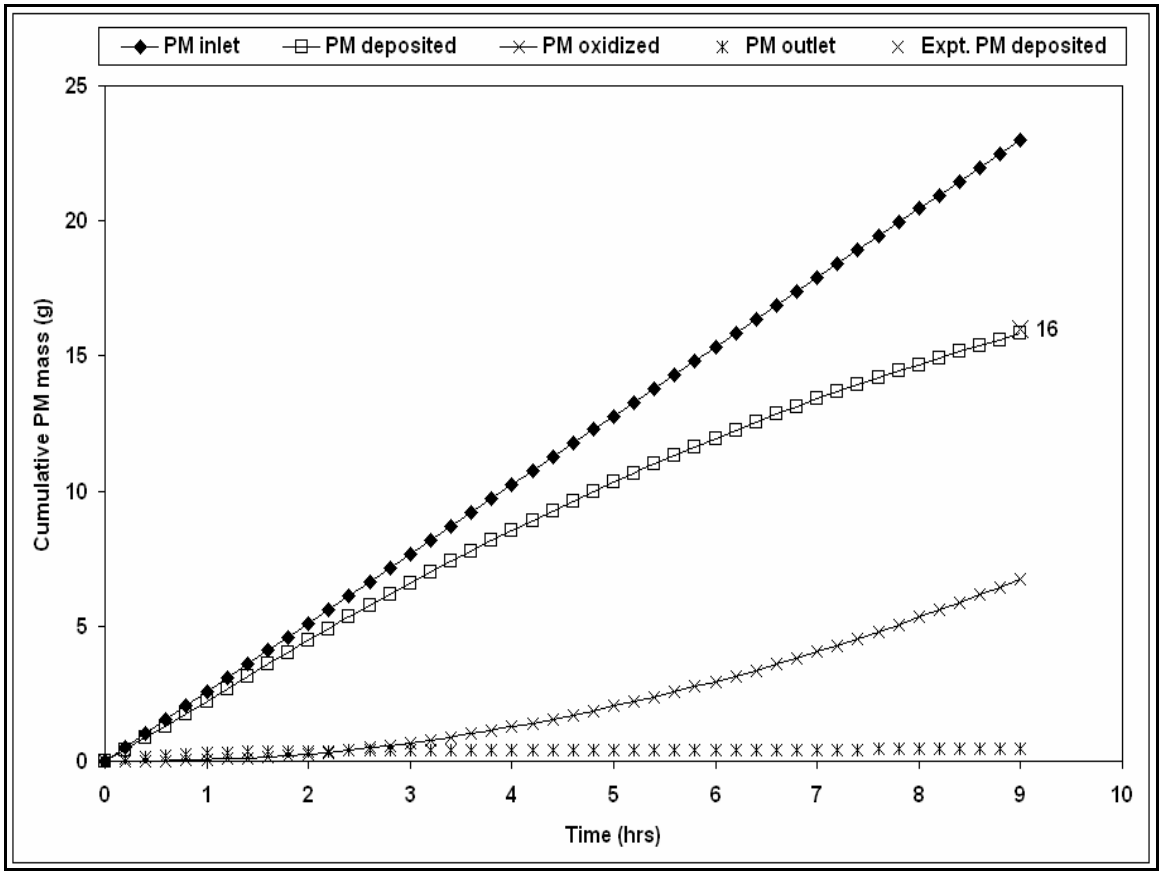

Figure 74: *PM* mass balance curves obtained from the calibrated CPF model at 50% engine load case in the CPF configuration at 2200 rpm

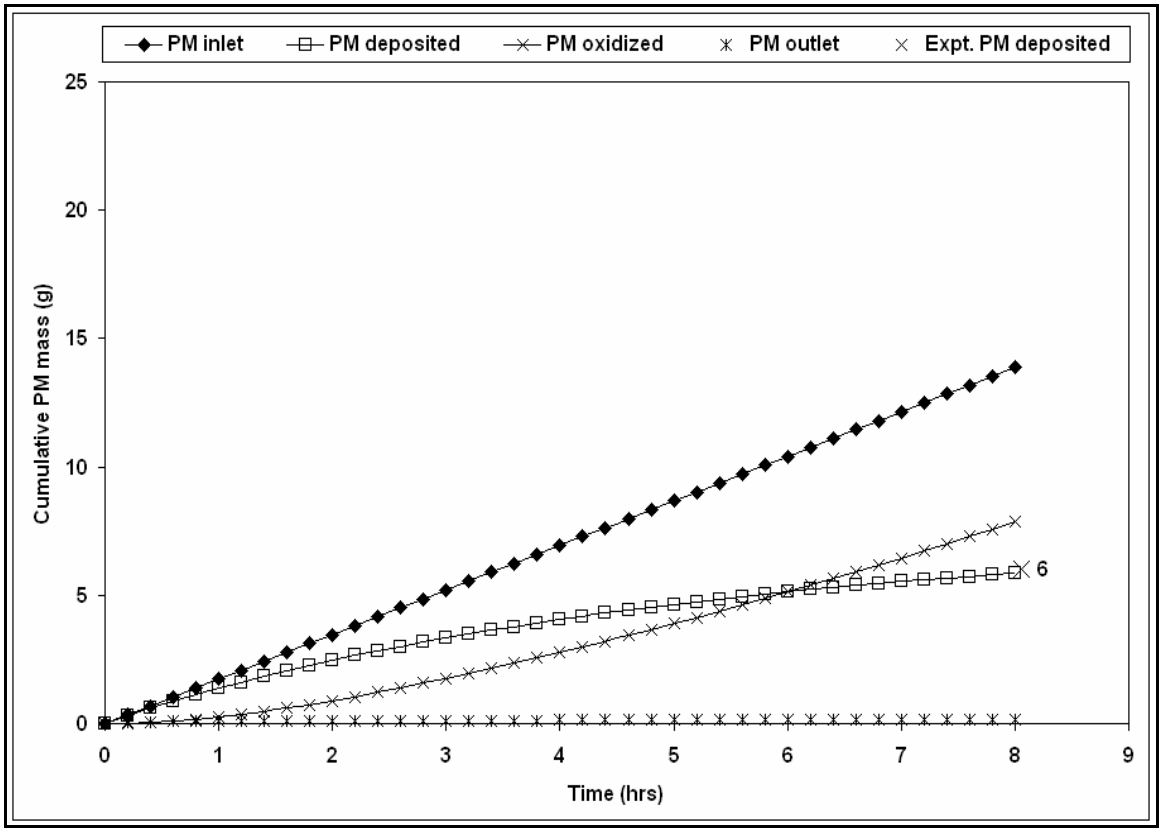

Figure 75: *PM* mass balance curves obtained from the calibrated CPF model at 50% engine load case in the DOC+CPF configuration at 2200 rpm

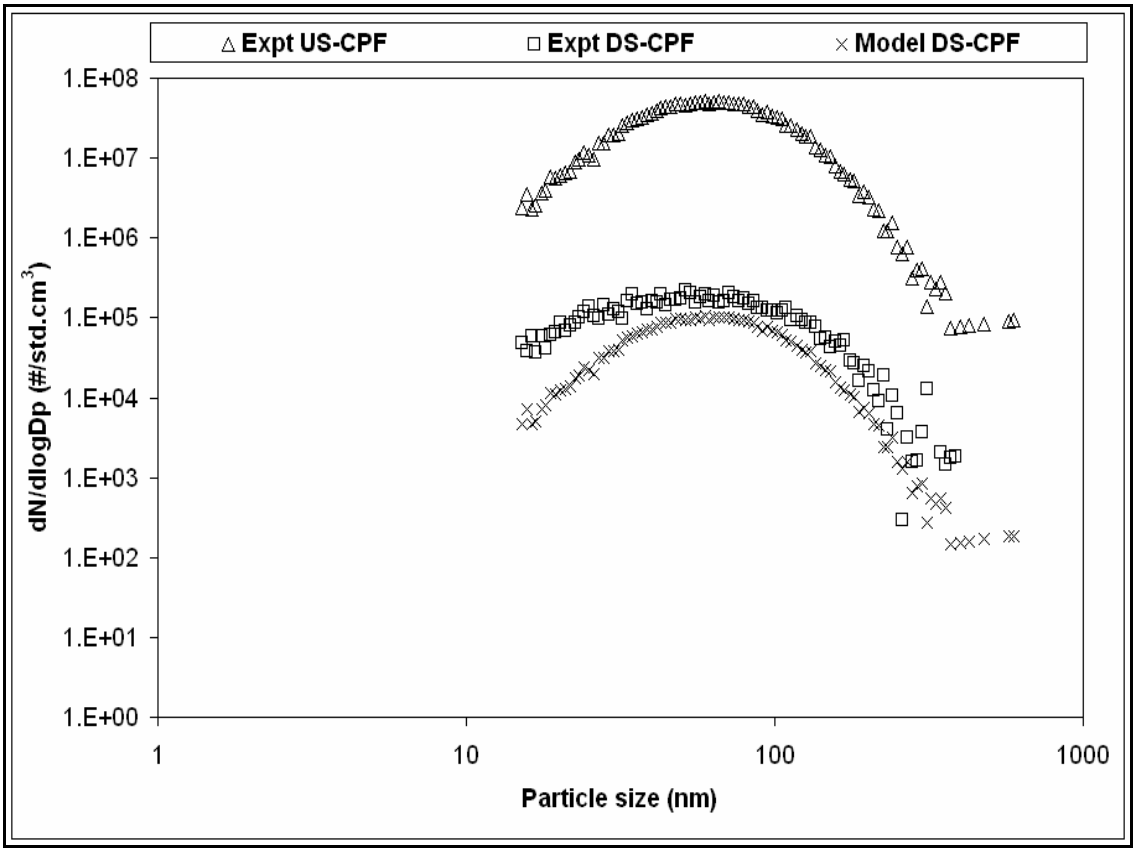

Figure 76: Average UP-CPF PSD and a comparison of experimental DN-CPF PSD at 8 hours of loading time and model-predicted DN-CPF PSD at 8 hrs of simulation time, for the 25% engine load case in the DOC+CPF configuration at 2200 rpm

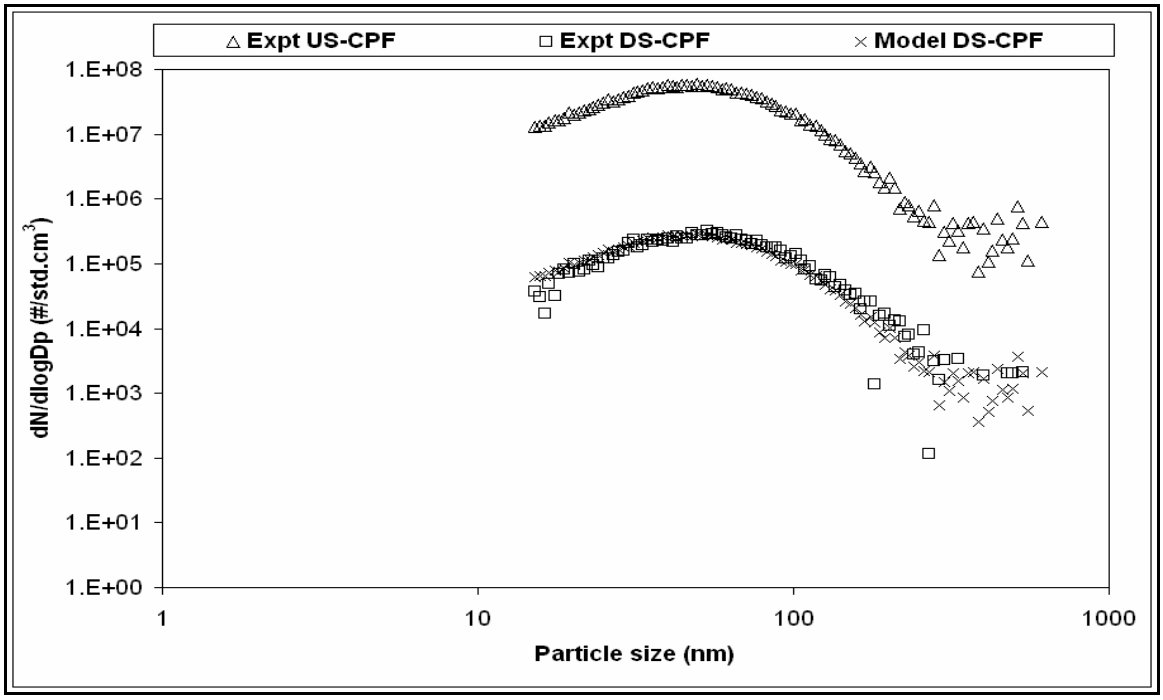

Figure 77: Average UP-CPF PSD and a comparison of experimental DN-CPF PSD at 8 hours of loading time and model-predicted DN-CPF PSD at 8 hrs of simulation time, for the 100% engine load case in the DOC+CPF configuration at 2200 rpm

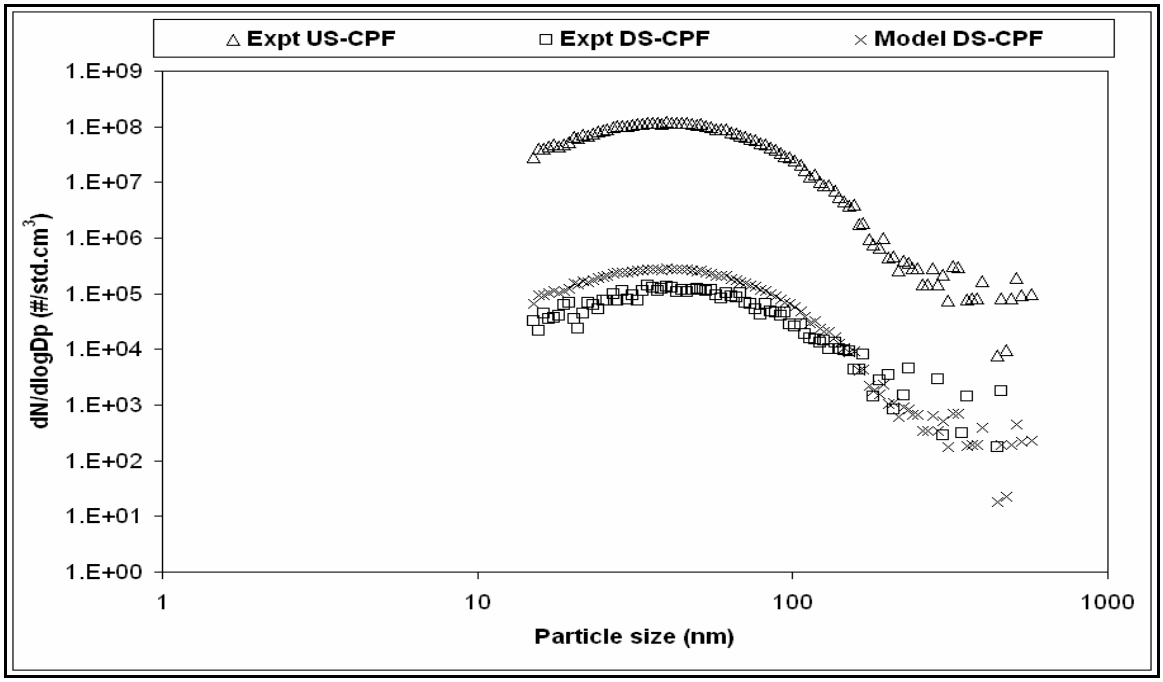

Figure 78: Average UP-CPF PSD and a comparison of experimental DN-CPF PSD at 8 hours of loading time and model-predicted DN-CPF PSD at 8 hrs of simulation time, for the 50% engine load case in the CPF configuration at 2200 rpm

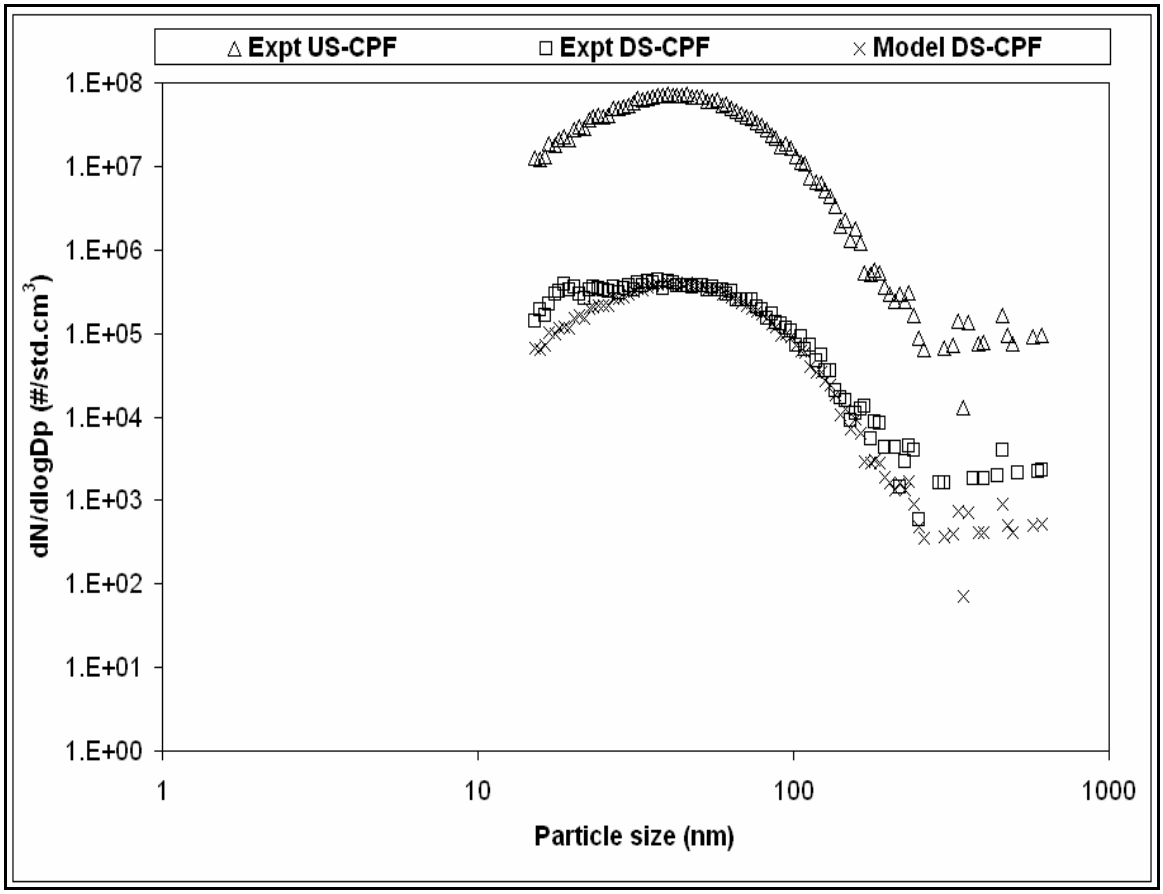

Figure 79: Average UP-CPF PSD and a comparison of experimental DN-CPF PSD at 8 hours of loading time and model-predicted DN-CPF PSD at 8 hrs of simulation time, for the 50% engine load case in DOC+CPF configuration at 2200 rpm

Table 21: A comparison of experimentally measured variables and CPF oxidation characteristics between current study and previous research

Current Study (Reference [25])								
Engine	**John Deere 2004 6068H** (DEV), 6.8 liter 6 in-line, VGT, aftercooled, 187 kW@2200 rpm, 995 Nm@1650 rpm, Auto low P loop (aftercooled) EGR							
Fuel	ULSF, API gravity = 36.6, Cetane number = 48.2, Sulfur content = 11.6 ppm							
CCRT®	Cordierite 400 cpsi, 10.5"x6" square channel (coated) DOC + Cordierite 200 cpsi, 10.5"x12" square channel (coated) 11μm mean pore size CPF							
Engine load *(%)*	**25**		**50**		**75**		**100**	
	CPF	**DOC+CPF**	**CPF**	**DOC+CPF**	**CPF**	**DOC+CPF**	**CPF**	**DOC+CPF**
Speed *(rpm)*	2200	2200	2200	2200	2200	2200	2200	2200
Load *(Nm)*	203	203	406	406	608	608	811	811
Power *(kW)*	47	47	94	94	140	140	187	185
A/F ratio *(.)*	43	43	31	32	27	27	24	24
EGR* *(.)*	20.4	20.1	20.1	19.8	20.0	19.3	18.9	18.5
CPF inlet temperature *(°C)*	250	267	343	364	380	408	405	428
Volumetric flow rate *(std.m^3/s)*	0.130	0.129	0.181	0.179	0.215	0.218	0.242	0.245
CPF inlet *PM* conc. *(mg/std.m^3)*	6.04	4.16	3.92	2.53	2.82	2.41	2.72	2.96
CPF inlet *PM* mass rate *(mg/s)*	0.78	0.53	0.71	0.45	0.61	0.53	0.66	0.73
CPF inlet *NO_2* conc. *(ppm)*	38	144	44	101	37	111	27	127
CPF outlet *NO_2* conc. *(ppm)*	12	125	21	65	19	74	32	91
***NO_2* cons.-prod. In CPF** *(ppm)*	27	20	23	40	17	41	-6	36
***PM* oxidation efficiency** *(%)*	22	34	29	57	36	79	73	89

Previous Research (References [9 and 31])								
Engine	**Cummins ISM 2002**, 10.8 liter 6 in-line, VGT, aftercooled, 246 kW@2100 rpm,1697 Nm@1200 rpm, Auto high P loop (aftercooled) EGR							
Fuel	API gravity = 39.1-39.4, Cetane number = 51.1-51.7, Sulfur content = 0.3-0.2 ppm							
CCRT®	Cordierite 400 cpsi, 10.5"x6" square channel (coated) DOC, Cordierite 200 cpsi, 10.5"x12" square channel (coated) 13µm MPS CPF							
Engine load *(%)*	**20**		**40**		**60**		**75**	
	CPF	**DOC+CPF**	**CPF**	**DOC+CPF**	**CPF**	**DOC+CPF**	**CPF**	**DOC+CPF**
Speed *(rpm)*	2100	2100	2100	2100	2100	2100	2100	2100
Load *(Nm)*	223	223	446	446	671	671	840	840
Power *(kW)*	49	49	98	98	148	148	185	185
A/F ratio *(.)*	52	52	41	40	33	34	30	30
EGR* *(.)*	16.0	15.6	14.2	14.1	11.7	11.3	9.3	9.3
CPF inlet temperature *(^oC)*	287	287	340	340	416	416	466	460
Volumetric flow rate *($std.m^3/s$)*	.245	.241	.279	.279	.313	.313	.341	.341
CPF inlet *PM* conc. *($mg/std.m^3$)*	17.9	16.4	23.5	20.2	14.0	15.5	10.8	10.8
CPF inlet *PM* mass rate *(mg/s)*	4.39	3.95	6.56	5.64	4.38	4.85	3.68	3.68
CPF inlet *NO_2* conc. *(ppm)*	33	105	22	136	25	103	13	83
CPF outlet *NO_2* conc. *(ppm)*	74	116	45	130	52	122	52	99
***NO_2* cons.-prod. in CPF** *(ppm)*	-41	-11	-23	6	-27	-19	-39	-16
***PM* oxidation efficiency** *(%)*	4	9	10	32	40	70	65	82

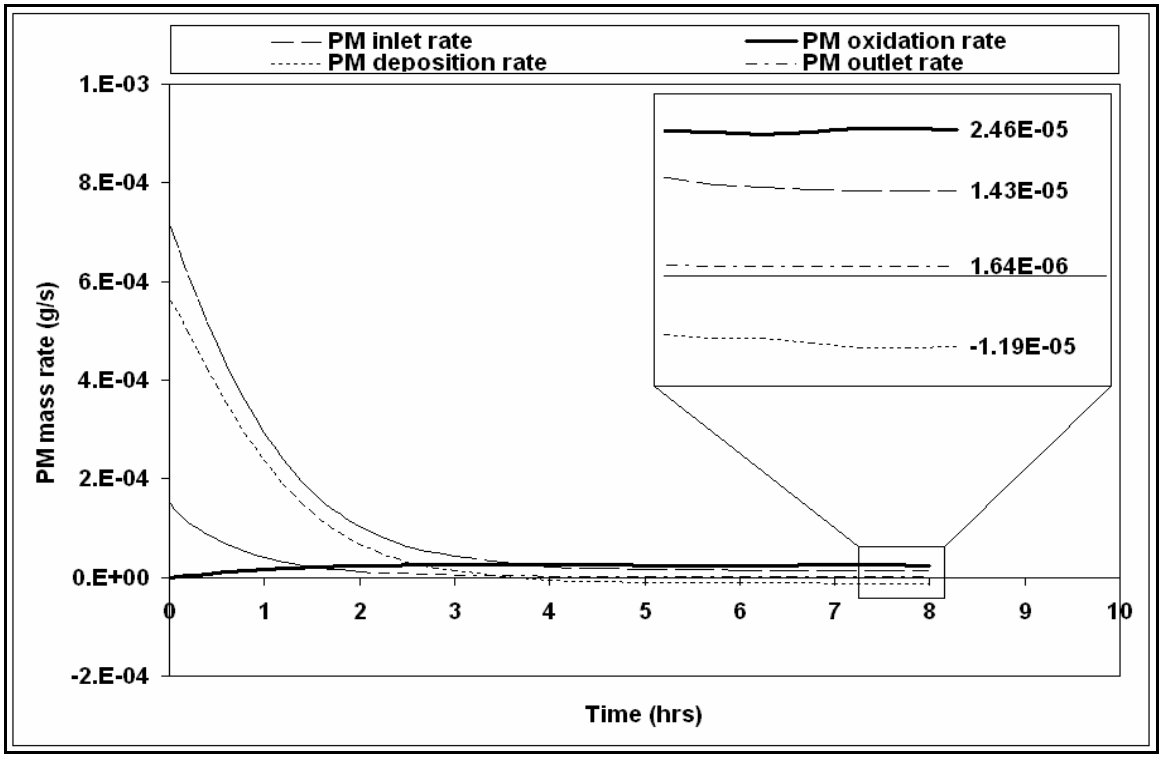

Figure 80: *PM* mass rates in the substrate wall at 50% engine load case in the CPF configuration at 2200 rpm

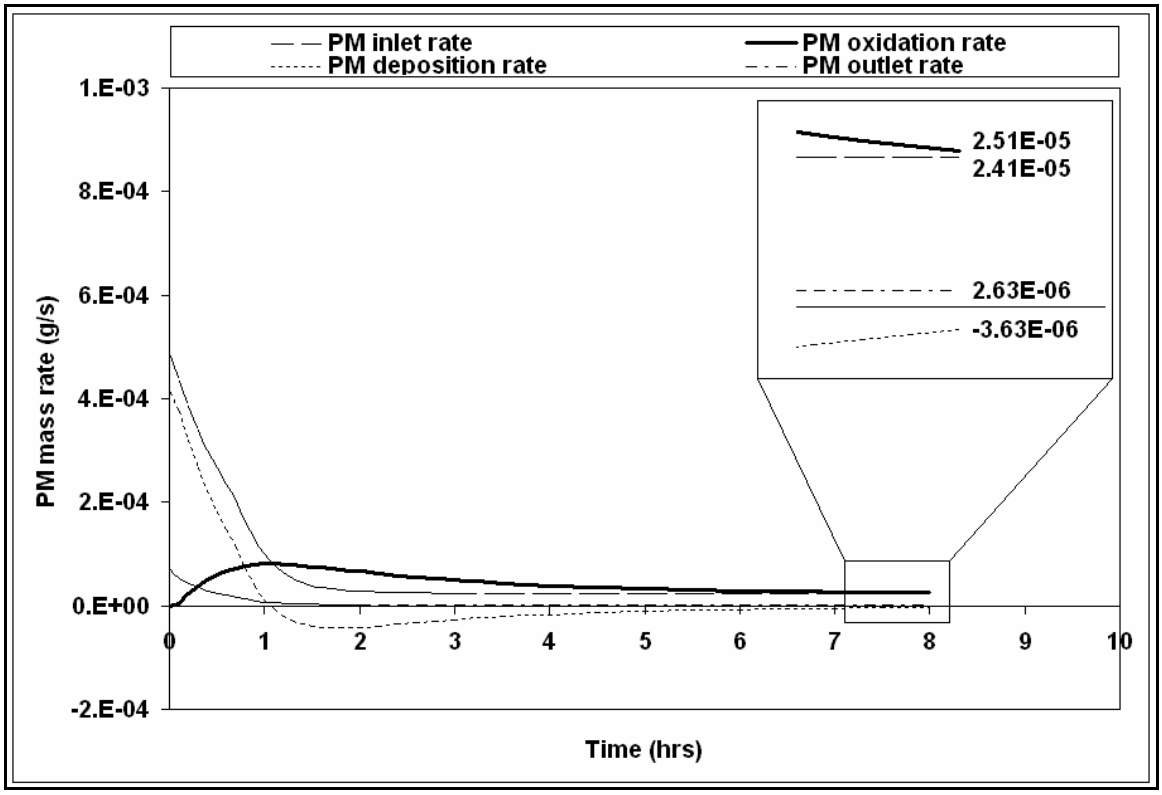

Figure 81: *PM* mass rates in the substrate wall at 50% engine load case in the DOC+CPF configuration at 2200 rpm

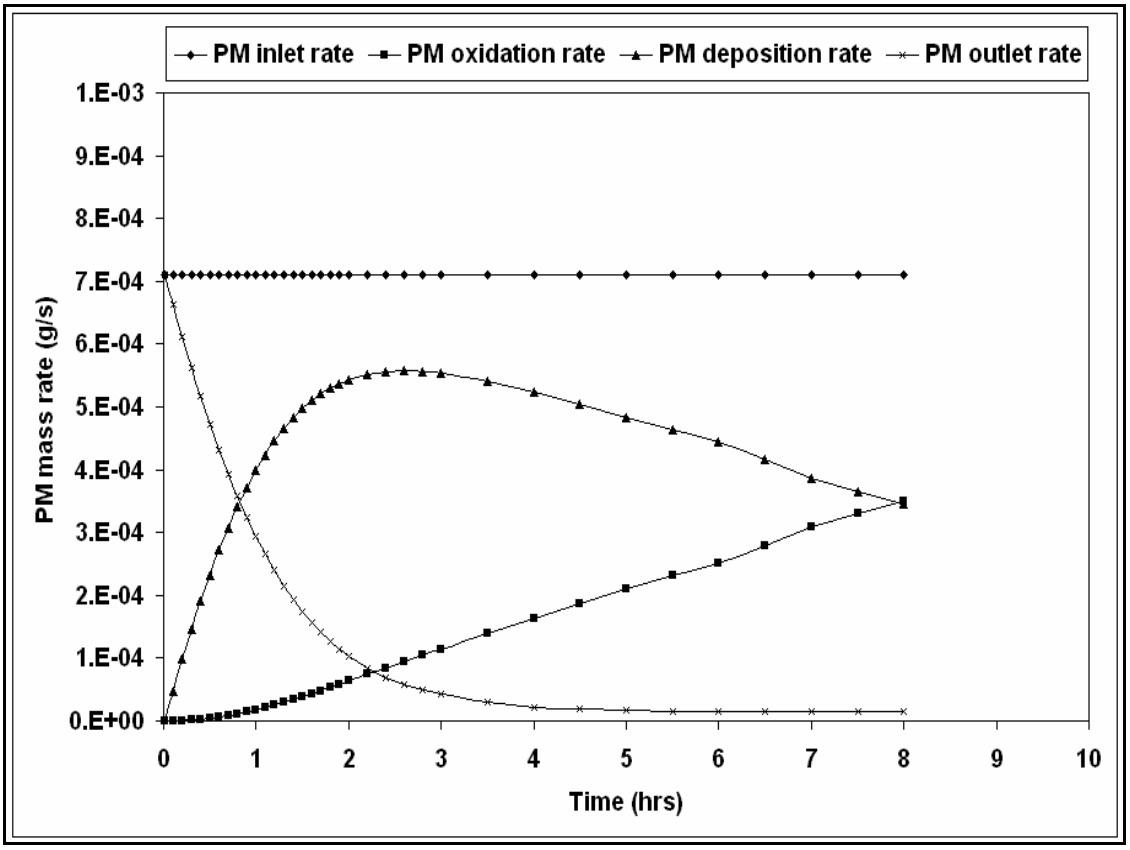

Figure 82: *PM* mass rates in the *PM* cake layer at 50% engine load case in the CPF configuration at 2200 rpm

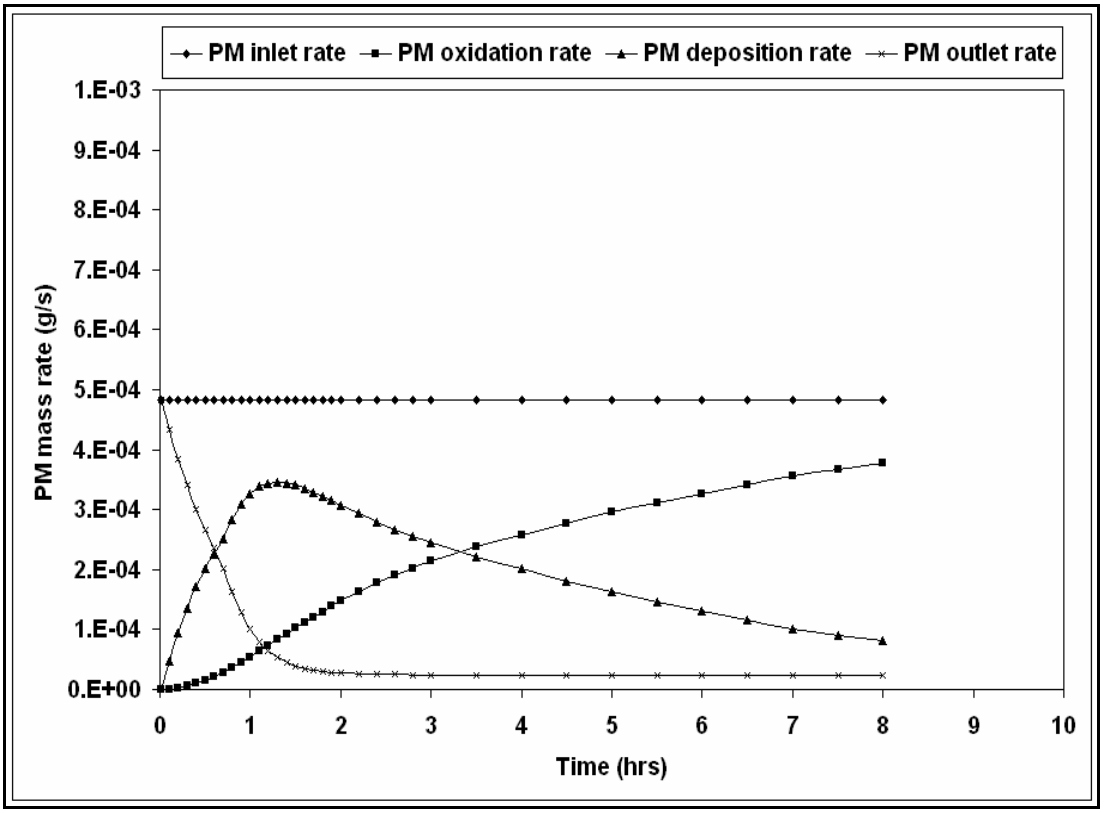

Figure 83: *PM* mass rates in the *PM* cake layer at 50% engine load case in the DOC+CPF configuration at 2200 rpm

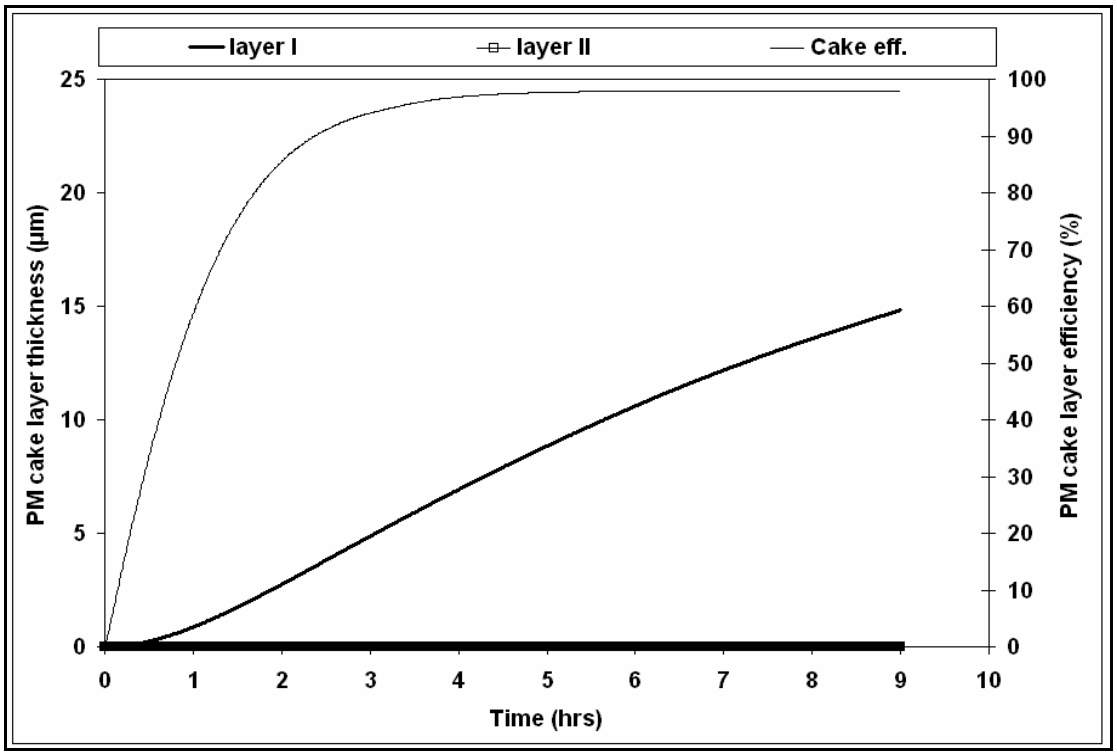

Figure 84: Thickness of *PM* cake layers I and II and PM cake layer efficiency in CPF configuration at 50% engine load case at 2200 rpm

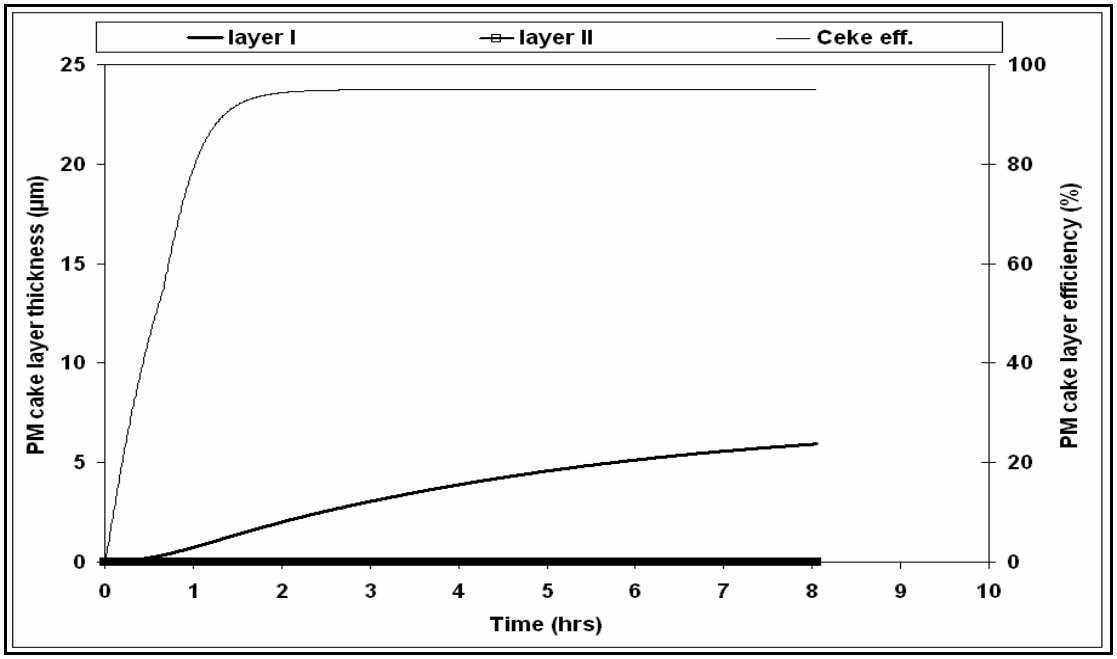

Figure 85: Thickness of *PM* cake layers I and II and PM cake layer efficiency in DOC+CPF configuration at 50% engine load case at 2200 rpm